MECHANICAL PROPERTIES OF SHIMANTO ACCRETIONARY COMPLEX AND NANKAI TROUGH ROCKS

A Thesis

by

PATRICK ROBERT NEBEL

Submitted to the Office of Graduate and Professional Studies of
Texas A&M University
in partial fulfillment of the requirements for the degree of

MASTER OF SCIENCE

Chair of Committee,	Hiroko Kitajima
Committee Members,	Richard Gibson
	David Schechter
Head of Department,	Julie Newman

May 2020

Major Subject: Geophysics

ABSTRACT

The threat from earthquakes and tsunamis on human life is immense. To conduct threat assessment and mitigate damage, the scientific community strives to generate physics-based models that accurately portray natural fault systems. Realistic models require better numerical description of deformation processes and mechanisms with appropriate initial and boundary conditions. Mechanical properties, such as elastic moduli and fracture strength, are important parameters in these models; however, it is difficult to accurately estimate these properties at depth. This study aims to document the elastic moduli, fracture strength, and acoustic velocities through laboratory experiments on rock samples collected from the ancient Shimanto accretionary complex and the subducting oceanic plate at the Nankai Trough offshore Japan. All the tested samples including basalt, Nobeoka mélange, Shimanto mélange, white sandstone, gray sandstone, and red shale exhibit an increase in Young's modulus and Poisson's ratio with increasing pressure. The triaxial deformation experiments exhibit that the white sandstone deforms brittle at effective pressure of 5-80 MPa, whereas the basalt deforms brittle at 5 and 10 MPa and ductile at 20 MPa. P-wave and S- wave velocities for the white sandstone and basalt range from 3.70-5.41 and 2.43-3.33 km/s. Based on the experiment results, the simple two layer models with various lithologies at different stress conditions were constructed to estimate the reflection coefficient at the boundary. 18 scenarios out of 64 scenarios considered result in similar reflection coefficient values observed along the plate boundary in the Nankai Trough.

ACKNOWLEDGEMENTS

I would like to thank my committee chair, Dr. Kitajima, for her patience and guidance throughout the course of this research.

I would also like to thank my committee members, Dr. Richard Gibson & Dr. David S Schechter, for their contributions.

Thanks also to all of my friends and colleagues in the Tectonophysics group. You have been a constant support and wonderful friends.

Finally, thanks to my parents for their unending encouragement and faith in me throughout this time.

CONTRIBUTORS AND FUNDING SOURCES

TABLE OF CONTENTS

LIST OF FIGURES

LIST OF TABLES

xi

1. INTRODUCTION

Subduction zones are convergent plate margins where the denser lithosphere subducts beneath the less dense lithosphere identified by the presence of a trench or trough. Examples include, but are not limited to, the Mariana Trench, Java Trench, Aleutian Trench, and the Nankai Trough. Observed in subduction zones are not only volcanic activities, as called as "Ring of Fire," but also seismic activities along the megathrust plate boundary faults. Significant slip on these megathrust faults generates seismic activity from the scale of microseismic events (M<0) to greater than M of 9.0 (M 9.5 – 1960 Chilean earthquake; Stein et al., 1986). Seismically active subduction zones may cause catastrophic structural damage from ground motion and tsunamis. Therefore, understanding the mechanics of earthquakes, modeling past seismic events, and interpreting current subsurface structure and properties is vital for mitigating damage caused by future earthquakes.

This study aims to constrain the mechanical properties of megathrust plate boundary faults and surrounding rocks around the Nankai Trough. Seismic reflection surveys, well logging, and laboratory testing of rock samples are powerful tools to estimate mechanical properties at depth (Fig. 1). Seismic reflection surveys measure the strength of the acoustic signal (i.e. seismic waves) at a geophone or hydrophone that has been placed at a set distance from a source, such as an air gun, a vibrator, or dynamite. Seismic reflection profiles can display the entire plate interfaces in tens of kilometers scale, allowing us to interpret two- and three-dimensional structures. The seismic profile also displays positive and negative reflectors, which denote a change in acoustic

1
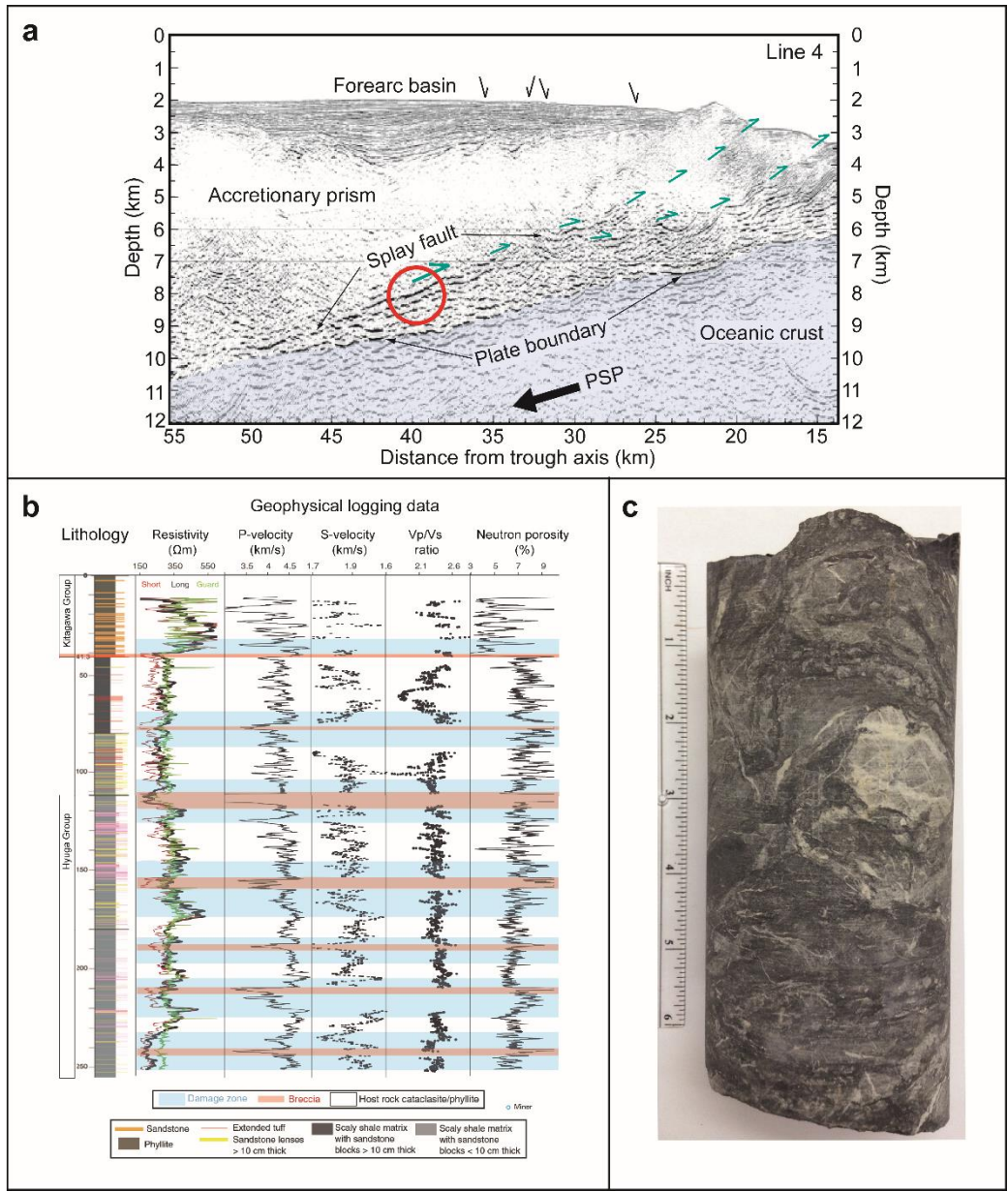
Fig. 1. (a) Poststack depth migrated profile showing the Nankai Trough (modified from Park et al., 2002). Vertical exaggeration is 2x. The red circle approximates the Nobeoka thrust pressure/temperature conditions when active. (b) Lithostratigraphic column and geophysical logging data of the Nobeoka thrust from the Nobeoka Thrust Drilling Project (NOBELL) (modified from Hamahashi et al., 2017). (c) An image of one of the NOBELL cores (core 204 – 204.83 mbgs [meters below ground surface]) that was utilized for experimental work.

impedance. From this change, we can interpret differences in mechanical properties at

depth, e.g. porosity, acoustic velocity, and bulk density.

2

Well logging with various tools at a borehole can directly measure the physical properties of neutron porosity, electric resistivity, seismic velocity, gamma ray, etc. These measured values generate a highly detailed profile of a single point within a target area. A detailed profile of the entire target area can be interpreted given an array of boreholes. Coring operation, often combined with well logging, can be utilized to gather rock samples from the subsurface. Although drilling technology exists that allows for deep water drilling in the Gulf of Mexico to crustal depths greater than 7 km (Close et al., 2008), scientific drilling to such depths for sample recovery is expensive. Thus another approach of determining mechanical properties is needed.

Another method is to collect samples from accessible outcrops similar to the target location and conduct laboratory experiments to measure their physical properties at elevated pressure and temperature that simulate the subsurface conditions. The ancient accretionary prisms were exhumed after being subducted at certain depths in the convergent plate margins and accessible on land (Fig. 2). The examples include: the Kodiak accretionary complex in Alaska, the Franciscan complex in California, and the Shimanto accretionary complex in Japan (Fisher and Byrne, 1987; Dumitru et al., 2010; Kimura et al., 2014). The physical and mechanical properties determined from experiments can be integrated with the data from well logging and seismic surveys to better understand mechanical properties of fault rocks, and thus deformation processes within subduction systems and slip behaviors along megathrust plate boundary faults.

Many studies have interpreted lithologies and mechanical properties from seismic data and well logs. Seismic profiles utilized in conjunction with acoustic velocity picks and known elastic moduli values have been used to interpret subsurface lithologies

(Christensen et al., 1999; Bauer et al., 2003). Experimental results on hand samples have been compared to well log estimates to determine the relationship between static and dynamic elastic moduli (McCann and Entwisle, 1992; Nedimović et al., 2003). In addition, well logs have been analyzed to determine the Young's modulus and shear modulus (Karacan, 2009).

The International Ocean Discovery Program (IODP) Nankai Trough Seismogenic Zone Experiment NanTroSEIZE) has attempted to drill through the plate boundary fault at seismogenic depth at ~ 5 km below sea floor, however, the deep drilling was extremely challenging and only achieved to drill to ~3 km depth (Tobin et al., 2019). Thus, still unknown are the lithologies and structures of the active fault zones and their mechanical and frictional properties (Fig. 2). In this study, the rock samples from the ancient Shimanto accretionary complex are used as analogue samples of the current Nankai subduction zones to characterize the static and dynamic elastic properties of rock samples and document the mechanical properties and seismic response (acoustic velocity) of different lithologies that likely exist along the thrust plate boundary faults at depth. At IODP Site C0012, a complete section of sediments and underlying basement materials of the Philippine Sea Plate were cored (Fig. 2) (Saito et al., 2010; Henry et al., 2012). The lithologies of the input materials to the Nankai subduction zone system includes hemipelagic mudstone, dark gray siltstone, siliciclastic, tuffaceous, and volcaniclastic sandstone, reddish brown calcareous claystone, turbidite facies, and basalt basement. The lithologies of the input materials are similar to those found in the Shimanto accretionary complex: light and dark gray sandstones, sandstone blocks within shales and tuff matrix, red brown shales, and turbidite sandstones.
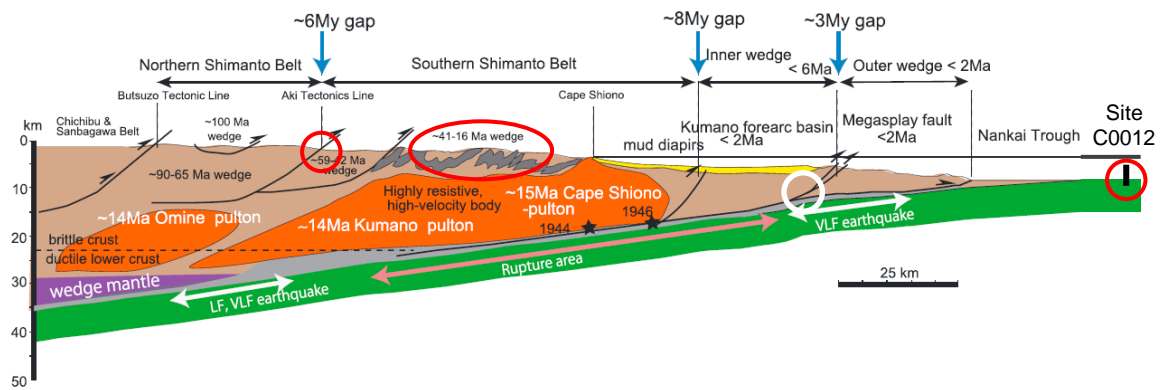
Fig. 2. Schematic cross section of the Shimanto accretionary complex to the Nankai Trough (modified from Kimura et al., 2014). Red and white circles signify the locations that samples were collected from and this study's target location of the active plate boundary fault, respectively.

2. GEOLOGIC BACKGROUND

2.1. Nankai Subduction Zone

The Nankai subduction zone is located offshore south Japan and results from the subduction of the Philippine Sea Plate beneath the Eurasian plate at a rate of approximately 4-6.5 cm per year to the northwest (Fig. 3) (Miyazaki & Heki, 2001; Seno, Stein, & Gripp, 1993).
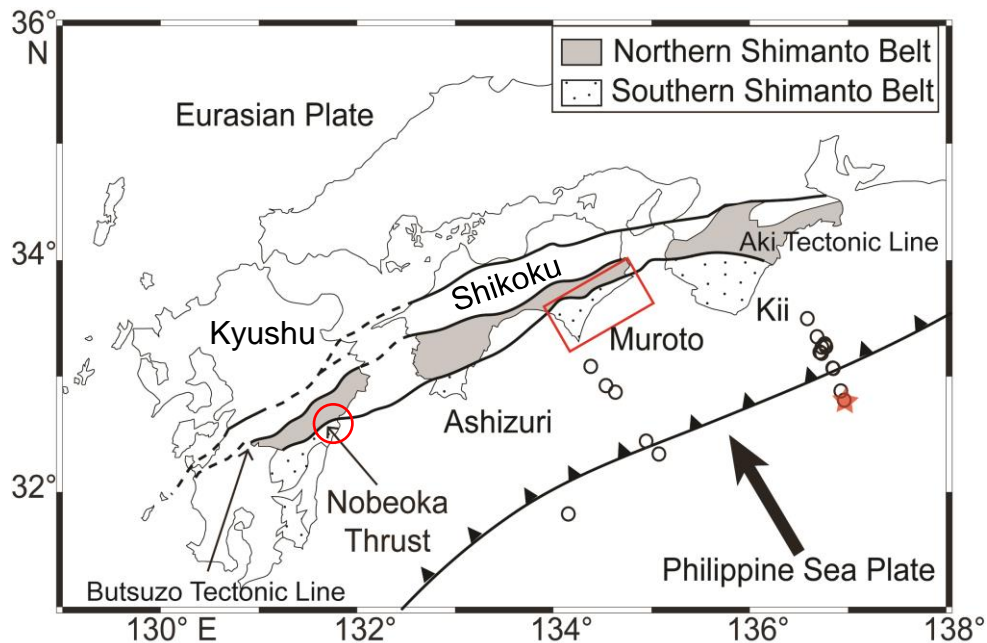
Fig. 3. Map of the Nankai Trough in southwest Japan (modified from Kitajima et al., 2017). The red box, circle, and star indicate locations of collected experimental samples.

The Nankai Trough has been extensively studied through offshore drilling (seismic reflection and gravity - Honda and Kono, 2005; Kimura et al., 2014; Kodaira et al., 2000, 2002, 2006; Park et al., 1999; pore pressure - Kodaira et al., 2004; structure - Moore et al., 1990; sediment properties - Karig, 1986). The studies reveal that the Nankai

subduction zone has a well-developed megasplay fault (Park et al., 2002; Moore et al., 2007), along which significant seismic ruptures occur. This subduction zone has societal impact because large earthquake rupture generates considerable tsunamis occurring every 100-200 years (Sagiya and Thatcher, 1999). The most recent events were the 1946 Nankaido (M 8.4), the 1944 Tonankai (M 8.1), and the 1854 Ansei-Nankai (M 8.5) (Ando, 1975). Recurring great earthquakes and tsunamis are a substantial threat to the populace living along the southwestern coast of Japan.

2.2. Shimanto Accretionary Complex

The Shimanto accretionary complex (SAC) is an ancient (early Cretaceous to Eocene age), exhumed accretionary prism that extends for over 800 km nearly parallel to the current Nankai Trough from central Japan to the Ryukyu Islands (Fig. 3) (Kimura & Mukai, 1991; Kondo et al., 2005; Kimura et al., 2014). This ancient accretionary complex is divided into a Northern and Southern Belt by the Aki Tectonic Line (Figs. 2 and 3).

2.2.1. Northern Cretaceous Shimanto Belt

The northern belt of the SAC is bounded by faults and further divided into four units, listed from north to south. The fault boundaries are the Butsuzo Tectonic Line to the north and the Aki Tectonic Line to the south (Fig. 3). The Hinotani unit is an early Cretaceous accretionary prism composing of slope sediments and coherent turbidites with no mélange present. The Akamatsu-Taniyama unit consists of a mélange with a terrigenous sediment matrix of Coniacian to Santonian age with Valanginian to Cenomanian chert and red shale blocks. The Hisawa unit contains conglomerates, massive sandstones, and alternating beds of sandstone and mudstone. At map scale, these strata are folded and faulted. The Mugi unit consists of a mélange with a terrigenous

7

sediment matrix of Campanian to Maastrichtian age with Albian to Cenomanian basalt, chert, and red shale blocks. The contacts between all adjacent units is a northward dipping, high angle reverse faults (Kimura & Mukai, 1991).

2.2.2. Southern Tertiary Shimanto Belt

The southern belt of the SAC is bounded by the Aki Tectonic Line to the north and the Pacific Ocean to the south (Fig. 3). The three units that compose the southern SAC are the Ohyama-misaki, Naharigawa, and Muroto (listed from north to south; Taira et al., 1982). The Ohyama-misaki unit is an Eocene formation that contains conglomerate, sandstone, and shale. The Naharigawa unit is also Eocene in age and consists of a flysch sequence of turbidite sandstones and shales. The Muroto unit is a Paleocene to early Eocene mélange complex with chert, tuff, and sandstone blocks within a shale and tuff matrix (Taira et al., 1982).

2.3. Nobeoka Thrust

The Nobeoka Thrust in Kyushu island and the Aki Tectonic Line in the Shikoku and Kii regions of Japan are major faults that bound the Cretaceous with minor Paleogene age northern and the Tertiary age southern portions of the Shimanto belt (Imai, 1971; Hashimoto et al., 2017) (Fig. 3). An excellent exposure of the Nobeoka Thrust can be found along the coastline of the eastern Kyushu (Fig. 3). The Nobeoka Thrust is nearly a pure dip-slip thrust with a SSE dip of approximately 10° between the Morotsuka and Kitagawa groups of the hanging wall in the north and the Hyuga group of the footwall in the south (Hamahashi et al., 2015). The hanging wall of the Nobeoka Thrust is composed of alternating layers of Eocene Kitagawa Group phyllitic shales and sandstones (Kondo et al., 2005). The shales were deformed by pressure solution while the sandstones and

8

mineral veins deformed via plastic flow and dynamic recrystallization of quartz aggregates (Hamahashi et al., 2015). The footwall of the Nobeoka Thrust consists of a mélange from the Eocene to early Oligocene Hyuga Group. The mélange has a shaly matrix containing sandstone and basaltic blocks that have experienced brittle deformation and pressure solution (Kondo et al., 2005). The footwall is more heavily deformed than the hanging wall, potentially due to the presence of more water during deformation, as evidenced by the pressure solution (Tsuji et al., 2006). The cataclastic fault core of the Nobeoka Thrust is at least 20 cm thick and up to 80 cm thick with the most common thickness being approximately 25 cm (Kimura et al., 2013; Hamahashi et al., 2015; Hashimoto et al., 2017). The cataclasite that constitutes the fault core originates from the footwall mélange (Hashimoto et al., 2017). Surrounding the fault core is a brittle shear zone several meters to several tens of meters thick in the hanging wall (Hamahashi et al., 2015; Kimura et al., 2013) and roughly 100 m thick in the footwall (Kondo et al., 2005; Yamaguchi et al., 2011). The folding and thrusting seen in the Nobeoka Thrust are evidence for horizontal shortening in shallow settings. The Kitagawa and Hyuga groups have experienced the maximum temperatures of 320 and 250°C, respectively, suggesting that the thermal gap was due to the fault being active as an out-of-sequence-thrust or megasplay fault with 8.6 to 14.4 km of displacement at up to 11 km depth below seafloor (Kondo et al., 2005).

2.4. Samples

To understand the mechanical behaviors of different lithology that potentially exist along the active plate boundary fault in the Nankai Trough, rock samples from the ancient Shimanto complex and relevant formations were used in this study (Fig. 4). The

samples used in this study were taken from the IODP Site C0012 on the Philippine Sea Plate offshore, and the Nobeoka Thrust and Shimanto accretionary complex (SAC) on land (Fig. 2 and 3). From the Site C0012, a slightly fractured, highly altered pillow basalt, hereafter referred to as basalt or Nankai basalt, from ~500 meters below sea floor was chosen (Fig. 4a). The lithology from the Nobeoka Thrust is footwall mélange, hereafter referred to as Nobeoka mélange, with a shaly matrix containing sandstone and basaltic blocks that have experienced brittle deformation and pressure solution (Fig. 4b). A fine-grained Shimanto sandstone that is light gray in color, hereafter referred to as (Shimanto) gray sandstone, several large and small cracks are present and filled with calcite and quartz, respectively (Fig. 4c). This sample is poorly sorted with a clay matrix of silt sized grains and sand sized grains of quartz and feldspar. A different Shimanto sandstone that is white in color, hereafter referred to as (Shimanto) white sandstone, mostly consists of quartz with a small portion containing hornblende, biotite, feldspar, muscovite, and clay (Fig. 4d). This sample is well sorted with sand sized grains and is also slightly fractured. A fractured mélange from the SAC, hereafter referred to as Shimanto mélange, contains a shaly matrix with predominantly calcite blocks (Fig. 4e). Shale from the SAC with a red coloration, hereafter referred to as red shale, consists of silt sized grains of red clay with small black inclusions (<1%) (Fig. 4f). The source material displays parallel fractures filled with calcite.
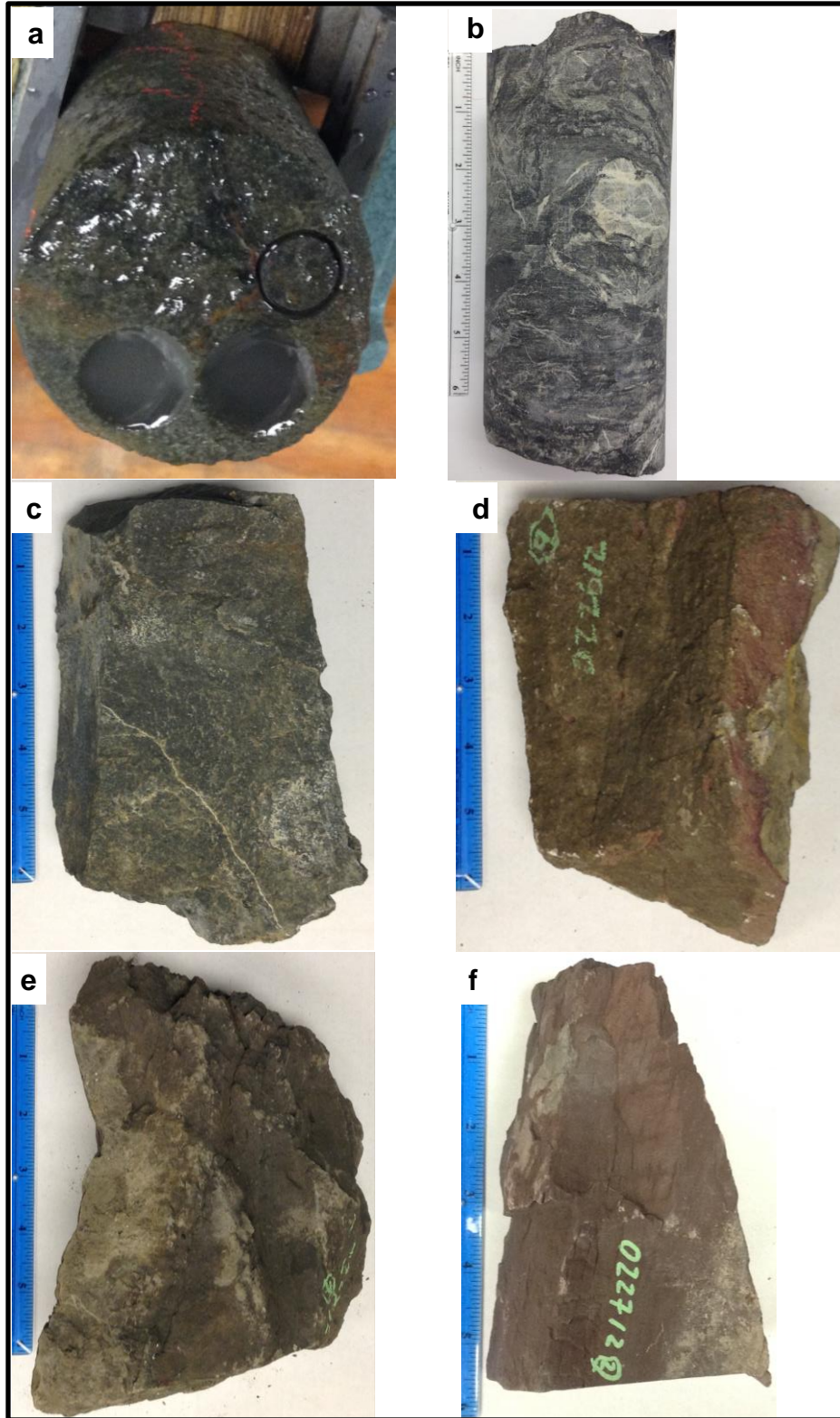
Fig. 4. Lithologies researched in this study: (a) Nankai Basalt, (b) Nobeoka mélange, (c) Shimanto gray sandstone, (d) Shimanto white sandstone, (e) Shimanto mélange, and (f) Shimanto red shale. Ruler displays inches.

3. METHODOLOGY

I prepared cylindrical specimens from various lithologies for testing. Porosity and density values for the cores were calculated using wet and dry mass measurements. Utilizing the cylindrical samples, I conducted three different experiments: (1) triaxial loading/unloading, (2) triaxial deformation tests, and (3) acoustic velocity tests. All work conducted in this thesis was completed in the John W. Handin Laboratory for Experimental Rock Deformation at Texas A&M University.

3.1. Sample Preparation

For this study, I prepared a total of 25 cylindrical specimens from 6 different lithologies (Table 1). 8 specimens are from basement basalt core obtained from the Integrated Ocean Drilling Program (IODP) Site C0012. Two specimens are from mélange in the footwall of the Nobeoka thrust, which was obtained in the onshore Nobeoka Thrust Drilling Project (NOBELL) from a depth of 203.83 – 204 meters below ground surface (mbgs). Additionally, 15 specimens are prepared from SAC blocks with different lithology collected from outcrops in Shikoku: two specimens from gray sandstone, eleven specimens from white sandstone, one specimen from red shale, and one specimen from mélange.

All specimens have a diameter of either 11.84 or 12.40 mm, with the exception of specimen Bas_A with a diameter of 12.70 mm (Table 1). From the drilled specimens, I cut and ground the ends of each specimen perpendicular to the cylindrical axis to ensure smooth and parallel surfaces. The final lengths for all specimens range from 19-27 mm (Table 1).

Table 1. Summary of experimental samples. Porosity values were calculated from measurements on wet and dry mass of cylindrical specimens.

Location	Source	Lithology	Sample	Length (mm)	Diameter (mm)	Initial mass (g)	Wet mass (g)	Dry mass (g)	Porosity (%)	Dry Bulk Density (g/cm^3)
Shikoku Basin	IODP Site C0012G, Core 10R-2, 107.5-116.5 cm, (597 mbsf)	Basalt	Bas_A	24.62	12.70	-	-	-	-	-
			Bas_B	25.53	11.84	-	7.572	7.165	14.49	2.55
			Bas_C	26.04	11.84	7.195	7.315	6.950	12.74	2.43
			Bas_D	25.76	11.84	7.165	7.260	6.930	11.65	2.45
			Bas_E	25.53	11.84	6.875	7.050	6.725	11.57	2.39
			Bas_F	24.77	11.84	6.430	6.685	6.240	16.33	2.29
			Bas_G	21.08	11.84	5.810	6.280	5.750	22.76	2.47
			Bas_H	25.40	11.84	7.000	7.120	6.770	12.52	2.42
Nobeoka Thrust	NOBELL Project, 203.3-204 mbgs	Mélange	NM_A	24.55	12.40	-	-	-	-	-
			NM_B	23.32	12.40	-	-	-	-	-
Shimanto Accretionary Complex, Shikoku outcrop	Sample 022512-3	Gray Sandstone	GS_A	26.47	11.84	7.650	7.660	7.630	1.03	2.61
			GS_A	26.42	11.84	7.610	7.620	7.580	1.37	2.60
	Sample 022612-9	White Sandstone	WS_A	24.56	11.84	-	7.115	6.970	5.34	2.57
			WS_B	26.62	11.84	-	7.670	7.600	2.38	2.58
			WS_C	25.93	11.84	-	7.430	7.370	2.09	2.57
			WS_D	23.37	11.84	-	6.650	6.580	2.71	2.55
			WS_E	24.03	11.84	-	6.840	6.780	2.26	2.55
			WS_F	27.74	11.84	7.825	7.865	7.815	1.63	2.55
			WS_G	24.84	11.84	7.075	7.155	7.075	2.91	2.58
			WS_H	19.84	11.84	-	-	-	-	-
			WS_I	19.99	11.84	-	-	-	-	-
			WS_J	26.44	11.84	7.545	7.625	7.530	3.25	2.58
			WS_K	21.92	11.84	-	-	-	-	-
	Sample 022712-2	Red Shale	RS_A	25.78	11.84	-	7.770	7.640	4.56	2.68
	Sample 022712-5	Mélange	SM_A	23.93	11.84	-	-	-	-	-

3.1.1. Porosity and Density Measurements

Porosity of specimens was determined by two methods: (1) measurements of wet mass, dry mass of cylindrical sample and (2) measurements of wet mass, dry mass, and solid volume. In the first method, diameter and length of the specimen were measured to compute the specimen volume. Specimen was saturated with distilled water in a desiccator under vacuum for 24 or 48 hours, depending on lithology: 24 hours – sandstone and basalt, 48 hours – mélange and shale. After saturation, excess water from the surface of the specimen were removed to measure the wet mass (m_{wet}). Then, the specimen was dried in an oven at 110˚C for 24 or 48 hours, depending on lithology: 24 hours – sandstone and basalt, 48 hours – mélange and shale, to measure the dry mass (m_{dry}). From the measured values of wet mass and dry mass, porosity (φ) was calculated using an equation,

$$\varphi = \frac{m_{wet} - m_{dry}}{\rho_{water}} / V_{tot} \tag{1}$$

where ρ_{water} is the density of water (assumed to be 1.0 g/cm^3), and V_{tot} is the total volume of the sample (Table 1). Dry bulk density (ρ_{dry}) was calculated utilizing Equation 2.

$$\rho_{dry} = m_{dry} / V_{tot} \tag{2}$$

In the second method, solid volume was measured using the Quantachrome gas pycnometer, which consists of two chambers of known volume (sample and reference chamber) attached to a Helium (*He*) gas cylinder. *He* gas was utilized because *He* gas is the inert gas with the smallest molecules. The sealed sample chamber was pressurized to a target pressure with the *He* gas. A valve was then opened to allow the gas to expand

14

into the reference chamber until the pressure equalized. The pressure drop was then used

to measure the solid volume of the specimen. Porosity was calculated from

$$\varphi = \frac{m_{wet} - m_{dry}}{\rho_{water}} \Big/ \Big(\frac{m_{wet} - m_{dry}}{\rho_{water}} + V_{solid}\Big) \tag{3}$$

where V_{solid} is the solid volume measured by the pycnometer (Table 2).

Table 2. Pycnometer measurements and calculated densities.

Lithology	Specimen	Dry mass (g)	Wet mass (g)	Dry solid volume (cm³)	Grain density (g/cm³)	Porosity	Wet bulk density (g/cm³)
Basalt	Bas_H	2.046	2.139	0.7545	2.713	0.1102	2.52
Shimanto mélange	SM_Ba	5.164	5.281	1.992	2.954	0.0554	2.51
	SM_Bb	4.116	4.214	1.510	2.712	0.0616	2.66
Red Shale	RS_A	4.093	4.143	1.516	2.700	0.0319	2.66
Gray sandstone	GS_B	3.300	3.331	1.290	2.559	0.0229	2.52
White sandstone	WS_F	2.090	2.111	0.7721	2.708	0.0261	2.66
	WS_G	1.564	1.579	0.6044	2.587	0.0250	2.55

3.1.2. Local Strain Measurements

Prior to experiments, two or three 350 Ω resistance strain gauges were mounted to

the specimen to measure local strain (Fig. 5c, Table 3). All triaxial loading/unloading

experiment specimens, and the white sandstone specimen of the triaxial deformation

experiments deformed at 80 MPa, had strain gauges applied. None of the acoustic

measurement cores had strain gauges applied.

All strain gauges used in this study were obtained from Micro-Measurements.

They include two different types: a tee rosette pattern strain gauge and a linear pattern

strain gauge (Fig. 5c). The tee rosette pattern strain gauge measured local strain along

two perpendicular axes, whereas the linear pattern strain gauge measured local strain

along one axis. Throughout this study, a combination of different sizes of both tee rosette

pattern and linear pattern strain gauges were used. There were two different tee
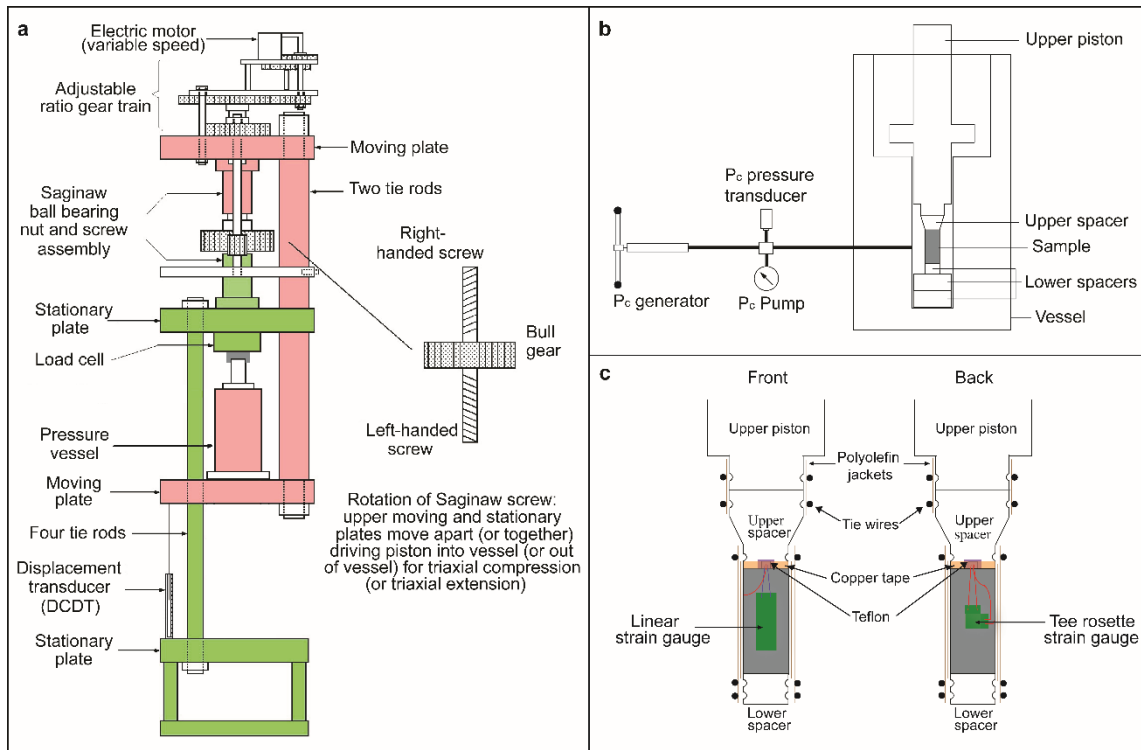
Fig. 5. (a) A schematic of the Large Sample Rig (LSR) in the John Handin rock deformation laboratory at Texas A&M. (b) A schematic of the pressure vessel used for all experiments on the LSR. (c) A schematic of the sample for loading/unloading experiments.

rosette strain gauges (125 UT and 125 WT) and two different linear strain gauges (250 UT and 250 UW). The tee rosette strain gauges were the 125UT and 125WT patterns. The 125 UT pattern is two small grids adjacent to each other and does not measure the strain over the same area, whereas the 125WT pattern is two small grids that overlap each other. The 125 WT was used for most of the experiments except the two experiments of Bas_A-1 and NM_B-1.

Different linear strain gauges were selected to maintain the surface area as close as the tee rosette strain gauge area. The 250UW and 250UN linear strain gauges have a

16

Table 3. Strain gauge configuration for each experiment.

Sample	Experiment #	Experiment Type	Linear (axial)	Linear (radial)	Tee rosette (axial)	Tee rosette (radial)
Bas_A	1		250UW	250UW	125UT	125UT
Bas_B	1	Load/unload	250UW	-	125WT	125WT
	2 and 3		250UN	-	125WT	125WT
NM_B	1	Load/unload	250UW	250UW	125UT	125UT
RS_A	1	Load/unload	250UN	250UN	125WT	125WT
SM_A	1	Load/unload	250UW	-	125WT	125WT
WS_A	1 and 2	Load/unload	250UW	-	125WT	125WT
	80 MPa	Deformation	250UW	-	125WT	125WT
GS	all	Load/unload	250UN	-	125WT	125WT

single grid with approximately three and two times as the grid area of the 125WT pattern, respectively. The experiment with the 250 UW (e.g., Bas_B-1) shows greater difference (more than 10%) in Young's modulus between the linear and tee rosette Young's modulus, whereas the experiment with 250 UN (e.g., Bas_B-2) shows less than 10% difference. Therefore, the 250UN pattern is applied to most of the cores as supplies were available.

The strain gauge configuration on the specimen was either: (1) two linear and one tee rosette strain gauges or (2) one linear and one tee rosette strain gauges (Figure 4c). For configuration 1, one of the linear pattern strain gauges was oriented parallel to the cylindrical axis to measure axial strain while the other was oriented perpendicular to the cylindrical axis to measure radial strain. The tee rosette pattern strain gauge was oriented to measure both the axial and radial strain. For configuration 2, the linear pattern strain gauge was oriented parallel to the cylindrical axis to measure axial strain, and, as in the first case, the tee rosette pattern strain gauge was oriented to measure both the axial and radial strain. Configuration 2 was the most frequently used.

17

The strain gauges were applied using the standard procedure. I first smoothed the core face with 2000 grit sandpaper. Second, I cleansed the surface with M-Prep Conditioner A and M-Prep Neutralizer 5A to remove any particulates. Third, I primed the core surface with 200 Catalyst-C to ensure that the adhesive would function properly. Fourth, I applied the M-Bond 200 Adhesive and set the strain gauge by holding the strain gauge to the sample for five minutes. Fifth, I placed a heat-resistant coating of polyurethane over the strain gauge grids to prevent damage during the soldering phase. Finally, I soldered wires to the strain gauge with a 60/40 tin/lead solder.

3.2. Experiments

Three kinds of experiment were conducted on the dry cores: (1) triaxial loading/unloading, (2) triaxial deformation tests, and (3) acoustic velocity tests. Triaxial deformation experiments (1 and 2) and acoustic velocity tests (3) were conducted using a large sample rig (LSR) and a petrophysics measurement system, respectively, in the John W. Handin Laboratory for Experimental Rock Deformation (Fig. 5). All experiments were conducted on dry samples at room temperature and humidity conditions. No pore fluid pressure was applied on any experiment.

The LSR frame has a unique yoked configuration, which includes moving and stationary frames, and the originally-designed pressure vessel with two loading pistons at the top and bottom can keep the volume of the confining pressure medium during the triaxial loading (Fig. 5a; Logan, 1972). Because the originally-designed pressure vessel was not currently available, a modified configuration was used for this study. A pressure vessel with a single loading piston was placed on the moving plate. The moving plate is shifted by a variable speed electric motor with an adjustable gear train to better control

displacement rate. The LSR system measures axial load, axial displacement, and confining pressure. The load cell, located on the stationary plate, measures the axial load from both the piston and the confining pressure and can therefore measure differential load. Displacement of the moving plate is measured by a linear variable differential transformer (LVDT). Confining pressure is measured by a pressure transducer located in the confining pressure system.

The confining pressure system utilizes a confining fluid reservoir, a hand-operated pump for pressurization, and a Riken pressure generator (screw-driven) for fine pressure generation and control during experimentation. Pressure transducers are used to convert the confining fluid pressure to an analog signal that is read off by an analog pressure gauge.

3.2.1. Triaxial Loading/Unloading Tests

The triaxial loading/unloading experiments were conducted to determine the static elastic moduli. Each specimen was placed between spacers, and attached to the upper piston (Fig. 5). Two layers of polyolefin jackets were used to isolate the core from the confining fluid and secured with tie wires at the ends. The upper spacer was notched to prevent the strain gauge wires from pinching, and the notch was covered by Teflon and copper tape inside the polyolefin jackets (Fig. 5c).

The specimens were subjected to confining pressures between 5 and 80 MPa, incremented stepwise (5-10-20-40-60-80-40-20-10 MPa) utilizing oil as the confining fluid. At each confining pressure, the motor is turned on to start moving the vessel and frame at a displacement rate of 0.25 µm/s until finding the hit point (initiation of load increase) of the sample, loading the sample at a displacement rate of 0.25 µm/s until

LVDT axial strain reached ~0.5%, and unloading the sample till ~0.025 mm beyond the hit point. The LVDT axial strain was kept below ~0.5% to ensure that all deformation remained in the elastic regime. After each cycle, the confining pressure was adjusted to the next step, and the process repeated. Each iteration lasted ~30 minutes.

Total load, axial displacement, confining pressure, room temperature measured by a K-type thermocouple, and strains measured by the strain gauges were recorded digitally using Labview software. Because the axial force was measured on the external load cell, the differential load was calculated by subtracting the load induced by confining pressure from the measured axial force. The true displacement of the specimen was calculated by subtracting the rig distortion from the measured displacement. Rig distortion (*rd*) was calculated from:

$$rd = \frac{differential\ load}{k} \tag{4}$$

where *k* is the rig stiffness (1.1 x 10^6 lb/in). Linear rig stiffness is assumed in this study. The true sample area of the specimen was calculated by dividing the undeformed specimen area by one minus the axial strain, assuming that total volume is not changed during deformation. Using the true sample area and the differential load, the differential stress was calculated for the experiment. For each load/unload iteration, the displacement and strain were adjusted to zero at the hit point to simplify calculations and improve graphing.

The Young's modulus was calculated from the slope of the relation of stress and axial strain utilizing an equation,

$$E = \frac{\Delta\sigma}{\Delta\varepsilon_{ax}} \tag{5}$$

where E is the Young's modulus, $\varDelta\sigma$ is the change in differential stress, and $\varDelta\varepsilon_{ax}$ is the change in axial strain. Both tee rosette and linear pattern axial strains were used whenever available. Axial displacement measured by LVDT were also utilized to calculate axial strain and the Young's modulus for comparison. The Poisson's ratio (v) was calculated by dividing the slope determined on the differential stress-axial strain curve by the slope determined on the differential stress-radial strain curve for the same portion of the loading curve to yield:

$$v = \left. \frac{\frac{\Delta\sigma}{\Delta\varepsilon_{ax}}}{\frac{\Delta\sigma}{\Delta\varepsilon_{rad}}} \right. = \frac{\Delta\varepsilon_{rad}}{\Delta\varepsilon_{ax}} \tag{6}$$

where $\varDelta\varepsilon_{rad}$ is the change in radial strain. Different combinations of axial and radial strain measurements generated different Poisson's ratios depending on availability of both tee rosette and linear pattern axial and radial data.

The other elastic moduli (bulk modulus, Lamé's first parameter, shear modulus, and P-wave modulus) were calculated from the Young's modulus and Poisson's ratio, assuming the core is a homogeneous, elastic solid:

$$K = \frac{E}{3(1-2v)} \tag{7}$$

$$\lambda = \frac{Ev}{(1+v)(1-2v)} \tag{8}$$

$$G = \frac{E}{2(1+v)} \tag{9}$$

$$M = \frac{E(1-v)}{(1+v)(1-2v)} \tag{10}$$

where K is the bulk modulus, E is the Young's modulus, v is the Poisson's ratio, λ is Lamé's first parameter, G is the shear modulus, and M is the P-wave modulus.

3.2.2. Triaxial Deformation Tests

Triaxial deformation experiments were conducted to determine the fracture strength and mode of failure at different confining pressures. The sample configuration was the same as those for triaxial loading unloading experiments except strain gauges were not attached to the specimen in most of the deformation tests. The specimens were deformed at a constant confining pressure ranging between 5 and 80 MPa, increasing sequentially (5-10-20-40-80 MPa). If the specimen experienced transitional or ductile mode deformation at a confining pressure below 80 MPa, no higher pressure experiments were conducted on that lithology. The specimens were deformed at a constant displacement rate of 0.25 µm/s. Once the steady state was achieved, the specimen was unloaded followed by depressurization of confining pressure.

3.2.3. Ultrasonic Velocity Measurements

Dynamic elastic moduli were determined through acoustic velocity experiments. The lithologies with the greatest and least pressure dependence, as demonstrated by the static results, were chosen for acoustic experiments.

Specimens were held in place between two sample holders within a pressure vessel (Fig. 6) by a double jacket of polyolefin and secured with tie wire to isolate the sample from the confining pressure media (oil). Each sample holder incorporated one 500 kHz lead-zirconate-titanate (PZT) transducer: one of which was connected to the input pulse, while the other was connected to an oscilloscope to record and display the received acoustic waveform. The sample holder configuration was placed within a pressure vessel and experimentation commenced.
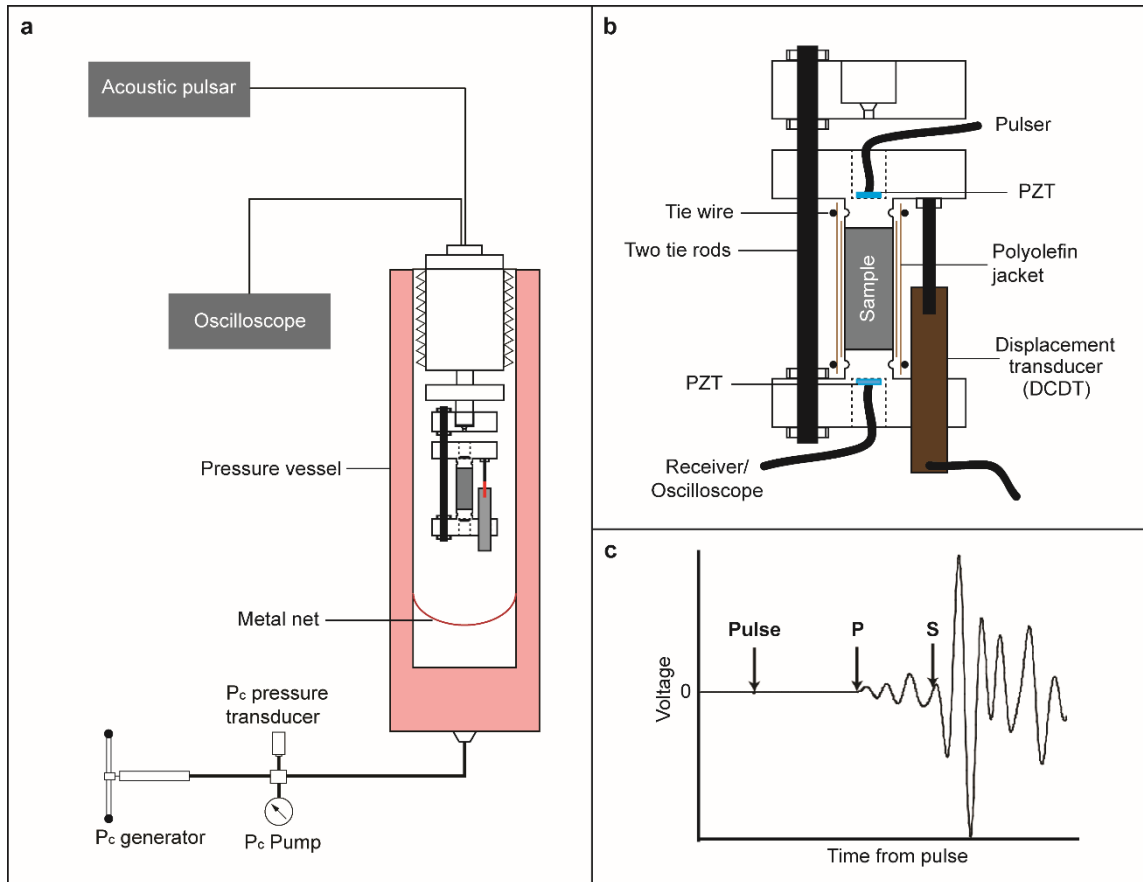
Fig. 6. (a) Schematic of the petrophysics measurement system in the John Handin rock deformation laboratory. (b) Schematic for the sample holder. (c) Example waveform output for the acoustic pulsar tests, showing P- and S-wave determinations (modified from Carpenter et al.*,* 2014).

The petrophysics measurement system measures displacement, confining pressure, temperature, and acoustic waveform. Displacement is measured by the LVDT attached to the sample holders. Specimens were held in place between two sample holders within a pressure vessel surrounded by a layer of double polyolefin jackets that are secured with tie wire (Fig. 6b). One of the transducers was connected to the input pulse and the other was connected to an oscilloscope to record and display the received acoustic waveform through the sample. The confining pressure system utilizes a confining fluid reservoir, an air driven pump for pressurization, and a High Pressure

23

Equipment pressure generator (screw-driven) for fine pressure generation and control during experimentation.

The specimens were subjected to similar confining pressure steps as used in the triaxial loading/unloading experiments (5-10-20-40-60-80-60-40-20-10 MPa). At each confining pressure, a sonic pulse was generated by an internal trigger with a repetition rate of 100 Hz, transducer operating frequency of 0.5 MHz, and an output amplitude of 0 dB. After the waveform was saved, the confining pressure was adjusted and the process repeated.

Due to the transducers not being directly connected to the specimens, travel time through sample holders and system was calibrated at each confining pressure step. To measure this travel time, first arrivals of aluminum specimens of three different lengths (12.70, 25.43, and 38.12 mm) were determined. By plotting the determined travel times against the specimen length, the y-intercept was estimated to be the travel time differential of the acoustic pulse through the sample holder (Table 4).

Table 4. Travel time difference due to the sample holders at different confining pressures.

Pc (MPa)	Δt system (μs)
5	4.25
10	4.17
20	4.42
40	4.66
60	4.17
80	4.07
60	5.95
40	4.26
20	5.12
10	4.36

Confining pressure, sample displacement, and temperature were recorded digitally using Labview software. The waveform was received by an oscilloscope set to a record

length of 100 µs, and sample interval of 40 ns (Fig. 7).

Acoustic velocities were determined from the first arrivals and the measured sample length (Fig. 7). Sample length was reduced by the displacement experienced due to increased confining pressure. Acoustic travel time was determined by

$$Velocity = (l_{sample} - \Delta l)/(\Delta t_{measured} - \Delta t_{system}) \tag{11}$$

where l_{sample} is the length of the sample, Δl is the displacement, $\Delta t_{measured}$ is the first arrival of the waveform, and Δt_{system} is the travel time through the system and sample holders. System travel time (Table 4), the time the sonic pulse travels through the steel sample holder before and after traveling through the specimen, demonstrated no correlation with confining pressure. To improve calculations, a range of first arrivals was taken. Therefore, minimum and maximum possible acoustic velocities were determined at each confining pressure.
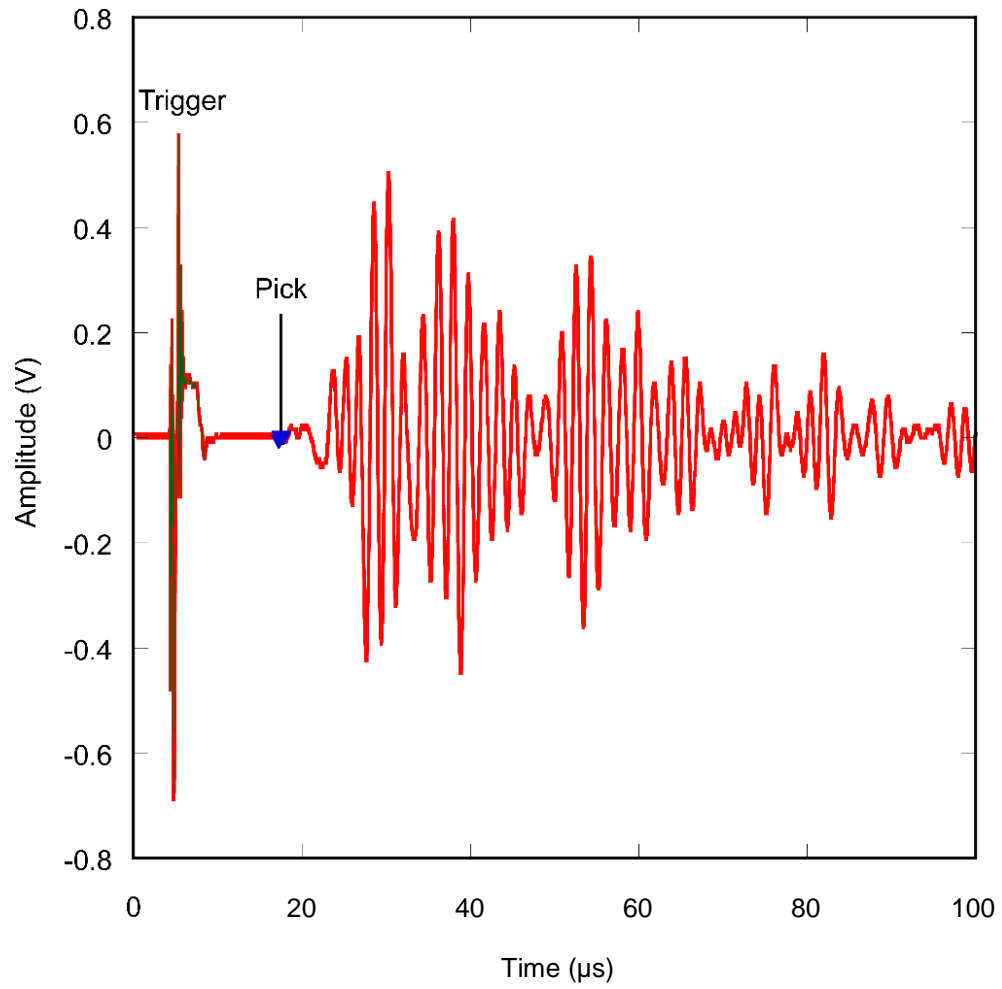
Fig. 7. Acoustic waveform of white sandstone at 80 MPa. The trigger has a green shading, and my picks are blue triangles.

4. RESULTS

4.1. Triaxial Load/Unload Tests

For each iteration of all triaxial load/unload experiments, differential stress as a function of both axial stress and radial strain was plotted to determine Young's modulus and Poisson's ratio (Fig. 8). During the loading path, stress-strain curve shows a non-liner behavior followed by a linear behavior as load becomes higher. Once the unloading is started, a rapid decrease in differential stress changed to a linear stress-strain behavior followed by a non-linear behavior at the lower load. The non-linear behavior observed at smaller load likely reflects a nonlinear elastic behavior present in the loading system components (frame, piston, spacers, etc.) and an elastoplastic behavior of the rock sample (e.g., the closing of the pores within the sample). The differential load at the end of unloading path is smaller than that at the beginning of the loading path. This difference in differential load reflects the O-ring friction. Because the axial load was measured on the external load cell, the determined differential stress includes the O-ring friction. Because the O-ring frictional force is applied in opposite direction between in loading and unloading, a sudden drop in differential load is observed when the loading direction is switched. Thus, the difference in the differential load between the loading and unloading paths corresponds to twice the O-ring friction (Fig. 8a). To account for the O-ring friction and non-linear behaviors, the unloading curve was shifted and the differential stress ranging between 35-70% of the maximum stress was used to determine the elastic properties (i.e., slope in stress-strain curves) (Fig. 8b). Because some of the non-linear behavior of the rock specimen (e.g., closure of pore space, cracks) is not recoverable, the

27
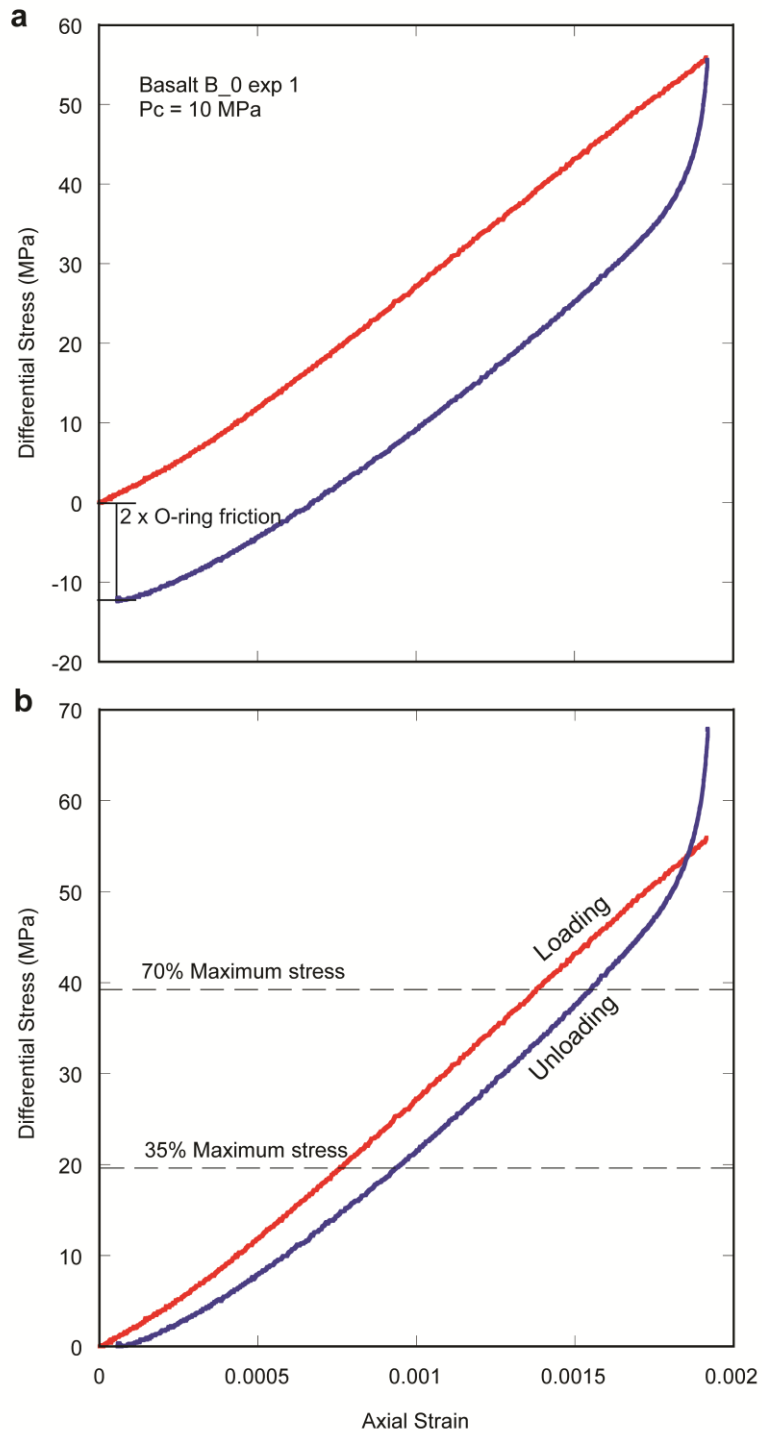
Fig. 8. a) Uncorrected and (b) corrected stress-strain curve for experiment Bas_A-1 at P_c = 10 MPa. The unloading curves were shifted to correct for O-ring friction.

elastic moduli values determined from the unloading path was presented in most of the figures and used for analysis shown in this thesis. Table 5 includes the values determined from the loading path also for reference.

In general, all of the tested samples exhibit that both the Young's modulus and Poisson's ratios determined from strain gauges increase systematically with increasing confining pressure; Young's modulus and Poisson's ratio increase from 13-70 GPa and 0.068 to 0.200, respectively, during pressurization of confining pressure (P_c) from 5 to 80 MPa (Figs. 9–14, Table 5). It should be noted that some of the experiments have incomplete datasets due to either jacket failure, loss of signal from the strain gauge during the experiment, lack of the necessary strain gauge, or change in experiment type.

Young's modulus of basalt determined from the strain gauges increases from 28.38-36.33 GPa at P_c = 5 MPa to 35.68-38.10 GPa at P_c =80 MPa (Fig. 9a). During depressurization, it decreases to 30.38-32.22 at P_c = 10 MPa. Poisson's ratio of basalt differs from the general trend: the values derived from the unloading curve continue to increase during depressurization. Poisson's ratio of the basalt increases from 0.198-0.226 at P_c = 5 MPa to 0.214-0.228 at P_c = 80 MPa (Fig. 9b), although exceptionally high and low values are observed in the test on Bas_A-1 sample measured by sets of (1) a linear axial strain gauge and a linear radial strain gauge (Bas_A-1 lin/lin) and (2) a linear axial strain gauge and a rosette radial strain gauge (Bas_A-1 lin/ros). During depressurization, the Poisson's ratio continues to increase from 0.214-0.221 at P_c = 80 MPa to 0.220-0.223 at P_c = 10 MPa and (Fig. 9b). Experiment Bas_A-1 exhibits a decrease in Poisson's ratio with increasing P_c; Bas_A-1 lin/lin decreases from 0.291 P_c = 5 MPa to 0.272 at P_c = 20 MPa, and Bas_A-1 lin/ros decreases from 0.142 P_c

29
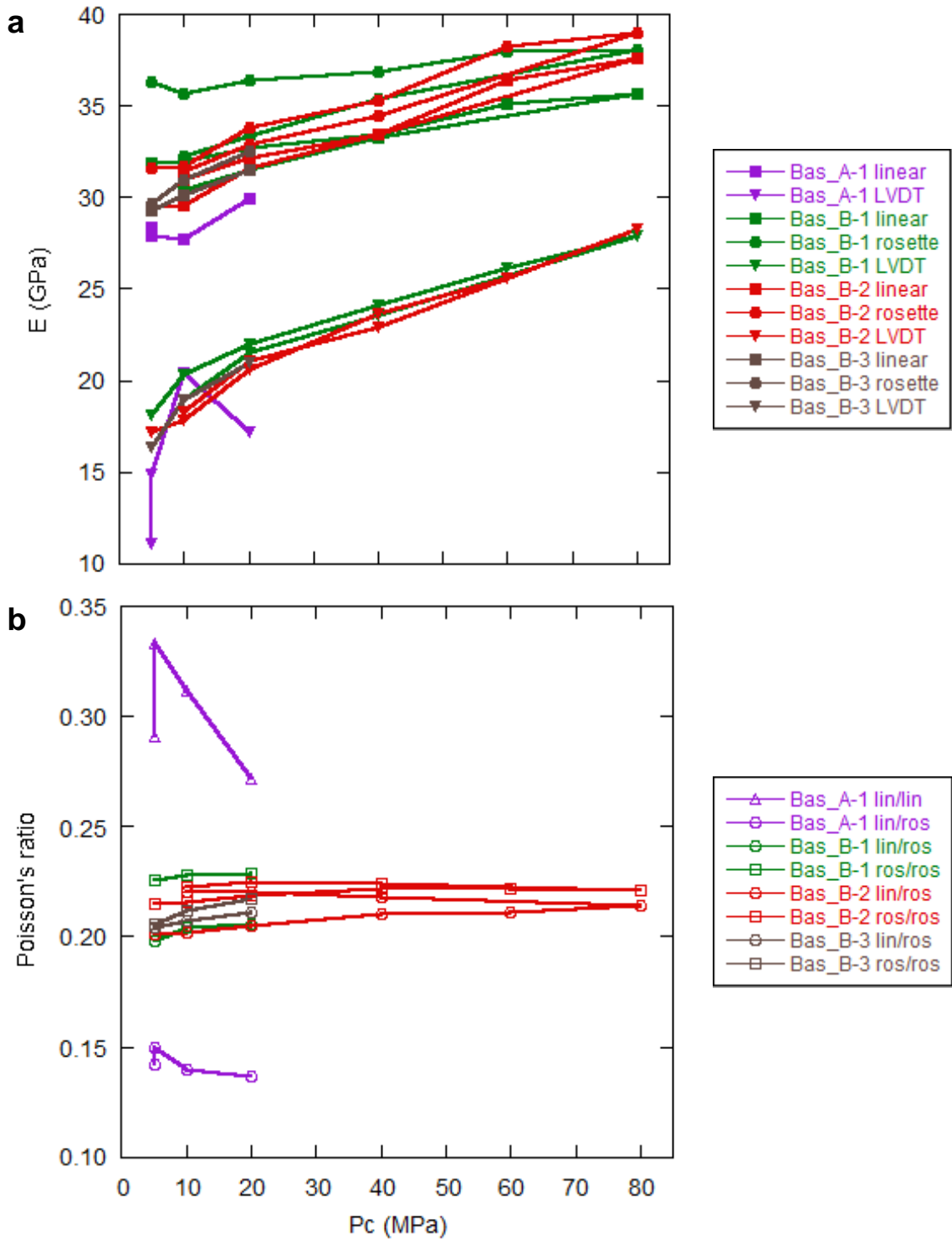
Fig. 9. (a) Young's modulus and (b) Poisson's ratio for basalt. Different colors represent different experiments and different symbols represent different sources of the data. For the Poisson's ratio, the combination of sources for axial strain and radial strain are labeled. Experiment Bas_A-1 failed in pressurization of P_c from 20 to 40 MPa, and experiment Bas_B-1 lost rosette radial strain gauge signal in pressurization of P_c from 20 to 40 MPa.

30
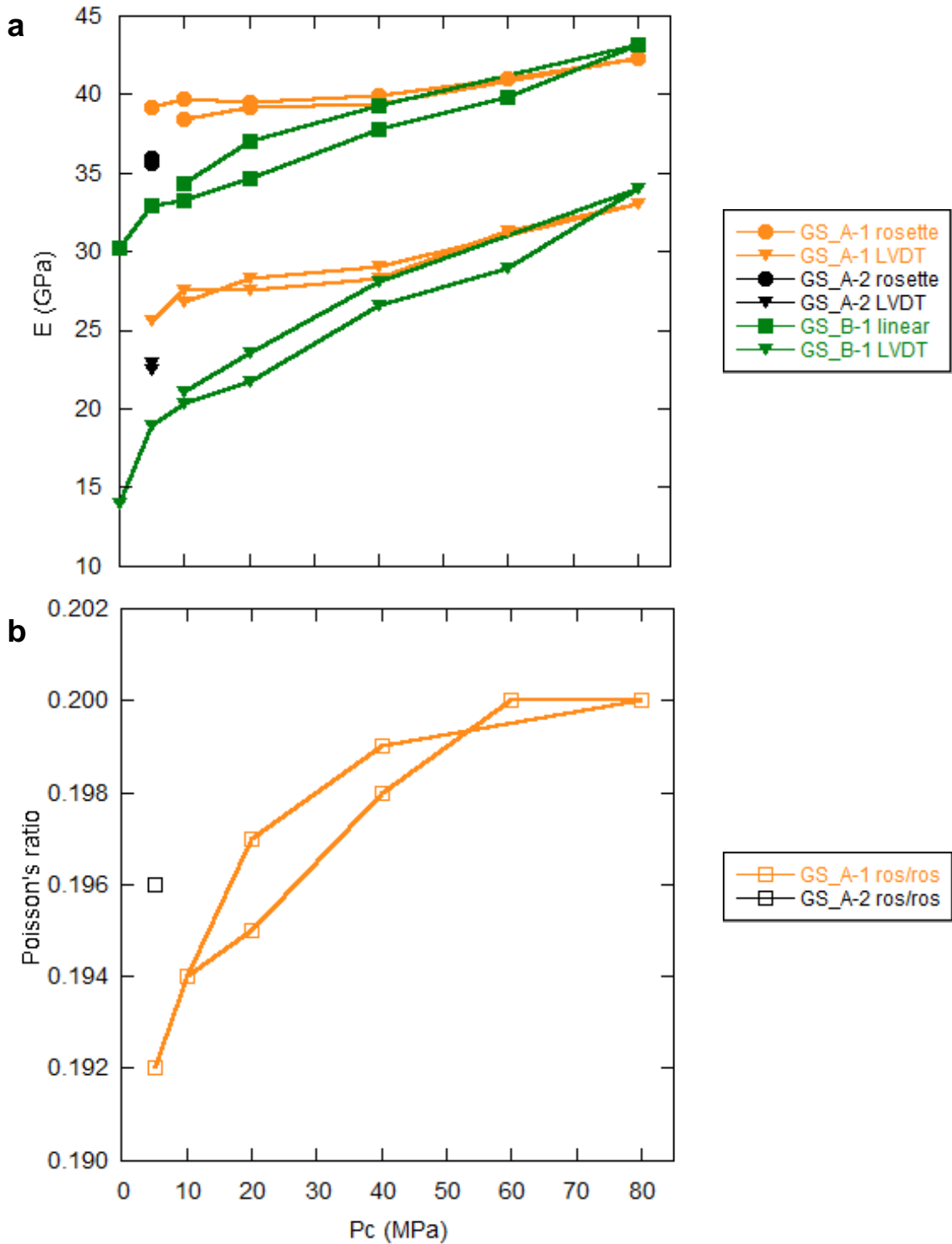
Fig. 10. (a) Young's modulus and (b) Poisson's ratio for Shimanto gray sandstone. Different colors represent different experiments and different symbols represent different sources of the data. For the Poisson's ratio, the combination of sources for axial strain and radial strain are labeled. Experiments GS_A-1 and GS_A-2 experienced wire failure in the linear axial strain, failing to record for that strain gauge. Experiment GS_B-2 had wire failure for the tee rosette radial strain.

31
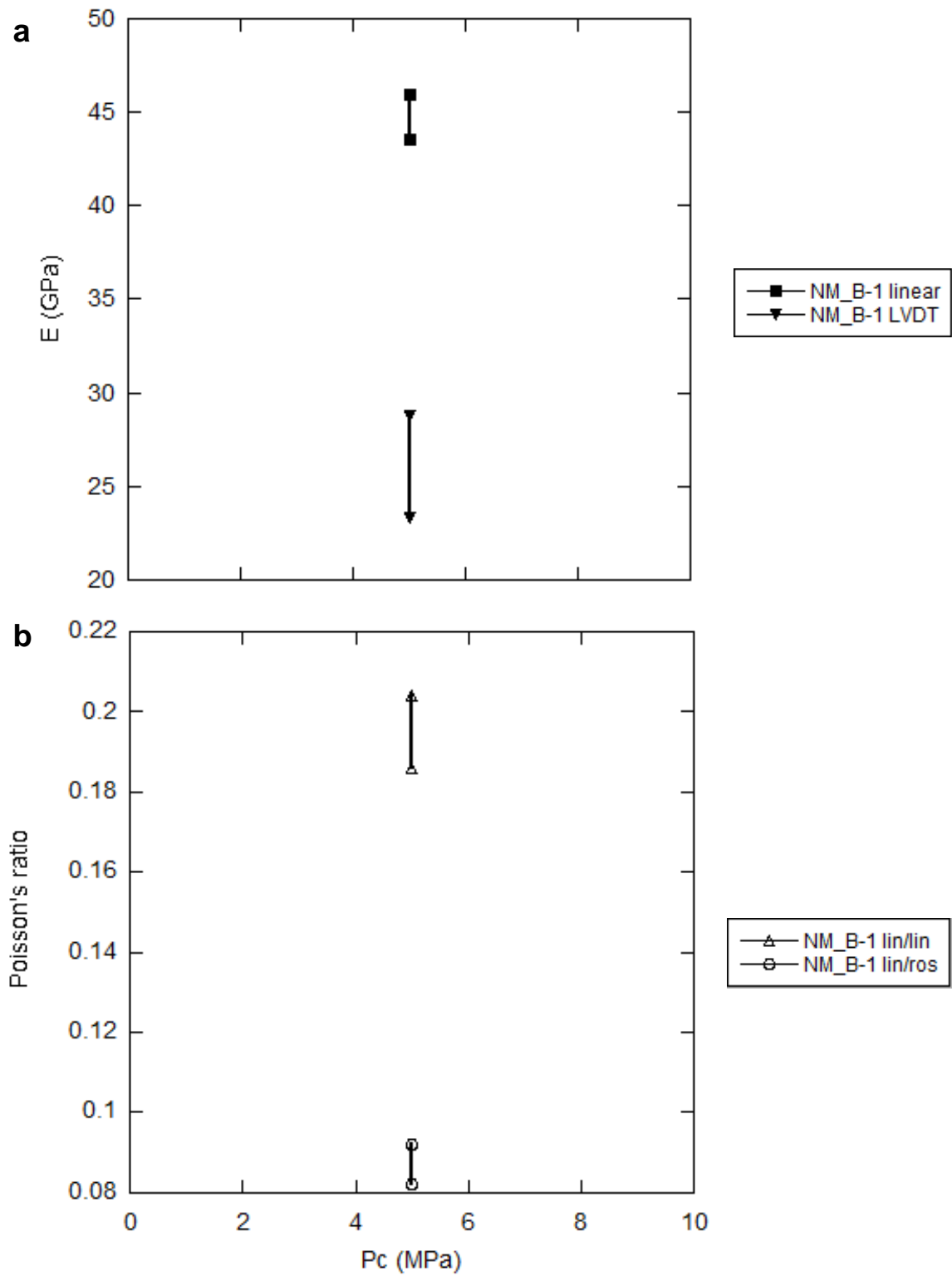
Fig. 11. (a) Young's modulus and (b) Poisson's ratio for Nobeoka mélange. Experiment NM_B-1 failed in pressurization of P_c from 5 to 10 MPa. Two iterations at P_c = 5 MPa are presented.
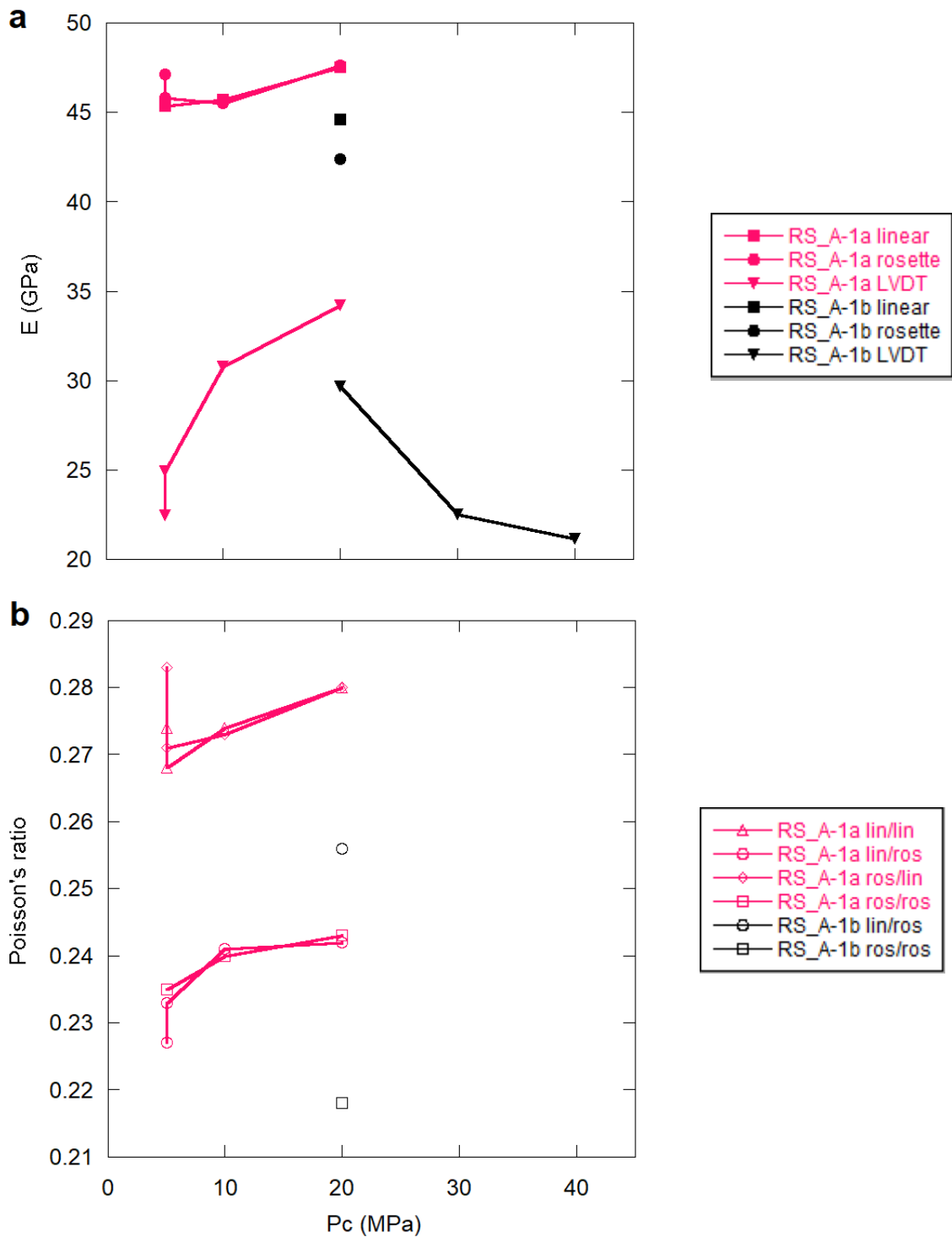
Fig. 12. (a) Young's modulus and (b) Poisson's ratio for Shimanto red shale. Experiment RS_A-1a terminated early due to time constraints. Experiment RS_A-1b had wire failure for the linear radial strain during pressurization to 20 MPa, lost all strain gauge signal during pressurization from 20 to 30 MPa, and failed during pressurization from 40 to 60 MPa. Experiment 1b is a continuation of experiment 1a and was pressurized to 20 MPa for the first iteration.
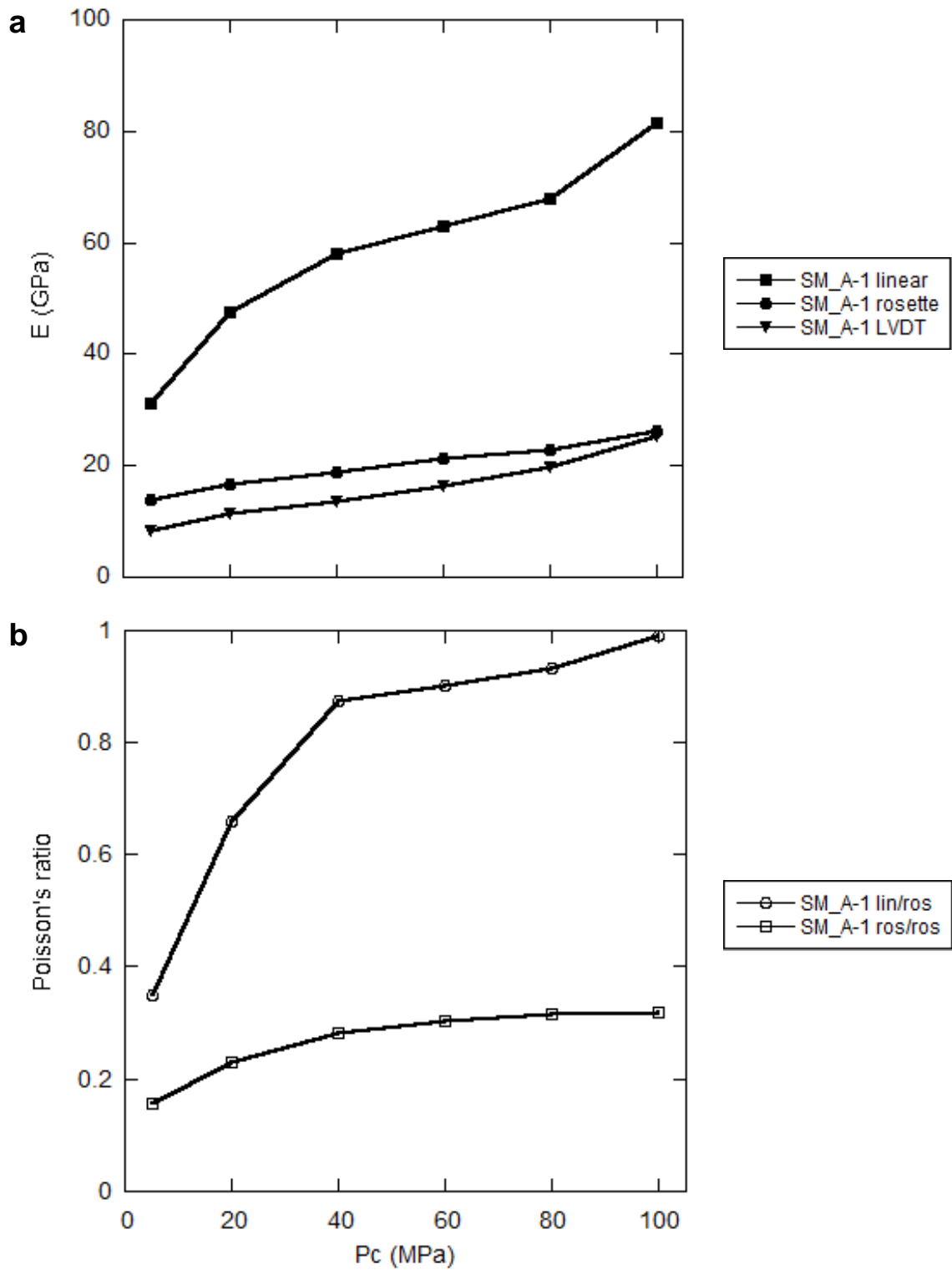
Fig. 13. (a) Young's modulus and (b) Poisson's ratio for Shimanto mélange. Experiment SM_A-1 failed during depressurization.
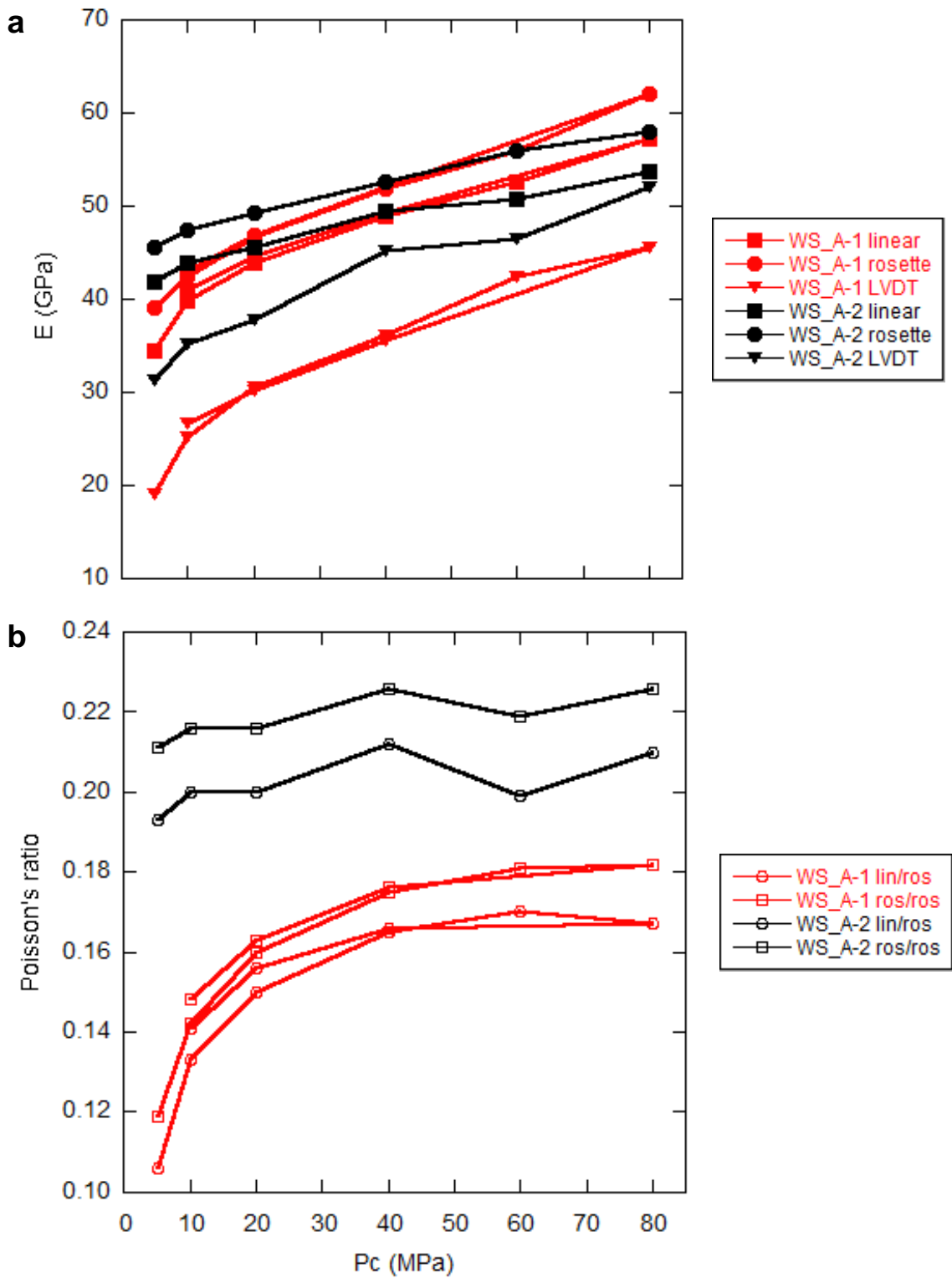
Fig. 14. (a) Young's modulus and (b) Poisson's ratio for Shimanto white sandstone. Experiment WS_A-2 has no data during depressurization because the triaxial deformation test was conducted at P_c = 80 MPa right after the load/unload test at the same pressure.

35

Table 5. Elastic moduli measurements from loading/unloading experiments on the LSR. **L** and **UL** represent the data in loading and unloading, respectively. **lin** and **ros** represent the strain gauge types of linear strain gauge and tee rosette strain gauge, respectively. For Poisson's ratio, the combination of strain gauge sources is listed for axial strain/radial strain. For example, **ros/lin** represents axial strain of a rosette strain gauge and radial strain of a linear strain gauge.

Sample	Experiment #	P_c (MPa)	Young modulus, E (GPa)						Poisson's ratio v							
			L, LVDT	UL, LVDT	L, lin	UL, lin	L, ros	UL, ros	L, lin/lin	UL, lin/lin	L, lin/ros	UL, lin/ros	L, ros/lin	UL, ros/lin	L, ros/ros	UL, ros/ros
Bas_A	1	5	13.22	11.12	27.96	28.38	-	-	0.300	0.291	0.145	0.142	-	-	-	-
		5	15.37	14.85	27.76	27.92	-	-	0.323	0.333	0.147	0.150	-	-	-	-
		10	15.74	20.41	26.32	27.72	-	-	0.310	0.312	0.141	0.140	-	-	-	-
		20	16.43	17.19	27.53	29.91	-	-	0.277	0.272	0.154	0.137	-	-	-	-
Bas_B	1	5	12.96	18.09	30.41	31.86	34.12	36.33	-	-	0.177	0.198	-	-	0.198	0.226
		10	18.52	20.29	31.67	31.93	36.07	35.70	-	-	0.187	0.204	-	-	0.213	0.228
		20	20.14	21.96	31.95	32.70	35.91	36.44	-	-	0.189	0.206	-	-	0.212	0.229
		40	22.03	24.09	33.32	33.48	36.11	36.83	-	-	-	-	-	-	-	-
		60	23.13	26.12	34.41	35.09	36.17	37.98	-	-	-	-	-	-	-	-
		80	22.31	27.91	34.14	35.68	35.45	38.10	-	-	-	-	-	-	-	-
		40	22.81	23.57	32.98	33.31	35.27	35.37	-	-	-	-	-	-	-	-
		20	20.95	21.51	30.73	31.50	33.14	33.36	-	-	-	-	-	-	-	-
		10	18.44	18.93	29.25	30.38	31.80	32.22	-	-	-	-	-	-	-	-
	2	5	16.32	17.23	28.27	29.48	30.10	31.56	-	-	0.190	0.201	-	-	0.202	0.215
		10	17.95	17.83	29.56	29.55	31.30	31.66	-	-	0.191	0.202	-	-	0.202	0.216
		20	18.43	20.58	30.53	31.64	32.21	33.84	-	-	0.195	0.205	-	-	0.206	0.219
		40	20.72	23.65	32.79	33.41	34.11	35.32	-	-	0.202	0.210	-	-	0.210	0.222
		60	23.94	25.56	34.67	36.41	35.60	38.21	-	-	0.214	0.211	-	-	0.220	0.222
		80	24.85	28.25	34.81	37.63	35.31	38.97	-	-	0.225	0.214	-	-	0.228	0.221
		40	24.35	22.96	33.51	33.48	34.57	34.43	-	-	0.220	0.218	-	-	0.227	0.224
		20	20.53	21.09	31.21	32.13	32.33	32.86	-	-	0.209	0.220	-	-	0.216	0.225
		10	18.48	18.31	29.71	30.94	30.73	31.46	-	-	0.201	0.220	-	-	0.208	0.223
	3	5	15.08	16.32	28.17	29.30	28.48	29.69	-	-	0.188	0.204	-	-	0.19	0.206
		10	17.61	18.92	29.55	30.16	29.76	30.95	-	-	0.197	0.207	-	-	0.198	0.212
		20	18.76	20.96	30.76	31.52	30.90	32.48	-	-	0.202	0.211	-	-	0.203	0.217
NM_B	1	5	22.15	23.31	37.12	43.53	-	-	0.137	0.186	0.053	0.082	-	-	-	-
		5	27.08	28.73	40.62	45.98	-	-	0.176	0.204	0.072	0.092	-	-	-	-
		5	28.59	-	42.97	-	-	-	0.187	-	0.077	-	-	-	-	-
RS_A	1a	5	22.95	22.47	39.02	45.59	43.28	47.14	0.242	0.274	0.202	0.227	0.269	0.283	0.224	0.235
		5	19.88	24.94	41.66	45.35	44.11	45.80	0.251	0.268	0.215	0.233	0.266	0.271	0.227	0.235
		10	29.24	30.80	42.09	45.72	43.33	45.53	0.249	0.274	0.226	0.241	0.256	0.273	0.233	0.240
		20	27.37	34.22	43.70	47.54	45.01	47.63	0.264	0.280	0.228	0.242	0.272	0.280	0.235	0.243
	1b	20	25.09	29.70	45.20	44.62	38.90	42.41	-	-	0.280	0.256	-	-	0.240	0.218
		30	15.23	22.52	-	-	-	-	-	-	-	-	-	-	-	-
		40	19.71	21.17	-	-	-	-	-	-	-	-	-	-	-	-
SM_A	1	5	4.356	8.226	17.51	31.25	11.85	13.91	-	-	0.158	0.349	-	-	0.107	0.155
		20	8.813	11.49	26.33	47.53	13.46	16.64	-	-	0.306	0.661	-	-	0.156	0.231
		40	11.05	13.68	38.17	58.14	16.43	18.71	-	-	0.518	0.876	-	-	0.223	0.282
		60	13.52	16.35	51.34	62.82	19.06	21.19	-	-	0.744	0.902	-	-	0.276	0.304
		80	15.45	19.84	57.61	67.98	20.33	22.90	-	-	0.881	0.934	-	-	0.311	0.315

Table 5. Continued

Sample	Experiment #	P_c (MPa)	Young's modulus, E (GPa)						Poisson's ratio, v							
			L, LVDT	UL, LVDT	L, lin	UL, lin	L, ros	UL, ros	L, lin/lin	UL, lin/lin	L, lin/ros	UL, lin/ros	L, ros/lin	UL, ros/lin	L, ros/ros	UL, ros/ros
SM_A	1	100	16.13	25.28	74.63	81.39	20.63	26.18	-	-	1.153	0.990	-	-	0.319	0.319
WS_A	1	5	14.87	18.97	28.13	34.50	31.76	38.98	-	-	0.070	0.106	-	-	0.079	0.119
		10	21.51	25.20	35.56	39.71	37.17	42.35	-	-	0.107	0.133	-	-	0.112	0.142
		20	28.00	30.45	39.46	43.82	41.67	46.56	-	-	0.127	0.150	-	-	0.134	0.160
		40	32.27	36.18	44.84	48.89	47.60	51.80	-	-	0.143	0.165	-	-	0.152	0.175
		60	37.15	42.39	48.60	52.68	52.57	55.89	-	-	0.153	0.170	-	-	0.165	0.181
		80	36.82	45.49	49.27	57.15	54.83	62.07	-	-	0.157	0.167	-	-	0.175	0.182
		40	35.47	35.55	47.19	49.32	49.89	52.09	-	-	0.174	0.166	-	-	0.184	0.176
		20	28.69	30.08	42.28	44.55	44.16	46.77	-	-	0.168	0.156	-	-	0.175	0.163
		10	24.36	26.55	37.62	40.91	39.09	42.89	-	-	0.154	0.141	-	-	0.160	0.148
	2	5	24.56	31.26	37.82	41.85	41.59	45.59	-	-	0.191	0.193	-	-	0.210	0.211
		10	33.81	35.16	40.96	43.94	43.74	47.44	-	-	0.202	0.200	-	-	0.216	0.216
		20	35.26	37.85	43.18	45.55	46.55	49.34	-	-	0.205	0.200	-	-	0.221	0.216
		40	43.26	45.22	46.66	49.40	49.89	52.56	-	-	0.207	0.212	-	-	0.222	0.226
		60	46.89	46.49	48.30	50.83	53.80	55.93	-	-	0.193	0.199	-	-	0.215	0.219
		80	49.88	52.08	50.67	53.78	55.61	57.91	-	-	0.205	0.210	-	-	0.225	0.226
GS_A	1	5	23.84	25.60	-	-	36.91	39.19	-	-	-	-	-	-	0.185	0.192
		10	26.78	27.53	-	-	38.68	39.74	-	-	-	-	-	-	0.188	0.194
		20	25.41	27.59	-	-	38.44	39.50	-	-	-	-	-	-	0.191	0.195
		40	25.85	28.28	-	-	37.89	39.98	-	-	-	-	-	-	0.193	0.198
		60	26.74	31.30	-	-	39.17	40.99	-	-	-	-	-	-	0.197	0.200
		80	28.82	33.08	-	-	38.86	42.35	-	-	-	-	-	-	0.199	0.200
		40	27.25	29.08	-	-	38.66	39.41	-	-	-	-	-	-	0.198	0.199
		20	26.51	28.27	-	-	38.09	39.22	-	-	-	-	-	-	0.195	0.197
		10	26.61	26.76	-	-	37.34	38.47	-	-	-	-	-	-	0.193	0.194
	2	5	22.43	22.88	-	-	34.76	35.94	-	-	-	-	-	-	0.192	0.196
		5	22.54	22.50	-	-	35.34	35.60	-	-	-	-	-	-	0.192	0.196
GS_B	1	0	13.22	14.00	28.87	30.29	-	-	-	-	-	-	-	-	-	-
		5	20.23	18.96	31.48	32.97	-	-	-	-	-	-	-	-	-	-
		10	21.70	20.37	32.10	33.24	-	-	-	-	-	-	-	-	-	-
		20	22.50	21.73	34.95	34.66	-	-	-	-	-	-	-	-	-	-
		40	25.80	26.55	36.70	37.73	-	-	-	-	-	-	-	-	-	-
		60	26.66	28.97	36.71	39.86	-	-	-	-	-	-	-	-	-	-
		80	28.28	33.98	37.22	43.21	-	-	-	-	-	-	-	-	-	-
		40	26.81	28.09	37.62	39.28	-	-	-	-	-	-	-	-	-	-
		20	24.54	23.61	37.26	37.00	-	-	-	-	-	-	-	-	-	-
		10	22.59	21.14	34.70	34.32	-	-	-	-	-	-	-	-	-	-

= 5 MPa to 0.137 at P_c = 20 MPa. Young's modulus of gray sandstone determined by strain gauges increases from 30.29 GPa at P_c = 0 MPa, which is conducted before pressurization to 5 MPa, to 42.35-43.21 GPa at P_c = 80 MPa (Fig. 10a). Poisson's ratio of gray sandstone increases from 0.192 at P_c = 0 MPa to 0.200 at P_c = 80 MPa (Fig. 10b). An experiment on Nobeoka mélange (NM_A-1), which failed in pressurization of P_c from 5 to 10 MPa, exhibits strain-gauge-derived Young's modulus ranging from 40.39 to 45.98 GPa and Poisson's ratio of 0.068 to 0.204 at P_c = 5 MPa (Fig. 11). Young's modulus of red shale derived from strain gauges increases from 45.35-47.14 GPa at P_c = 5 MPa to 47.54-47.63 GPa at P_c = 20 MPa in experiment RS_A-1a (Fig. 12a). Poisson's ratio of red shale ranges from 0.227-0.283 at P_c = 5 MPa to 0.242-0.280 at P_c = 20 MPa (Fig. 12b), although the greatest value of 0.283 is observed at 5 MPa (RS_A-1a ros/lin). Experiment RS_A-1 was conducted over two days due to time constrains. After the load/unload tests were run at P_c = 5, 10, and 20 MPa (called RS_A-1a), confining pressure was depressurized and resumed to pressurize to 20 MPa in the next day and the load/unload tests were conducted at P_c = 20, 30, and 40 MPa (called RS_A-1b). The strain gauge data were only available at P_c = 20MPa in the experiment RS_A-1b. Experiment RS_A-1b demonstrated lower Young's modulus and Poisson's ratio values than those of Experiment RS_A-a at Pc = 20 MPa, ranging 42.41-44.62 GPa and 0.218-0.256, respectively, (Fig. 12a). Young's modulus and Poisson's ratio of Shimanto mélange increases from 13.91-31.25 GPa and 0.155-0.349 at P_c = 5 MPa to 26.18-81.39 GPa and 0.319-0.990 at P_c = 100 MPa, respectively (Fig. 13). Young's modulus and Poisson's ratio of Shimanto white sandstone increases from 34.50-45.59 GPa and 0.106-0.211at P_c = 5 MPa to 53.78-62.07 GPa and 0.167-0.226 at P_c = 80 MPa (Fig. 14).

38

In addition to strain gages attached to specimens, Young's modulus were determined also from the axial displacement measured by LVDT located outside the pressure vessel. For all the tested samples, Young's modulus derived from LVDT generally increases with P_c, as observed in strain gage data, and are lower than that derived from strain gauges (Figure 7-12; Table 5). LVDT-derived Young's modulus of basalt increases from 11.12-18.09 GPa at P_c = 5 MPa to 22.31-28.25 GPa at P_c = 80 MPa (Fig. 9a). LVDT-derived Young's modulus of gray sandstone increases from 14.00 GPa at P_c = 0 MPa to 33.08-33.98 GPa at P_c = 80 MPa (Fig. 10a). An experiment on Nobeoka mélange (NM_A-1) over two iterations at P_c = 5 MPa exhibits LVDT-derived Young's modulus ranging from 22.15 to 28.73 GPa at P_c = 5 MPa (Fig. 11a). LVDT-derived Young's modulus of red shale increases from 22.47-24.94 GPa at P_c = 5 MPa to 34.22 GPa at P_c = 20 MPa in experiment RS_A-1a (Fig. 12a). Experiment RS_A-1b demonstrated lower LVDT-derived Young's modulus values of 29.70 GPa at Pc = 20 MPa to 21.17 GPa at Pc = 40 MPa (Fig. 12a). During pressurization from 20 to 30 MPa, the specimen deformed, causing the decrease in Young's modulus. LVDT-derived Young's modulus of Shimanto mélange increases from 8.226 GPa at P_c = 5 MPa to 25.28 GPa at P_c = 100 MPa (Fig. 13a). LVDT-derived Young's modulus of white sandstone increases from 18.97-31.26 GPa at P_c = 5 MPa to 45.49-52.08 GPa at P_c = 80 MPa (Fig. 14a). The strain gauge values (regardless of gauge type are systematically greater than the LVDT values by 1-80%. The difference between these values decreases with increasing confining pressure (Figs. 15-16, Table 5). The difference greater than 50% is observed at confining pressure of 5 MPa or in the experiment SM_A-1. In the experiment SM_A-1, both linear and tee rosette strain gauge data show a different trend in comparison of

Young's modulus derived from strain gauges and LVDT (Figure 15). The linear strain

gauge data results in much greater Young's modulus value than LVDT-derived value

whereas the rosette strain gauge data results in slightly higher value.
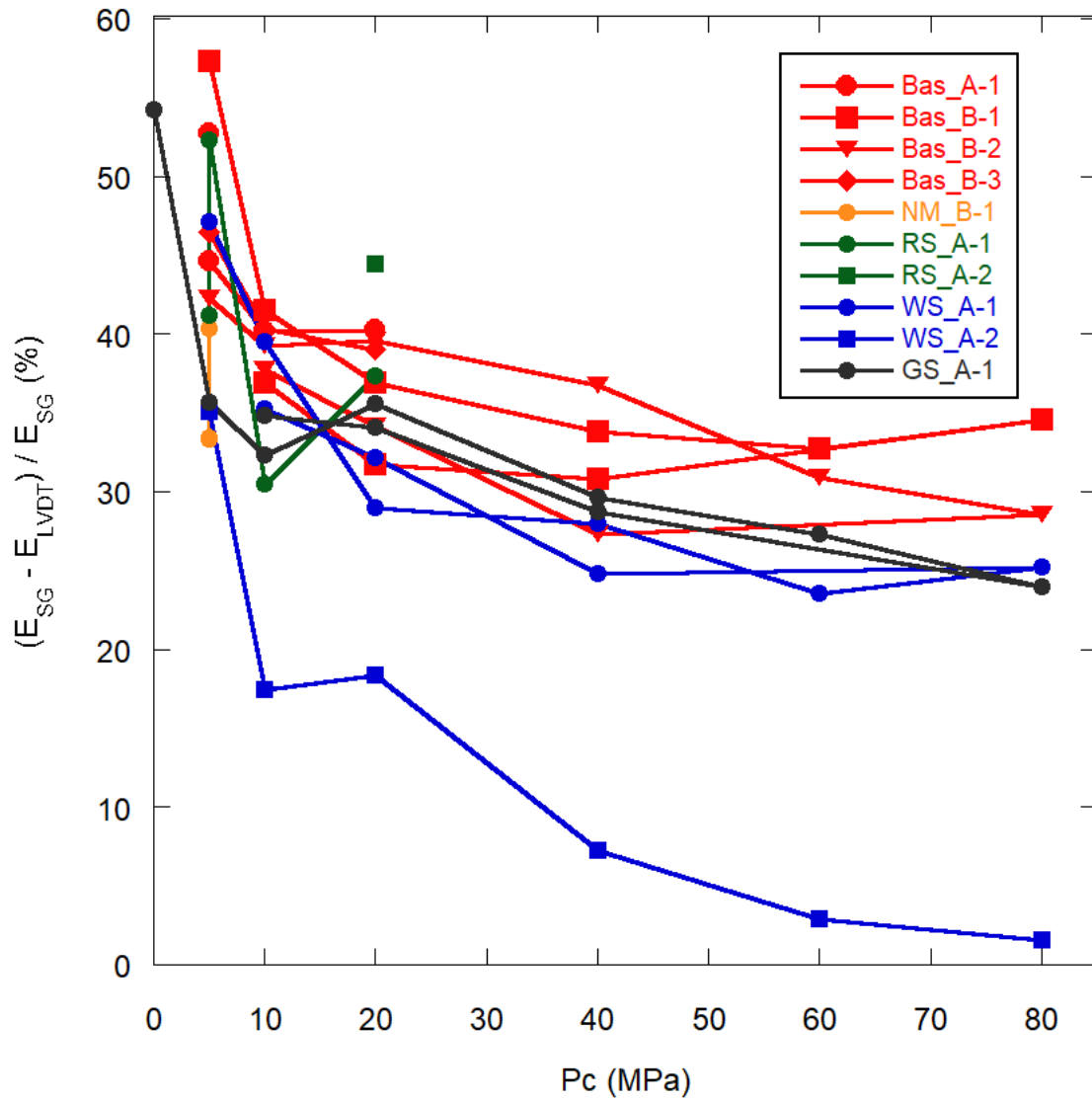
Fig. 15. Comparison of Young's modulus between LVDT measured values and linear strain gauge values. The y-axis represents the percentage difference in Young's modulus between the strain gauge and LVDT data relative to the strain gauge data.

Several relationships and correlations were evidenced in the Young's modulus data. First, the Young's modulus values determined by tee rosette strain gauge are 1-20% greater than those determined by the linear strain gauge with the exception of the Shimanto mélange sample (Table 5, Figs. 9a-14a). Second, the values calculated during the unloading portion of the experiment are generally greater than the loading curve values (Table 5). Third, the values calculated during depressurization are generally greater than the pressurization values of the same P_c (10, 20, and 40 MPa).
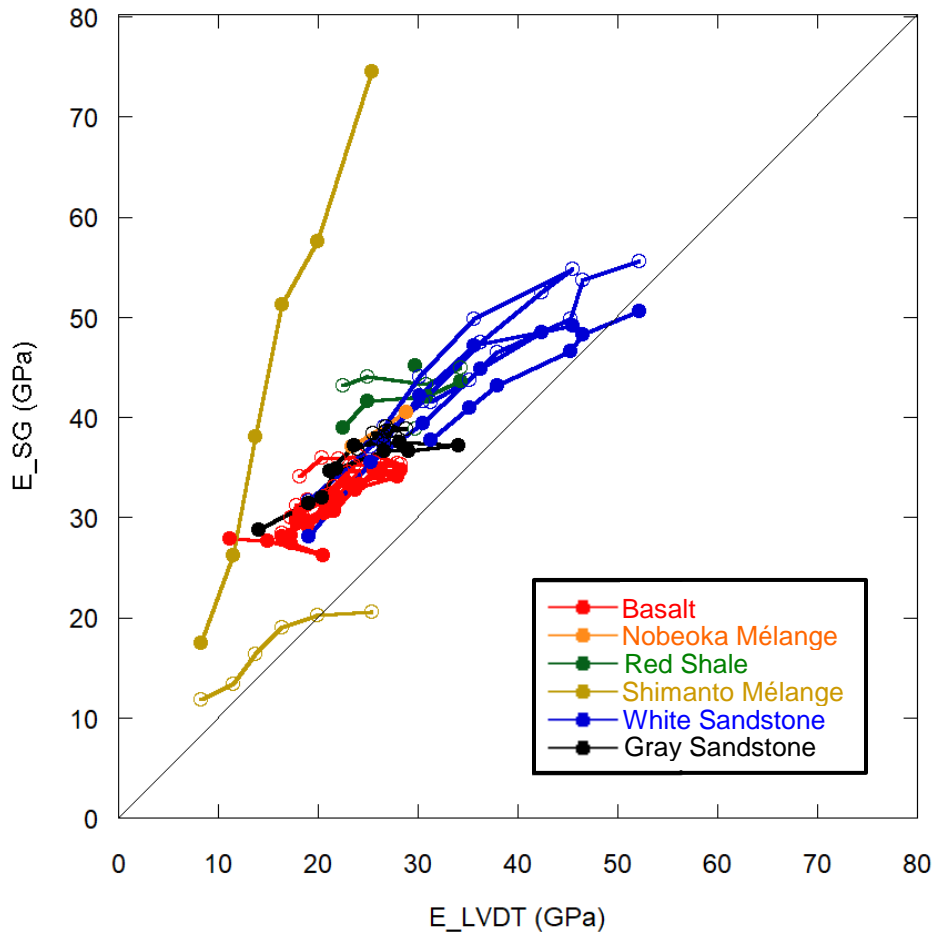
Fig. 16. Comparison of Young's modulus between strain gauge and LVDT values. Open and closed symbols represent rosette and linear strain gauge values, respectively.

41
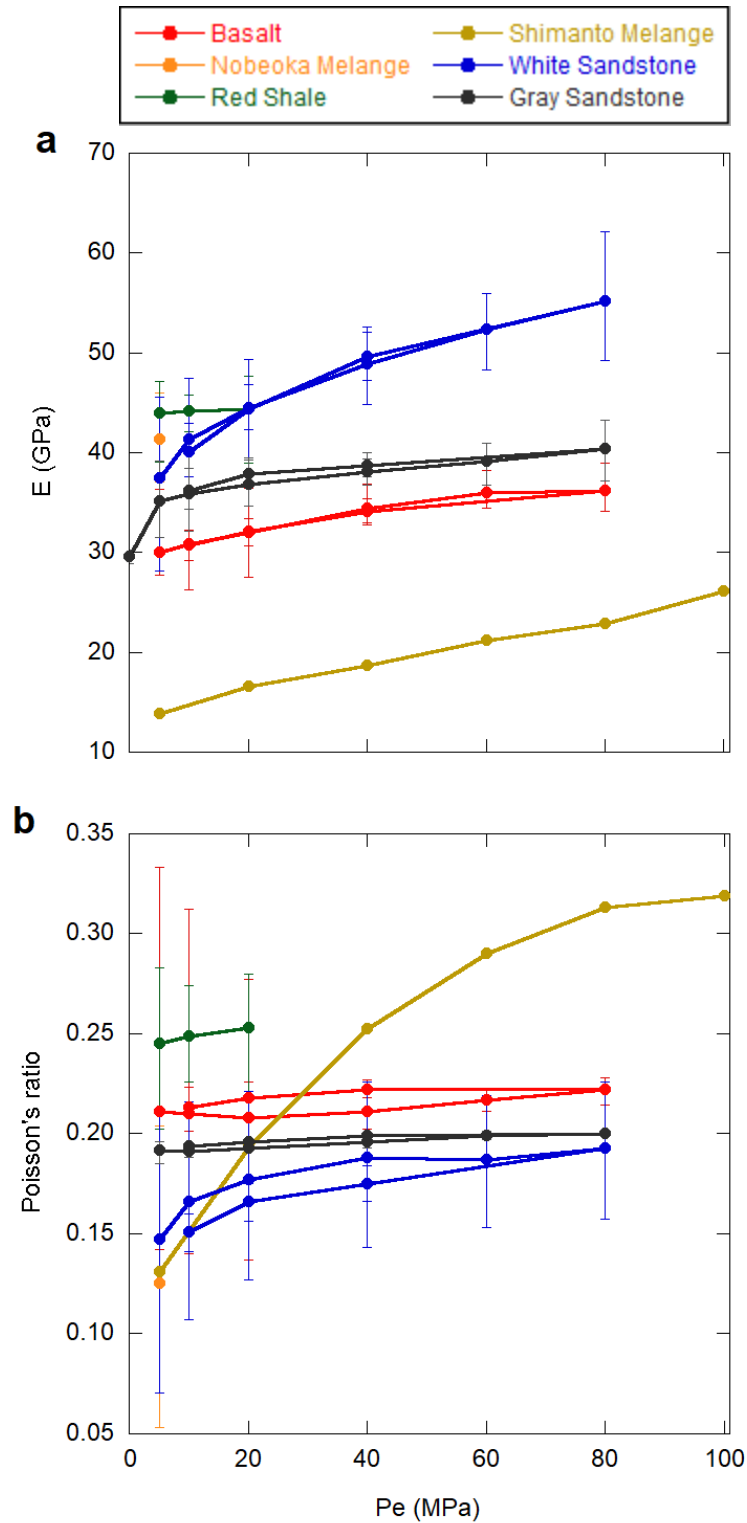
Fig. 17. Summary of (a) Young's modulus and (b) Poisson's ratio for all experiments. Data points are the averages taken across all unloading strain gauge measurements. Error bars represent maximum and minimum values. Shimanto mélange linear Young's modulus and linear/rosette Poisson's ratio not included because the values are untrustworthy.

For Poisson's ratio, various relationships were seen similar to the Young's modulus (Table 5, Figs. 9b-14b). First, the Poisson's ratio values determined from the axial and radial strains of a tee rosette strain gauge are greater than those calculated from the axial strain of a linear strain gauge and radial strain of a tee rosette strain gauge. Second, the values calculated during the unloading portion of the experiment are generally greater than the loading curve values (Table 5).

Comparing different lithologies, the Shimanto mélange exhibits the greatest pressure dependence of Young's modulus and Poisson's ratio and the white sandstone shows the second greatest dependence (Fig. 17). The basalt, on the other hand, demonstrates the smallest pressure dependence (Fig. 17). Based on the contrasting pressure dependence of Young's modulus, the white sandstone and basalt were chosen for deformation and acoustic velocity experiments. Shimanto mélange was not chosen due to the limited amount of source material, difficulty of sample preparation, and questionable result values. The experiment of the Shimanto mélange (SM_A-1) show confounding results in terms of both Young's modulus and Poisson's ratio. As mentioned above, the difference between strain-gauge-derived Young's modulus and LVDT-derived Young's modulus are exceptional (Fig. 16) and the Poisson's ratio derived from axial strain of a linear strain gauge and radial strain of a rosette strain gauge results in exceptionally high values, which is greater than the values between 0 and 0.5 expected for most solids and especially rocks (Fig. 13). Therefore, the results of linear strain gages are not reliable. Still, the Young's modulus determined by rosette strain gage was similar to that determined by LVDT as seen in other lithology samples, and the Poisson's ratio values determined by rosette strain gage are reasonable. Although the exact cause of the error

43

was unknown, possible causes include but not limited to: improper adhesion of the strain gauge to the sample, poor wiring connection, pinched wires, and poor quality strain gauge.

Utilizing the calculated Young's modulus and Poisson's ratio, I calculated other elastic moduli (Bulk modulus – K, Lamé constant – λ, Shear modulus – G, and P-wave modulus – M). Additionally, P-wave and S-wave velocities were calculated given the elastic moduli and measured density (Table 6). The Young's modulus values determined by the linear strain gauge from the unloading curve were used, except for GS_A sample. In both experiments on sample GS_A, Young's modulus determined by the tee rosette strain gauge were used for both experiments (GS_A-1; GS_A-2) because the linear strain gauge was not functional during the experiment. For GS_B-1, no elastic moduli were calculated because Poisson's ratio is not available due to malfunction of the tee rosette strain gauge. Overall, all of the calculated moduli increase with increasing confining pressure.

Table 6. Elastic moduli and acoustic velocity calculations from static measured data.
[**E** is the Young's modulus, **K** is the Bulk modulus, **v** is the Poisson's ratio, **λ** is the Lame's constant, **G** is the Shear modulus, **M** is the P-wave modulus, **α** is the P-wave velocity, and **β** is the S-wave velocity]

Sample	Experiment #	P_c (MPa)	E (GPa)	v	K (GPa)	λ (GPa)	G (GPa)	M (GPa)	α (km/s)	β (km/s)
Bas_A	1	5	28.38	0.142	13.21	4.93	12.42	29.78	-	-
		5	27.92	0.150	13.30	5.20	12.14	29.48	-	-
		10	27.72	0.140	12.84	4.73	12.16	29.05	-	-
		20	29.91	0.137	13.73	4.96	13.15	31.27	-	-
Bas_B	1	5	31.86	0.198	17.58	8.72	13.30	35.31	3.721	2.284
		10	31.93	0.204	17.98	9.14	13.26	35.66	3.740	2.280
		20	32.70	0.206	18.54	9.50	13.56	36.62	3.789	2.306
		40	33.48	-	-	-	-	-	-	-
		60	35.09	-	-	-	-	-	-	-
		80	35.68	-	-	-	-	-	-	-
		40	33.31	-	-	-	-	-	-	-
		20	31.50	-	-	-	-	-	-	-
		10	30.38	-	-	-	-	-	-	-
	2	5	29.48	0.201	16.43	8.25	12.27	32.80	3.587	2.194
		10	29.55	0.202	16.53	8.33	12.29	32.92	3.593	2.196
		20	31.64	0.205	17.87	9.12	13.13	35.38	3.725	2.269

Table 6. Continued.

[**E** is the Young's modulus, **K** is the Bulk modulus, **ν** is the Poisson's ratio, **λ** is the Lame's constant, **G** is the Shear modulus, **M** is the P-wave modulus, **α** is the P-wave velocity, and **β** is the S-wave velocity]

Sample	Experiment #	P_c (MPa)	E (GPa)	ν	K (GPa)	λ (GPa)	G (GPa)	M (GPa)	α (km/s)	β (km/s)
Bas_B	2	40	33.41	0.210	19.20	10.00	13.80	37.60	3.840	2.327
		60	36.41	0.211	21.01	10.98	15.03	41.05	4.012	2.428
		80	37.63	0.214	21.93	11.60	15.50	42.60	4.087	2.465
		40	33.48	0.218	19.78	10.62	13.74	38.11	3.866	2.321
		20	32.13	0.220	19.13	10.35	13.17	36.68	3.793	2.272
		10	30.94	0.220	18.42	9.96	12.68	35.33	3.722	2.230
	3	5	29.30	0.204	16.50	8.39	12.17	32.72	3.582	2.184
		10	30.16	0.207	17.16	8.83	12.50	33.82	3.642	2.214
		20	31.52	0.211	18.18	9.50	13.02	35.53	3.733	2.259
NM_B	1	5	40.39	0.068	15.58	2.98	18.91	40.80	3.873	2.637
		5	45.98	0.092	18.78	4.75	21.05	46.85	4.150	2.782
		5	-	-	-	-	-	-	-	-
RS_A	1	5	45.59	0.227	27.83	15.45	18.58	52.60	4.430	2.633
		5	45.35	0.233	28.31	16.05	18.39	52.83	4.440	2.620
		10	45.72	0.241	29.42	17.14	18.42	53.99	4.488	2.622
		20	47.54	0.242	30.71	17.95	19.14	56.23	4.580	2.672
	2	20	44.62	0.256	30.48	18.64	17.76	54.17	4.496	2.575
		30	-	-	-	-	-	-	-	-
		40	-	-	-	-	-	-	-	-
SM_A	1	5	31.25	0.349	34.49	26.77	11.58	49.93	-	-
		20	47.53	0.661	-49.20	-58.74	14.31	-30.13	-	-
		40	58.14	0.876	-25.77	-36.10	15.50	-5.11	-	-
		60	62.82	0.902	-26.04	-37.05	16.51	-4.03	-	-
		80	67.98	0.934	-26.11	-37.82	17.58	-2.67	-	-
		100	81.39	0.990	-27.68	-41.32	20.45	-0.42	-	-
WS_A	1	5	34.50	0.106	14.60	4.20	15.60	35.39	3.711	2.464
		10	39.71	0.133	18.04	6.35	17.53	41.40	4.014	2.611
		20	43.82	0.150	20.87	8.17	19.05	46.27	4.243	2.723
		40	48.89	0.165	24.32	10.33	20.98	52.30	4.511	2.857
		60	52.68	0.170	26.60	11.60	22.51	56.62	4.694	2.960
		80	57.15	0.167	28.60	12.28	24.48	61.25	4.882	3.087
		40	49.32	0.166	24.61	10.51	21.15	52.81	4.533	2.869
		20	44.55	0.156	21.58	8.74	19.27	47.27	4.289	2.738
		10	40.91	0.141	18.99	7.04	17.93	42.89	4.085	2.641
	2	5	41.85	0.193	22.72	11.03	17.54	46.10	4.235	2.612
WS_A	2	10	43.94	0.200	24.41	12.21	18.31	48.83	4.359	2.669
		20	45.55	0.200	25.31	12.65	18.98	50.61	4.438	2.718
		40	49.40	0.212	28.59	15.00	20.38	55.76	4.658	2.816
		60	50.83	0.199	28.14	14.01	21.19	56.40	4.685	2.872
		80	53.78	0.210	30.91	16.09	22.22	60.54	4.853	2.941
GS_A	1	5	39.19	0.192	21.21	10.25	16.44	43.13	4.065	2.510
		10	39.74	0.194	21.64	10.55	16.64	43.83	4.098	2.525
		20	39.50	0.195	21.59	10.57	16.53	43.62	4.088	2.516
		40	39.98	0.198	22.06	10.94	16.68	44.31	4.120	2.528
		60	40.99	0.200	22.77	11.38	17.08	45.54	4.177	2.558
		80	42.35	0.200	23.53	11.76	17.65	47.06	4.246	2.600
		40	39.41	0.199	21.82	10.87	16.44	43.74	4.094	2.509
		20	39.22	0.197	21.57	10.65	16.38	43.42	4.079	2.505
		10	38.47	0.194	20.96	10.21	16.11	42.44	4.032	2.485
	2	5	35.94	0.196	19.70	9.69	15.02	39.73	3.902	2.399
		5	35.60	0.196	19.51	9.59	14.88	39.36	3.883	2.388
GS_B*	1	-	-	-	-	-	-	-	-	-

* No Poisson's ratio was recorded for sample GS_B, so no elastic moduli and acoustic velocity values were calculated.

4.2. Triaxial Deformation Experiments

As discussed in the previous section, deformation experiments were conducted on the basalt and white sandstone samples only because these samples demonstrate the least and greatest pressure dependence, respectively, of both Young's modulus and Poisson's ratio (Fig. 17). The basalt and white sandstone exhibit different deformation characteristics in terms of mode of failure, peak strength, and fracture angle (Fig. 18, Table 7). The basalt samples demonstrated brittle failure at confining pressure of 5 and 10 MPa, and ductile failure at 20 MPa. The white sandstone samples demonstrated brittle failure for all confining pressures ranging between 5 and 80 MPa.

Table 7. Summary of triaxial deformation experiment results on basalt (Bas) and white sandstone (WS). Yield and peak strength recorded as differential stresses. Young's modulus was determined from LVDT axial displacement data.

Sample	P_c (MPa)	Yield stress (MPa)	Peak strength (MPa)	Young's modulus (GPa)	Mode of failure	Fracture angle (°)
Bas_D	5	52.64	71.82	10.48	Brittle	28.8
Bas_F	10	60.17	89.91	13.23	Brittle	31.5
Bas_E	20	57.59	102.5*	16.24	Ductile	-
WS_G	5	234.3	253.0	30.73	Brittle	17.9
WS_J	10	271.4	301.2	32.40	Brittle	28.8
WS_B	20	292.2	335.2	37.10	Brittle	34.8
WS_F	40	312.1	417.4	40.70	Brittle	36.2
WS_A	80	332.5	509.6	49.50	Brittle	41.1
				Lin: 50.55		
				Ros: 51.23		

* Ultimate strength of basalt at 2.8% strain.

Yield stress is defined and determined as the differential stress where the stress-strain curve deviates from linear behavior. Yield stress increases with confining pressure within the brittle regime. For basalt, the yield stress increases with confining pressure from 52.64 MPa at P_c = 5 MPa to 60.17 MPa at P_c = 10 MPa in brittle regime but slightly decreases to 57.59 MPa at P_c = 20 MPa. For white sandstone, yield stress increases with

confining pressure systematically from 234.3 MPa at P_c = 5 MPa to 332.5 MPa at P_c = 80

MPa. Peak strength increases with confining pressure; the peak strength of the white

sandstone (253.0 MPa at P_c = 5 MPa and 301.2 MPa at P_c = 10 MPa) is more than three

times greater than that of the basalt (71.82 MPa at P_c = 5 MPa and 89.91 MPa at P_c = 10

MPa) at the same confining pressure (Fig. 18, Table 7). Fracture angle, which was

measured from the fracture plane relative to the cylindrical axis, decreases with confining

pressure. Basalt shows lower facture angles than white sandstone for each confining

pressure. The strain at which the basalt samples fractured displays no correlation with

confining pressure, while the strain at which the white sandstone fractured appears to

increase with confining pressure (Table 7).

It should be noted that the triaxial compression experiment on white sandstone at

80 MPa was conducted right after the triaxial loading/unloading for elastic moduli

measurements at pressures ranging from 5 to 80 MPa confining pressure (5-10-20-40-60-

80 MPa). After the 80 MPa loading/unloading iteration, the specimen was deformed.

Thus this experiment also records strain gauges data (Fig. 18c). From the stress-strain

curves (Fig. 18a), the deformation behavior of the white sandstone at P_c = 80 MPa is

different from the rest. This difference is possibly due to the presence of the strain gauge.

The adhesive used to attach the strain gauge may strengthen the specimen and delay the

fracturing till a higher strain. The LVDT-derived Young's modulus is greater than the

linear and tee rosette Young's moduli by 0.99 and 0.62 GPa, respectively.
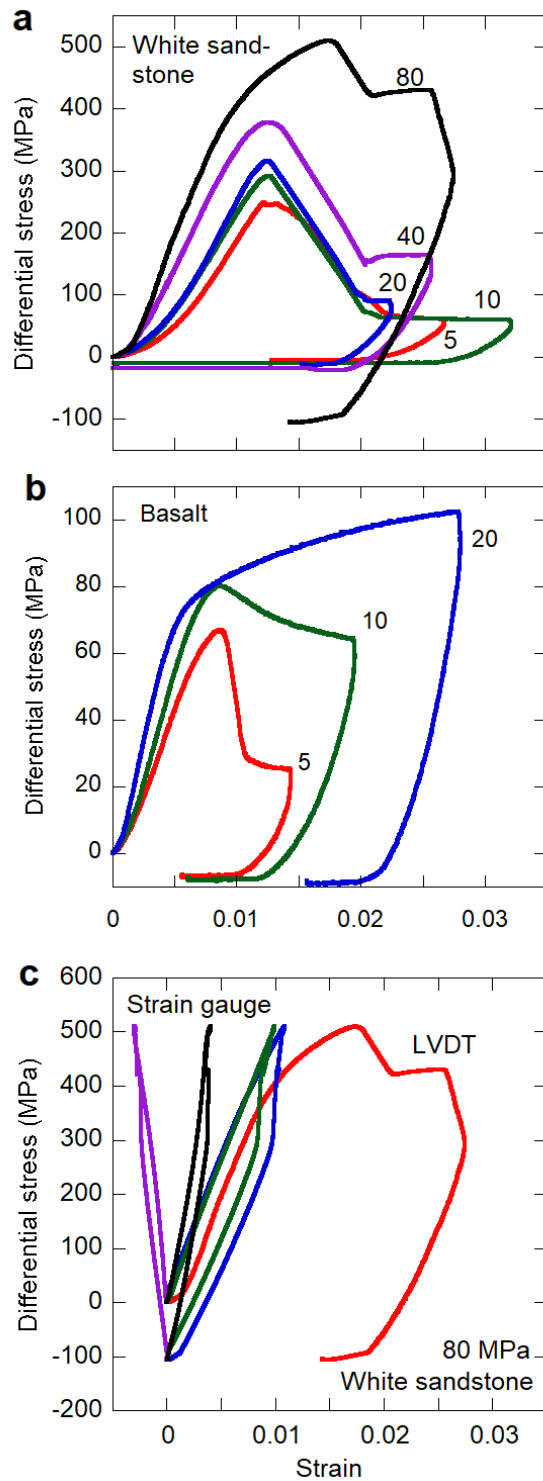
Fig. 18. Results of triaxial deformation experiment on (a) white sandstone and (b) basalt. (c) Results of white sandstone deformed at 80 MPa. LVDT-derived axial strain (red) and axial strain of a linear strain gauge (blue), axial strain of a rosette strain gauge (green), radial strain of a rosette strain gauge (purple), and volumetric strain (black) calculated from the axial (green) and radial (purple) strains of a rosette strain gauge are presented.

48

4.3. Acoustic Velocity Measurements

Acoustic velocity measurements were conducted on only the basalt and white sandstone samples because these samples demonstrate the least and greatest pressure dependence of Young's modulus and Poisson's ratio (Fig. 17), respectively. The displacements, travel times, and acoustic velocities were determined from the acoustic experiments (sandstone – Table 8, basalt – Table 9). Displacements and velocities generally increase with confining pressure, while travel times typically decrease with increasing confining pressures. During pressurization, sandstone has higher average velocities than basalt (except at 5 MPa) (Fig. 19). During depressurization, basalt has a higher velocity than the sandstone (except at 60 MPa, Fig. 19). In both experiments, a small jacket leak occurred.

Table 8. Acoustic velocity test results for sandstone. Initial sample length is 24.12 mm.

Pc (MPa)	Displacement (mm)	Δt measured (µs)	Velocity (km/s)
5	0.0050	14.2 ± 0.4	2.44
10	0.0055	13.8 ± 0.2	2.50
20	0.0062	13.6 ± 0.1	2.63
40	0.0024	13.5 ± 0.2	2.73
60	0.0100	13.3 ± 0.3	2.65
80	0.0220	13.2 ± 0.4	2.64
60	0.0120	13.2 ± 0.4	3.34
40	0.0090	14.0 ± 0.1	2.49
20	0.0010	13.8 ± 0.2	2.78
10	0.0030	13.9 ± 0.3	2.54

Table 9. Acoustic velocity test results for basalt. Initial sample length is 25.38 mm.

Pc (MPa)	Displacement (mm)	Δt measured (µs)	Velocity (km/s)
5	-0.0076	14.0 ± 0.3	2.60
10	-0.0077	15.0 ± 0.8	2.36
20	-0.0035	14.2 ± 0.6	2.61
40	0.0028	14.1 ± 0.4	2.70
60	0.0109	13.9 ± 0.2	2.62
80	0.0151	13.8 ± 0.1	2.60
60	-0.0108	13.8 ± 0.1	3.23
40	-0.0216	13.6 ± 0.4	2.73
20	-0.0122	13.6 ± 0.4	3.00
10	-0.0143	13.8 ± 0.2	2.68
5	-0.0148	14.1 ± 0.0	2.58
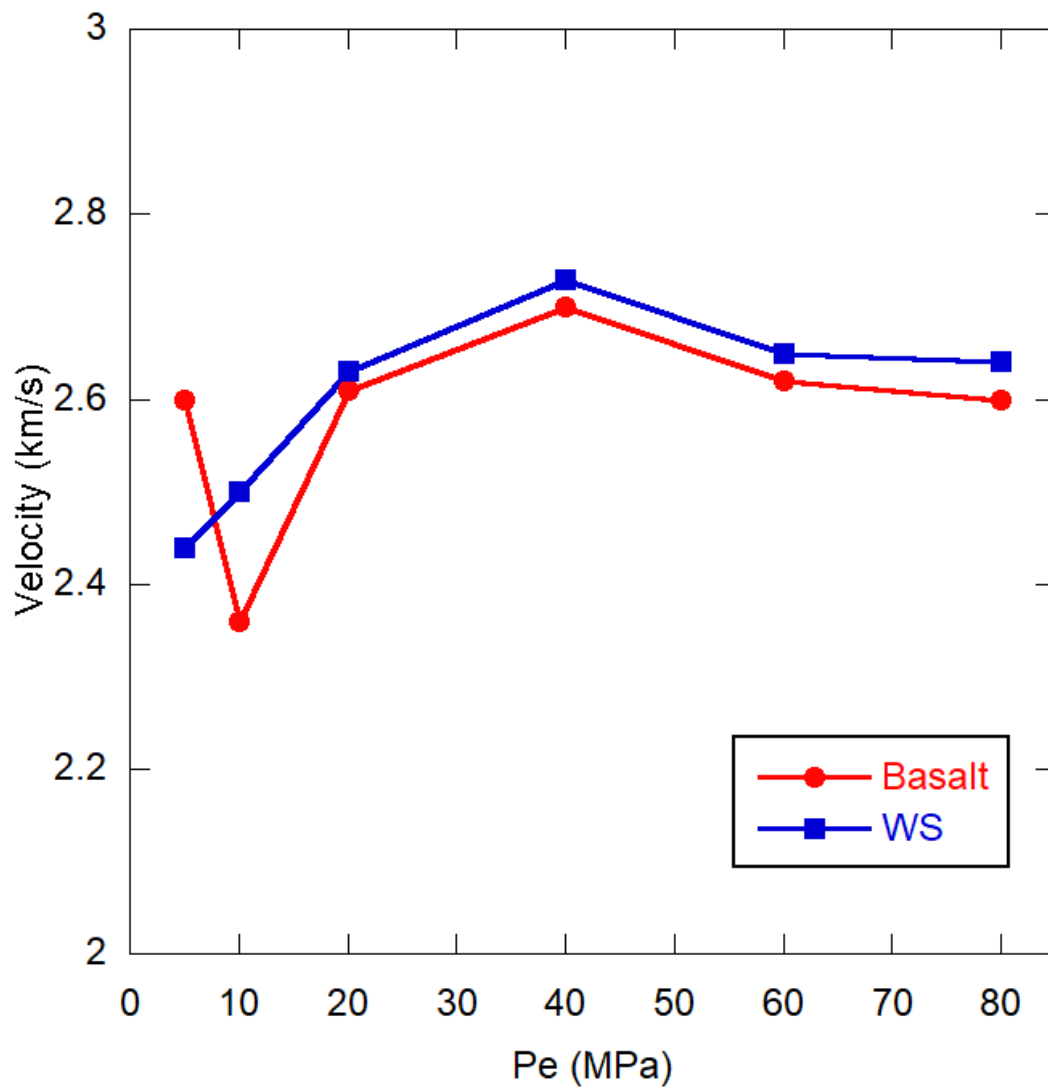
Fig. 19. Measured acoustic velocities for basalt and white sandstone (red and blue, respectively).

5. DISCUSSION

5.1. Yield Strength and Failure Criterion

Triaxial deformation experiments on white sandstone and basalt reveal that white sandstone deforms brittle at all tested confining pressure ranging from 5 to 80 MPa, whereas basalt deforms brittle at 5 and 10 MPa and ductile at 20 MPa. Both white sandstone and basalt exhibit in brittle regime an increase in yield and peak strengths with confining pressure (Table 7, Fig. 20). Differential stress at yield and peak of white sandstone increases from 234.3 MPa and 253.0 MPa at Pc = 5 MPa to 332.5 MPa and 509.6 MPa at Pc = 80 MPa, respectively. From the experiment results, failure criteria for white sandstone and basalt was constructed in σ_1'-σ_3' space, where σ_1' and σ_3' are effective maximum and minimum principal stresses, respectively (Fig. 20). Effective stress or pressure is used because rock strength is dependent on effective stress rather than total stress. In this study, pore pressure was 0 and thus effective confining pressure (P_e), σ_1', and σ_3' are equal to confining pressure (P_c), σ_1, and σ_3. Given the limited data set on the basalt, the failure criteria forms a perfectly straight line expressed as $\sigma_1' = 4.62\sigma_3' + 53.7$ or $\tau = 0.842\sigma_n + 12.5$. For the white sandstone, on the other hand, the best-fit linear relation is expressed as $\sigma_1' = 4.26\sigma_3' + 262$ or $\tau = 0.790\sigma_n + 63.7$ (R^2=0.978) and second-order polynomial fit is $\sigma_1' = -0.0297\ (\sigma_3')^2 +6.82\sigma_3' + 233$ (R^2=0.998).

Kitajima et al. (2017) reported results of triaxial deformation experiments on phyllite and mélange, which are composed of hanging wall and footwall of the Nobeoka thrust, respectively. Phyllite and mélange exhibit pressure dependence of yield and peak

strength as seen in white sandstone and basalt. Phyllite shows yield and peak strength (in differential stress) ranging from 71-179 MPa and 94-415 MPa, respectively.
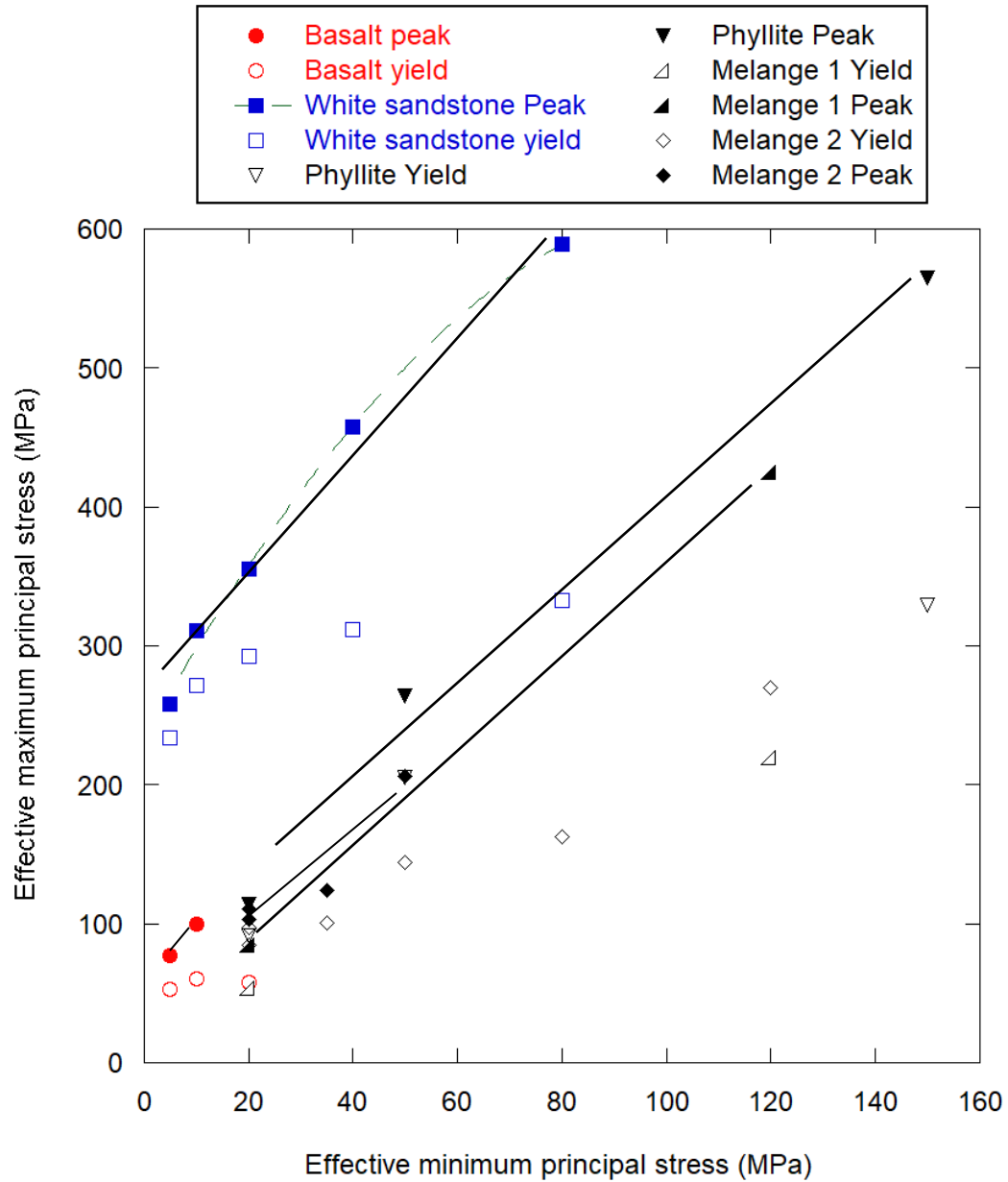
Fig. 20. Yield (open) and peak (solid) strengths of white sandstone (blue) and basalt (red) in σ_1'- σ_3' space. Only the data in brittle deformation regime are shown. Strengths for phyllite of the hanging wall and mélange of the footwall of the Nobeoka thrust (Kitajima et al. 2017) are also shown for comparison (black). Solid lines represent the best-fit linear relation for peak strengths. The dashed curve represents the best-fit second order polynomial relation for the peak strength of white sandstone.

52

at P_e = 20-150 MPa, whereas mélange shows yield and peak strength ranging from 34-150 MPa and 65-305 MPa, respectively, at P_e = 20-120 MPa. Comparing yield and peak stresses at similar effective pressure, the values of white sandstone are several times greater than both the phyllite and mélange, and the yield and peak stress values of basalt are similar to or slightly higher than the phyllite and mélange. At effective pressure of 20 MPa, phyllite has a yield and peak strength of 71 MPa and 94 MPa, respectively; two mélange samples exhibit yield stresses of 34 MPa and 65 MPa and peak stresses of 65 MPa and 91 MPa. Comparatively, yield and peak stresses of white sandstone at effective pressure of 20 MPa are 292.2 MPa and 335.2 MPa, respectively. Yield stress of basalt is 57.59 MPa at effective pressure of 20 MPa, which is smaller than the yield stress of the phyllite and one of the mélange (Mélange 2) but greater than the other mélange sample (Mélange 1). Peak stress of basalt is not compared because the basalt experienced strain hardening at P_e = 20 MPa, as opposed to the brittle deformation experienced by the phyllite and mélange.

Comparing my best-fit linear relations for peak stress (basalt: $\sigma_1' = 4.62\sigma_3' + 53.7$; white sandstone: $\sigma_1' = 4.26\sigma_3' + 262$) to those for phyllites ($\sigma_1' = 3.35\sigma_3' + 68.7$) and mélanges ($\sigma_1' = 3.32\sigma_3' + 29.4$) in Kitajima et al. (2017), the internal friction for my relations are higher for both basalt and white sandstone. However, the unconfined compressive strength (y-intercept of σ_1'-σ_3' relation) for basalt is smaller than that for phyllite but greater than that for mélange, whereas the white sandstone has significantly greater unconfined compressive strength than the phyllite and mélange.

Comparing my best-fit linear relations for yield stress (basalt: $\sigma_1' = 1.25\sigma_3' +$ 53.9, white sandstone: $\sigma_1' = 2.10\sigma_3' + 254$) to those for phyllites ($\sigma_1' = 1.68\sigma_3' + 85.0$) and mélanges ($\sigma_1' = 1.63\sigma_3' + 46.9$) calculated from reported values in Kitajima et al. (2017), the slope for my relations are higher for white sandstone but lower for basalt.

Differences in strengths are most likely due to the differences in porosity and lithology, although testing methods of Kitajima et al. (2017) are different from this study. The phyllites and mélange in Kitajima et al. (2017) have porosities of 1.40-1.61% and 1.67-1.98%, which are lower than both the white sandstone (2.6%) and basalt (11.0%). Phyllite and mélange have been metamorphosed, altering and strengthening the rocks. Comparing the basalt to Kitajima et al. (2017), the strength increases with decreasing porosity. White sandstone differs from this trend because the porosity is similar to the phyllite and mélange, but the strength of the white sandstone is significantly greater than the phyllite and mélange. Experimental conditions were also different in saturation, displacement rate, temperature, and jacketing. Kitajima et al. (2017) utilized pore pressure and had saturated samples whereas dry samples were used in experiments of this study. In general, dry samples have greater strength than wet samples. When pore pressure is applied and the sample deforms at strain rates greater than a critical strain rate, the strength of the rocks increases with strain rate because the pore pressure within the sample becomes lower than the value measured outside of the sample due to dilatancy of the sample (i.e., dilatancy hardening; Brace & Martin, 1968). Phyllite and mélange were deformed at $1-2\times10^{-5}$ s^{-1}, which is in the same order of magnitude to that used in this study ($\sim1.0\times10^{-5}$ s^{-1}). Additionally, all experiments of Kitajima et al. (2017) were conducted at 250˚C, whereas this study conducted all experiments at room temperature.

Heating the sample may decrease the strength of the specimen. Kitajima et al. (2017) used a 0.2-mm-thick copper jacket surrounding the sample to isolate the specimen from the confining fluid at elevated temperature, whereas this study utilized double layers of jacket made of polyolefin, which is operational at temperature lower than 135˚C. The experiment on mélange at room temperature results in a greater peak strength by ~10% compared to that at 250˚C (Kitajima, unpublished data). Thus, effects of difference in experimental method (pore pressure and temperature) on the mechanical behaviors including strength and mode of failure are likely minimal.

5.2. Elastic Moduli and Fracture Strength Comparison

The correlation between Young's modulus and the Poisson's ratio were compared for all lithologies (Fig. 21). Two trends are observed in the data. (1) There is a positive correlation between Young's modulus and Poisson's ratio for each lithology. However, the rate at which Young's modulus increases changes. At lower pressures, Young's modulus monotonically increases with Poisson's ratio. At higher pressures, Young's modulus increases drastically with little change in Poisson's ratio. (2) Comparing lithologies, lithologies with lower Poisson's ratio generally have higher Young's modulus values (Fig. 21). For example, white sandstone displays a lower Poisson's ratio than basalt, but the Young's modulus of white sandstone is higher than that of basalt.

LVDT-derived Young's modulus values from triaxial deformation experiments differ from the Young's modulus values from triaxial load/unload experiments (Fig. 22; Tables 5 and 7). For triaxial deformation experiments, the Young's modulus was determined using the stress-strain curves between 35% of the yield point and the yield point. Comparing values for basalt at Pc = 5, 10, and 20 MPa, Young's modulus
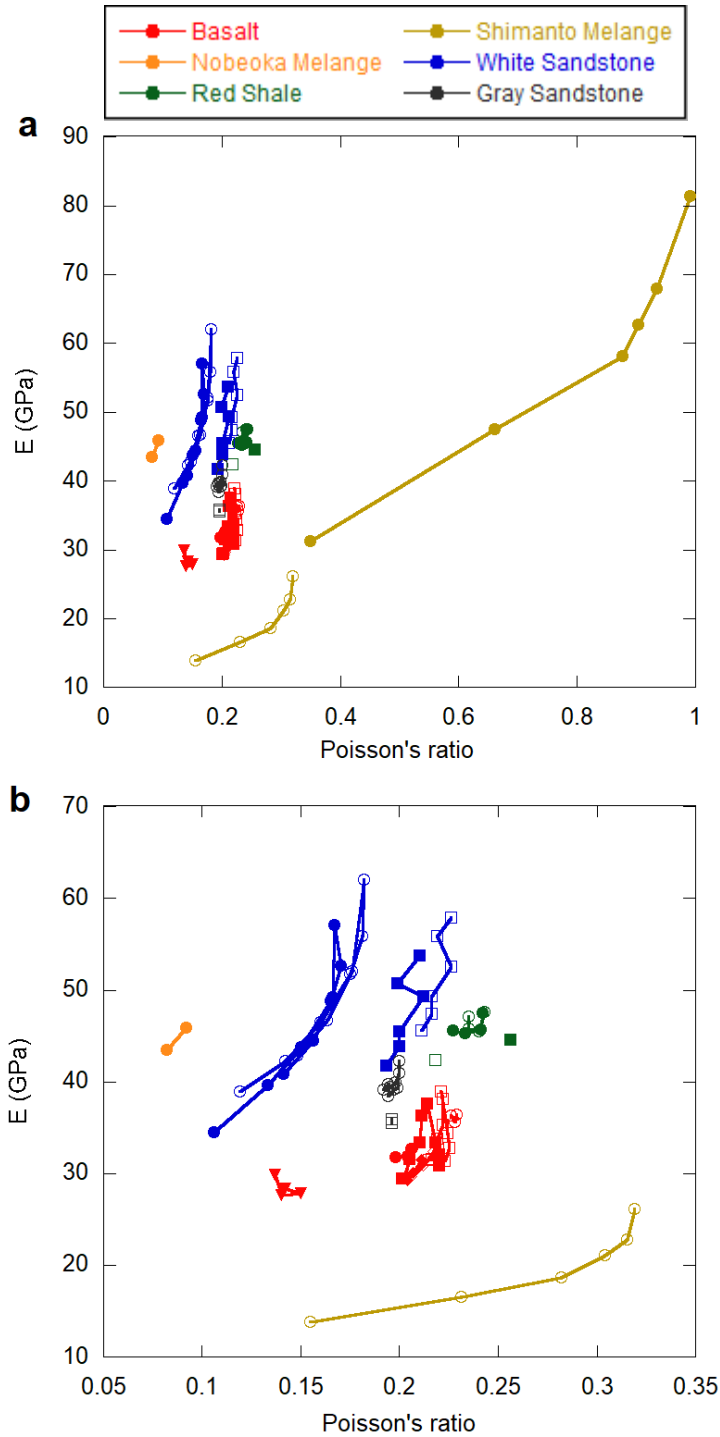
Fig. 21. Young's modulus vs. Poisson's ratio for all lithologies (a) including and (b) excluding the data of the Shimanto mélange obtained from linear strain gauge. Young's moduli measured with a linear strain gauge were compared to Poisson's ratio determined by a combination of an axial linear strain gauge and a radial rosette strain gauge (solid symbols), whereas Young's modulus measured with the rosette strain gauge was compared to Poisson's ratio determined by a combination of axial and radial strains on the rosette strain gauge (open symbols). Different symbols represent different experiments.
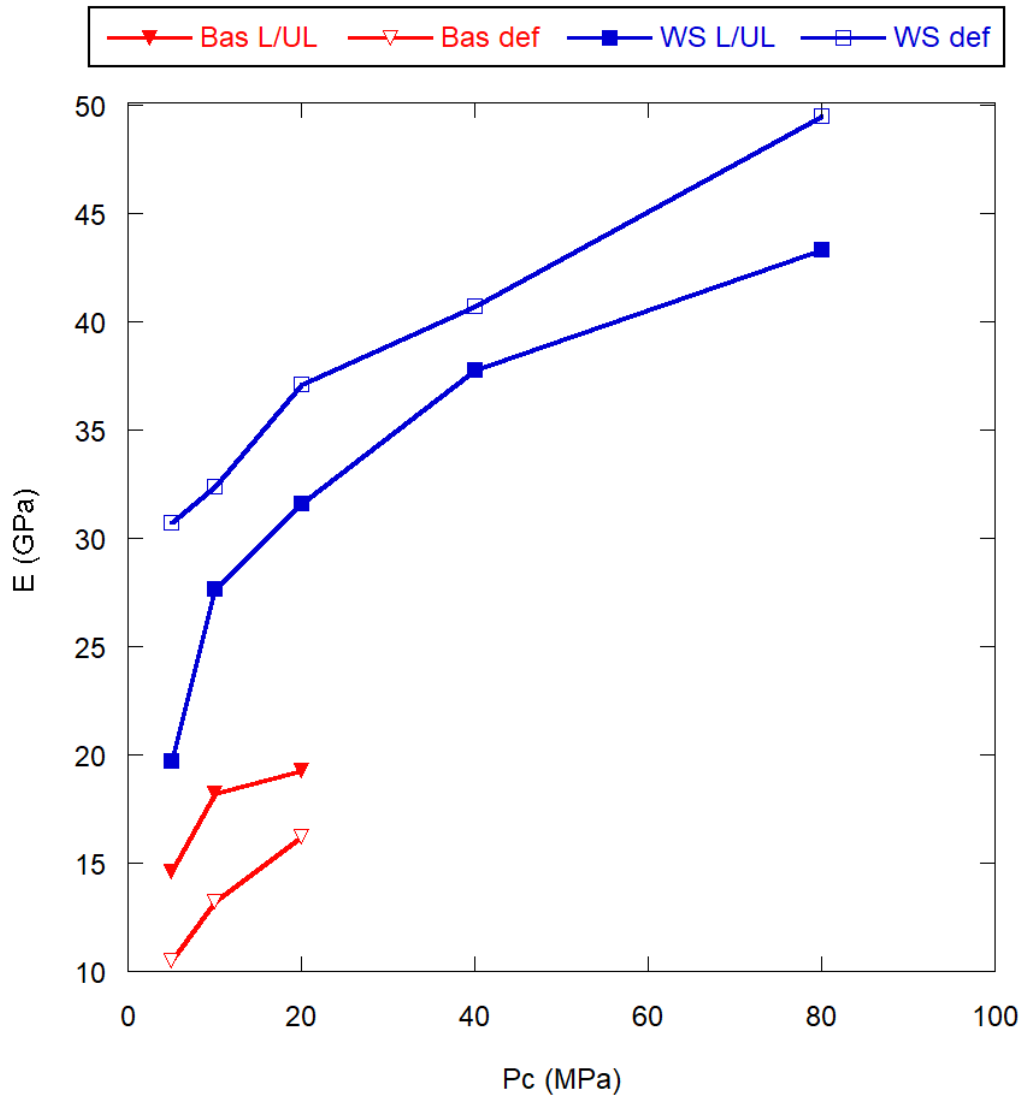
Fig. 22. Comparison of LVDT-derived Young's modulus determined in loading/unloading experiments (solid) and deformation experiments (open) on basalt (blue) and white sandstone (red). Values for loading/unloading experiments are averages of all complete experiments. Bas = Basalt; WS = White Sandstone; L/UL = Load/Unload; Def = Deformation.

determined in the triaxial deformation experiment are lower than the triaxial load/unload experiments by 2-6 GPa. The white sandstone, on the other hand, shows an opposite relation. Young's modulus values determined in the triaxial deformation (28.96-49.50 GPa) are all greater than the averages of the Young's modulus determined during the

loading of the load/unload experiment (19.71-43.35 GPa). Such a different relation

between the Young's modulus determined in triaxial load-unload test and triaxial

deformation test is due to the strain at which the lithology yields. Load/unload

experiments were loaded until 0.50% of the LVDT-derived axial strain, and the yield

point of basalt and white sandstone was 0.40-0.60% and 0.79-1.2%, respectively.

Therefore, the load/unload experiments of basalt are loaded to similar strain as the yield

point. However, the load/unload experiments of white sandstone are loaded to about half

of the strain as the yield point.

The LVDT-derived and strain-gauge-derived Young's modulus of the Nobeoka

mélange in this study is 22.15 and 37.12 GPa, respectively, at effective pressure of 5

MPa. Compared to Young's modulus of the mélanges (Nobell 142: 23 GPa, Nobell 153:

22 GPa) and at 20 MPa effective pressures (Kitajima et al., 2017), which were

determined using LVDT-derived axial strain, the strain-gauge-derived Young's modulus

of the Nobeoka mélange in this study is about 50% greater and the LVDT-derived

Young's modulus is similar to the Young's modulus of the mélanges. Therefore, the

Nobeoka mélange of this study has similar mechanical behaviors to the mélanges studied

in Kitajima et al. (2017).

Fracture strength shows a strong linear correlation to the average Young's

modulus at each confining pressure (Fig. 23). There is a limited range of data for the

basalt because brittle deformation was observed only at confining pressure of 5 and 10

MPa. But in those two cases, fracture strength increases with Young's modulus. The

white sandstone exhibits a strong linear and positive correlation between fracture strength

and Young's modulus. The Nobeoka mélange fracture strength barely increases with

Young's modulus (Kitajima et al., 2017).
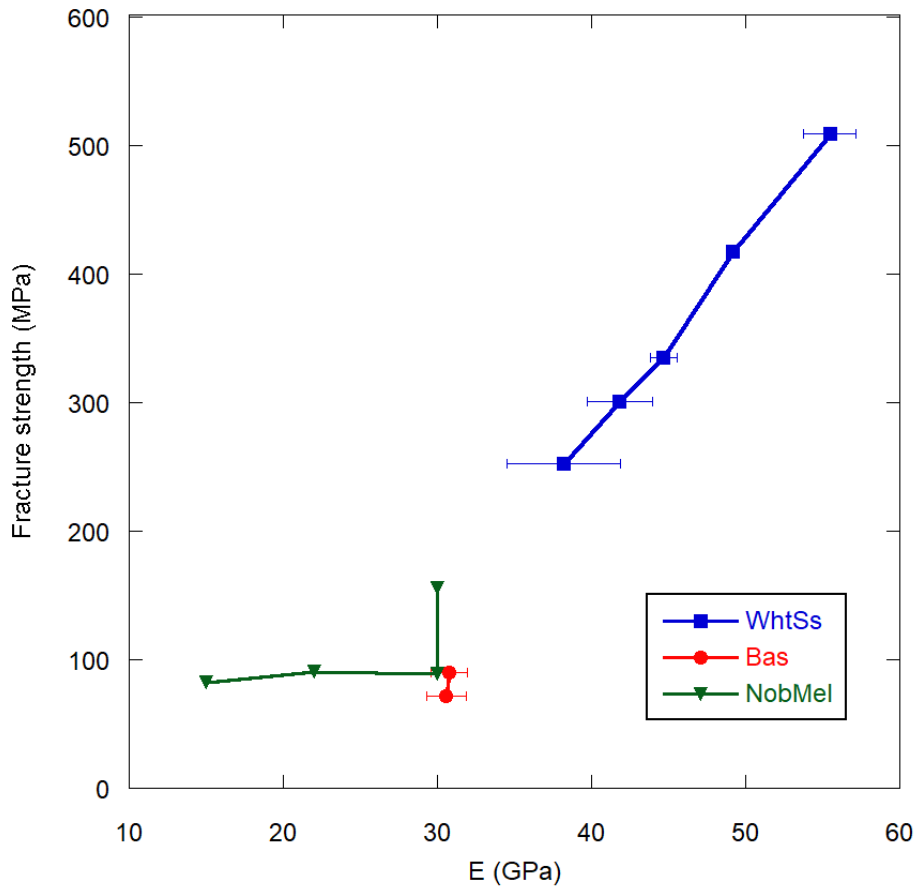
Fig. 23. Fracture strength as a function of Young's modulus for white sandstone (blue), basalt (red), and the Nobeoka mélange (green; data from Kitajima et al., 2017).

5.3. Velocities

The acoustic velocities for white sandstone (2.43 to 3.33 km/s) and basalt (2.36 to

3.23 km/s) are primarily between 2 and 3 km/s (Tables 8 and 9). These values are much

smaller than average values for the P-wave velocities for low porosity sandstone reported

from well logging (4-4.9 km/s) in Hamahashi et al. (2015) and basalt from logging data at

the Site C0012 where the rock sample was collected at the Nankai Trough (3.5-5.0 km/s; Strasser et al., 2014). In addition, the velocity of basalt in this study are lower than P-wave velocities of the basalt, which was prepared from the core sample used in this study, of 5.01-5.25 km/s measured at effective pressure of 2.5- 95 MPa (Kitajima, unpublished data). Based on the observations, I conclude that the measured values likely correspond to S-wave velocities not P-wave velocities.

To estimate the P-wave velocity from the measured S-wave velocity, I utilized the Poisson's ratio determined using rosette/rosette strain gauges for the basalt (Bas_A-2, 0.215-0.225) and white sandstone (WS_A-1, 0.119-0.182) (Table 5) to calculate the V_P/V_S ratio at each effective pressure. Using the V_P/V_S ratios and the measured S-wave velocity, I calculate P-wave velocities (Table 10, Fig. 24). At Pc = 5-80 MPa, P-wave velocities for basalt range from 3.92 to 4.52 km/s, with most values falling within 4.2 and 4.5 km/s and P-wave velocities for white sandstone are between 3.70 and 4.35 km/s with most falling within 3.8 and 4.3 km/s. The basalt yields higher P-wave velocities than the white sandstone at all effective pressures tested. This is due to the fact that Poisson's ratio of the basalt (0.215-0.225) used for calculating the P-wave velocity is 33-80% greater than the Poisson's ratio for the white sandstone (0.119-0.182). Comparison of the calculated values to the reported values in the literature (Strasser et al., 2014 – basalt, 3.5-5.0 km/s; Kitajima, unpublished – basalt: 5.01-5.25 km/s; Hamahashi et al., 2015 – sandstone: 4.0-4.9 km/s), most of the calculated P-wave velocities are within the expected range.

Table 10. Average acoustic velocities measured from acoustic pulsar experiments. Poisson's ratio for basalt and white sandstone were used to calculate the P-wave velocities.

Pc (MPa)	Basalt		White sandstone	
	V_S (km/s)	V_P (km/s)	V_S (km/s)	V_P (km/s)
5	2.60	4.31	2.43	3.70
10	2.36	3.92	2.50	3.87
20	2.61	4.35	2.63	4.13
40	2.70	4.52	2.73	4.35
60	2.62	4.38	2.65	4.25
80	2.60	4.35	2.64	4.23
60	3.23	5.41	3.33	5.34
40	2.73	4.58	2.48	3.96
20	2.99	5.02	2.77	4.37
10	2.68	4.49	2.54	3.95
5	2.58	3.65	-	-
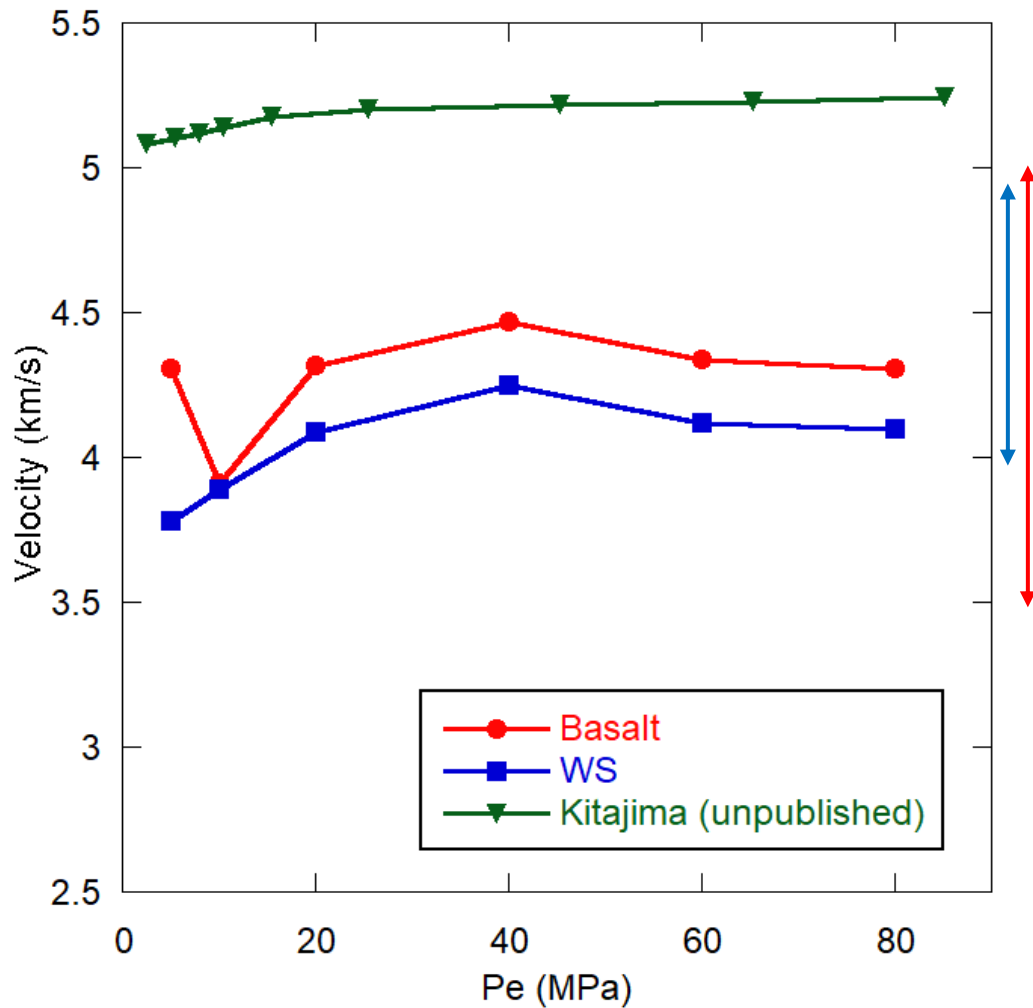
Fig. 24. Calculated P-wave velocities for basalt and white sandstone (red and blue, respectively) compared to lower porosity basalt (green, Kitajima, unpublished). P-wave velocities from logging data for sandstone (Hamahashi et al., 2015) and basalt (Strasser et al., 2015) are shown in blue and red arrows, respectively.

5.3.1. Static vs Dynamic Elastic Moduli

At each confining pressure step, I computed the P-wave modulus and shear

modulus from the bulk density and acoustic velocity measurements (assuming isotropic,

elastic media), as given by:

$$M_a = \rho V_P^2 \tag{12}$$

$$G_a = \rho V_S^2 \tag{13}$$

where M is the P-wave modulus, ρ is the bulk density, V_P is the P-wave velocity, G is the

shear modulus, and V_S is the S-wave velocity. The other elastic moduli were computed

from the shear and P-wave velocities, as given by:

$$K_a = M_a - \frac{4}{3}G_a \tag{14}$$

$$\lambda_a = M_a - 2G_a \tag{15}$$

$$E_a = \frac{G_a(3M_a - 4G_a)}{M_a - G_a} \tag{16}$$

$$\nu_a = \frac{M_a - 2G_a}{2M_a - 2G_a} \tag{17}$$

where K_a is the bulk modulus, E_a is the Young's modulus, ν_a is the Poisson's ratio, λ_a is

Lamé's first parameter, G_a is the shear modulus, and M_a is the P-wave modulus.

Comparison of the dynamic to the static moduli is meaningful only in the shear

modulus because Vp was not measured but calculated based on Vs and Poisson's ratio.

The dynamic shear modulus of basalt (~18 GPa) is approximately 50% greater than static

shear modulus (~12 GPa). Fjær (2009) reported a similar relationship between the static

and dynamic elastic moduli for a porous sandstone ($\varphi = 28.8\%$). The dynamic shear

modulus of white sandstone (~18 GPa) is approximately equivalent to the static shear

modulus (~18 GPa).

To compare the Poisson's ratio of Nobeoka mélange in this study, acoustic

velocity and velocity ratio values were estimated from Tsuji et al. (2006) (Figure 3d,

Table 11) . Poisson's ratios of Nobeoka mélange determined in the triaxial load/unload

tests are 0.05-0.15, which is in the range of the Poisson's ratio (-0.27-0.11) calculated

from the V_P and V_S values for the same unit (Tsuji et al., 2006) (Table 10). The similarity

in Poisson's ratio confirms that the use of Poisson's ratio to calculate V_P from V_S is a

reasonable assumption.

Table 11. Average estimated velocity and Poisson's ratio values for Nobeoka mélange (Figure 3d - Tsuji et al., 2006).

Pc (MPa)	Mélange (Footwall)			Phyllite (Hanging wall)		
	V_P (km/s)	V_S (km/s)	Poisson's ratio	V_P (km/s)	V_S (km/s)	Poisson's ratio
5	2.70 ± 0.00	2.10 ± 0.00	-0.2656	4.90 ± 0.40	3.00 ± 0.30	0.2002
10	3.05 ± 0.35	2.25 ± 0.05	-0.0970	4.70 ± 0.40	3.05 ± 0.25	0.1363
15	3.25 ± 0.25	2.35 ± 0.05	-0.0479	4.80 ± 0.50	3.15 ± 0.25	0.1218
20	3.40 ± 0.30	2.45 ± 0.05	-0.0400	4.90 ± 0.50	3.15 ± 0.25	0.1478
25	3.60 ± 0.20	2.50 ± 0.00	0.0343	4.95 ± 0.45	3.15 ± 0.25	0.1597
30	3.75 ± 0.15	2.75 ± 0.05	-0.0817	5.00 ± 0.40	3.20 ± 0.20	0.1531
35	3.85 ± 0.15	2.65 ± 0.05	0.0498	5.10 ± 0.40	3.20 ± 0.20	0.1753
40	3.95 ± 0.15	2.65 ± 0.05	0.0908	5.15 ± 0.35	3.20 ± 0.20	0.1856
45	4.00 ± 0.20	2.65 ± 0.05	0.1089	5.15 ± 0.35	3.25 ± 0.15	0.1691
50	4.10 ± 0.20	2.75 ± 0.05	0.0911	5.15 ± 0.35	3.25 ± 0.15	0.1691
55	4.15 ± 0.15	2.75 ± 0.05	0.1086	5.15 ± 0.35	3.25 ± 0.15	0.1691

5.4. Reflection Coefficients

For basalt and white sandstone, the acoustic impedance, Z, is calculated as a

function of effective pressure (P_e) as given by:

$$Z\ (P_e) = \rho \times V_P(P_e) \tag{17}$$

where ρ is the bulk density determined by mass and volume measurement and V_P is the P-wave velocity determined in the previous section. The calculated impedance values increase with effective pressure (Fig. 25; Table 12). Acoustic impedance values of the white sandstone (9.85-11.6 $\times10^6$ Pa·s/m) are greater than those of the basalt (9.90-11.4 $\times10^6$ Pa·s/m) for all effective pressures except for $P_e = 5$ MPa.

To better understand the effects of lithologies and the possible stress and pressure conditions on the seismic reflection along the plate boundary faults at depth, the reflection coefficient across the boundary between the layers composed of two different lithologies is calculated assuming normal incidence. The reflection coefficient, R, is expressed as

$$R = \frac{Z_2 - Z_1}{Z_2 + Z_1} \tag{18}$$

where Z_1 and Z_2 are the acoustic impedance values of the upper and lower media. I consider various scenarios with different lithologies under different stress states. The considered lithology models include: (1) white sandstone over basalt, (2) white sandstone over mélange, (3) mélange over white sandstone, (4) mélange over basalt, and (5) Nobeoka thrust (hanging wall phyllite over footwall mélange). The considered stress states include a hydrostatic pore pressure case (Fig. 26) and various overpressured conditions in either the upper layer or lower layer at different depths (1-6 km) (Figs. 27-31). The overpressure is denoted as ΔP_p, where:

$$\Delta P_P = P_P - P_{P\_hydro} \tag{19}$$

where P_p is the pore pressure in the system and P_{p_hydro} is the hydrostatic pore pressure.

Table 12. Calculated acoustic impedance values from velocities and densities. Wet bulk densities are 2663, 2524, 2600, and 2680 g/cm³ for white sandstone, basalt, Nobeoka footwall mélange, and Nobeoka hanging wall mélange, respectively.

	Acoustic Impedance (x10⁶ Pa·s/m)			
Pc = Pe (MPa)	*White Sandstone*	*Basalt*	*Nobeoka Mélange*	*Nobeoka Phyllite*
5	9.85 ± 0.38	10.9 ± 0.25	7.02 ± 0.00	13.1 ± 1.07
10	10.3 ± 0.15	9.90 ± 0.71	7.93 ± 0.91	12.6 ± 1.61
15	-	-	8.45 ± 0.65	12.9 ± 1.34
20	11.0 ± 0.10	11.0 ± 0.70	8.84 ± 0.78	13.1 ± 1.34
25	-	-	9.36 ± 0.52	13.3 ± 1.21
30	-	-	9.75 ± 0.39	13.4 ± 1.07
35	-	-	10.0 ± 0.39	13.7 ± 1.07
40	11.6 ± 0.29	11.4 ± 0.48	10.3 ± 0.39	13.8 ± 0.94
45	-	-	10.4 ± 0.52	13.8 ± 0.94
50	-	-	10.7 ± 0.52	13.8 ± 0.94
55	-	-	10.8 ± 0.39	13.8 ± 0.94
60	11.3 ± 0.35	11.1 ± 0.25	-	-
80	11.3 ± 0.47	11.0 ± 0.11	-	-
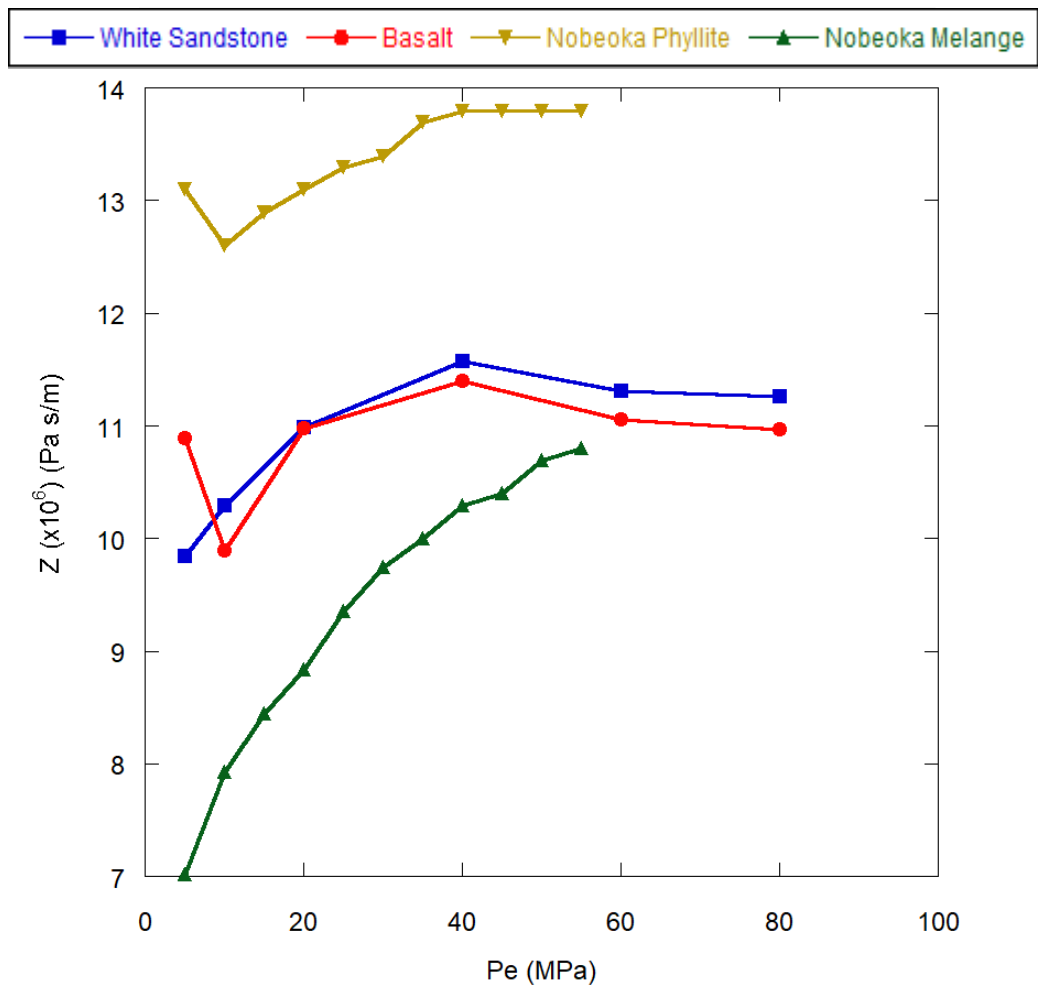
Fig. 25. Acoustic impedance for basalt (red), white sandstone (blue), Nobeoka hanging wall phyllite (yellow), and Nobeoka footwall mélange (green).

Assuming an effective pressure gradient of ~15 MPa/km, which is determined from an

average rock density of 2.60 g/cm^3 over the basalt, white sandstone, and Nobeoka

footwall, effective pressures of 5-80 MPa documented in this study correspond to ~1-6

km depth.
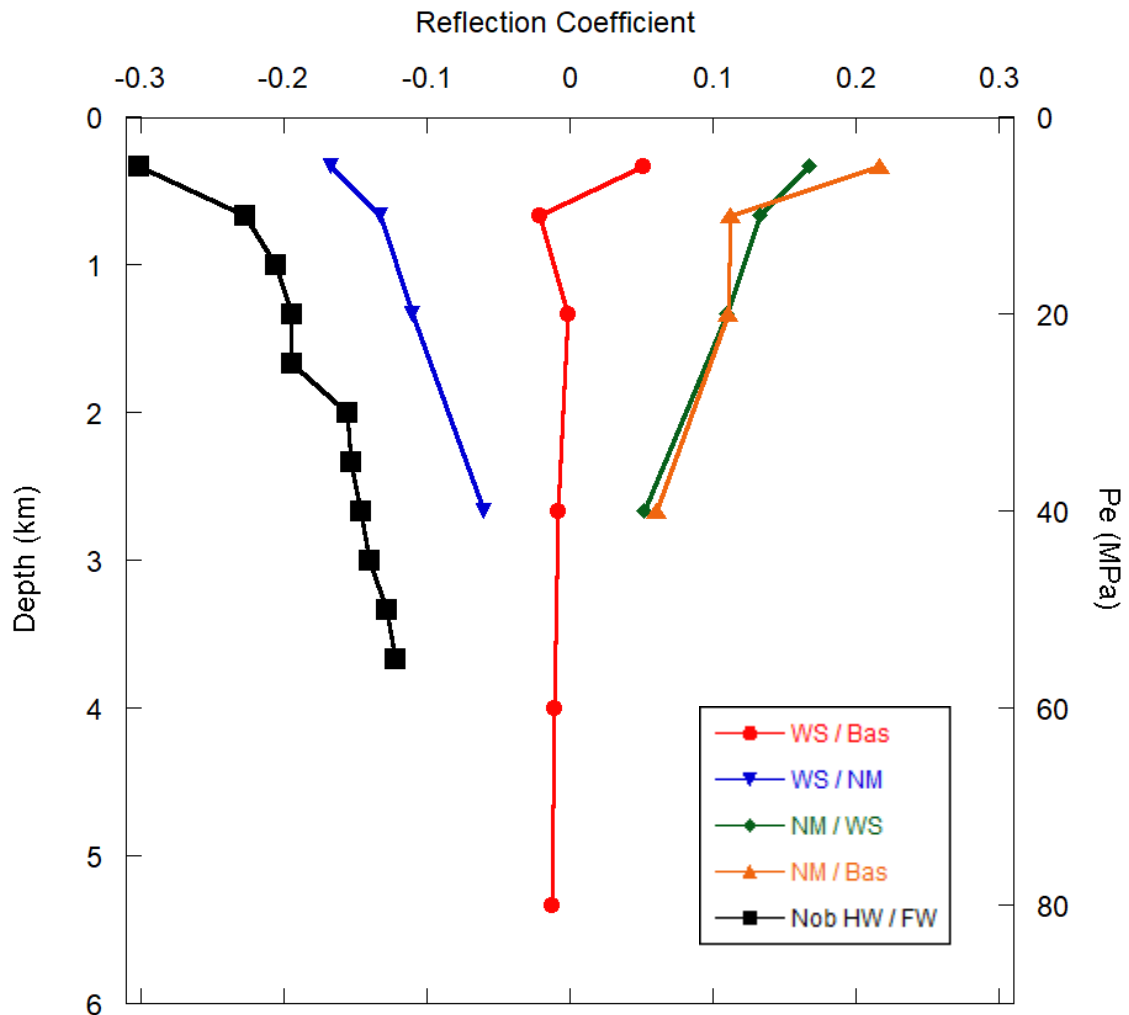
Fig. 26. Reflection coefficient as a function of depth for hydrostatic pore pressure case. The Nobeoka thrust model consists of the hanging wall phyllite and footwall mélange. WS = White Sandstone; Bas = Basalt; NM = Nobeoka Mélange; Nob HW = Nobeoka Hanging Wall (Phyllite); Nob FW = Nobeoka Footwall (Mélange).

Fig. 27. White sandstone over basalt model for (a) overpressured upper layer case and (b) overpressured lower layer case. Vertical axis of effective pressure (Pe) represents the effective pressures of the non-overpressured layer.

67
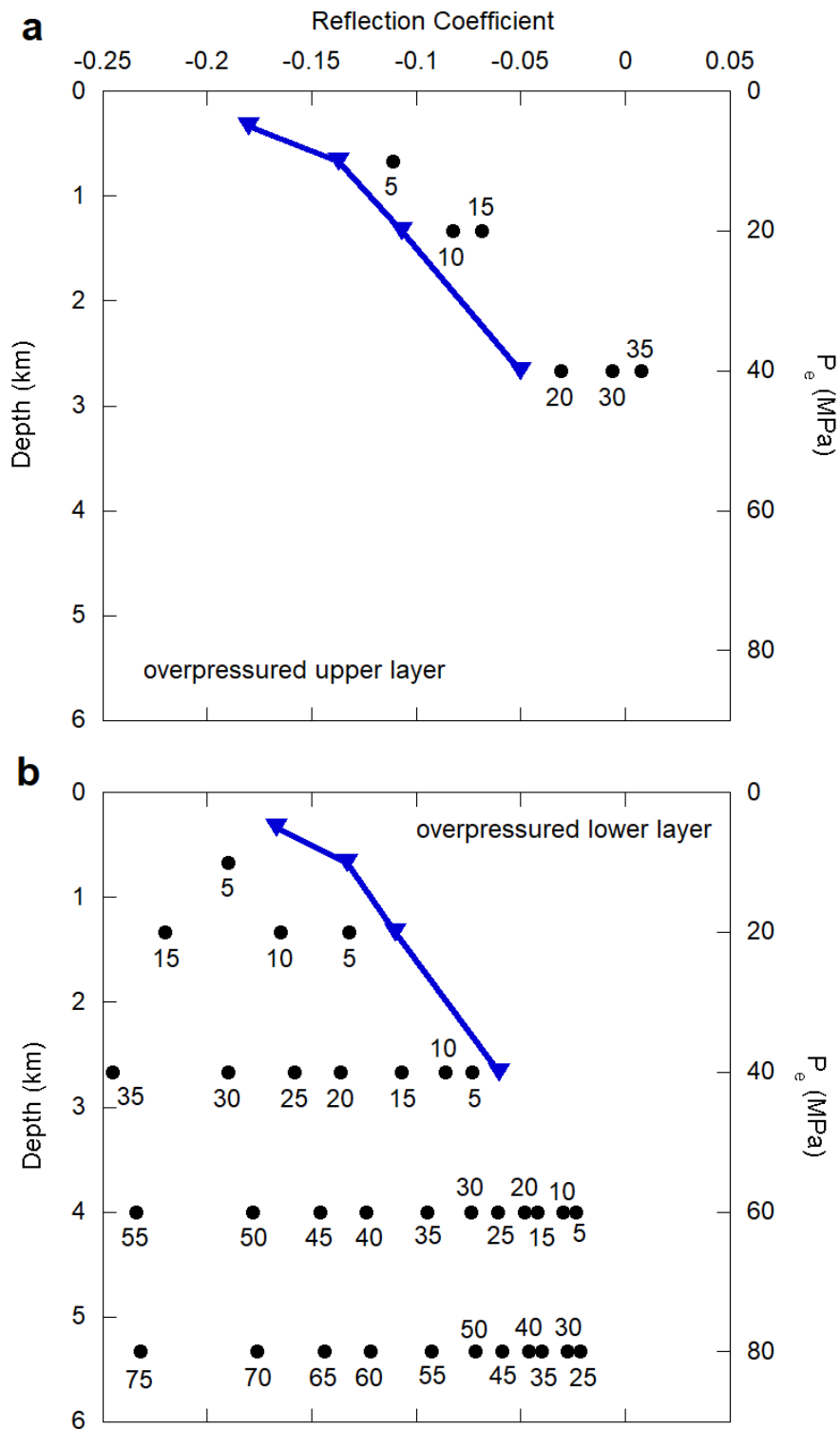
Fig. 28. White sandstone over mélange model for (a) overpressured upper layer case and (b) overpressured lower layer case. Vertical axis of effective pressure (Pe) represents the effective pressures of the non-overpressured layer.

68
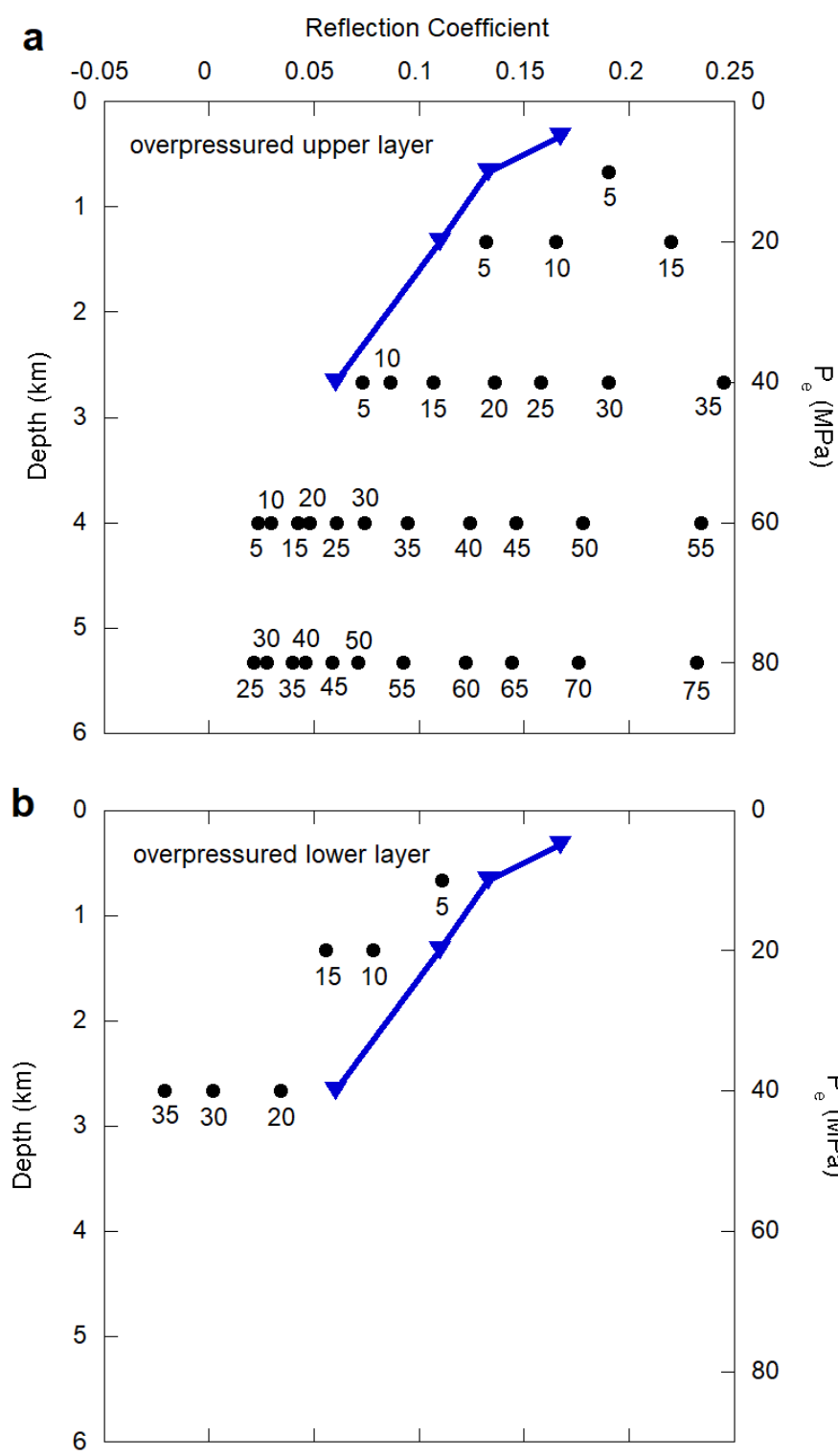
Fig. 29. Mélange over white sandstone model for (a) overpressured upper layer case and (b) overpressured lower layer case. Vertical axis of effective pressure (Pe) represents the effective pressures of the non-overpressured layer.
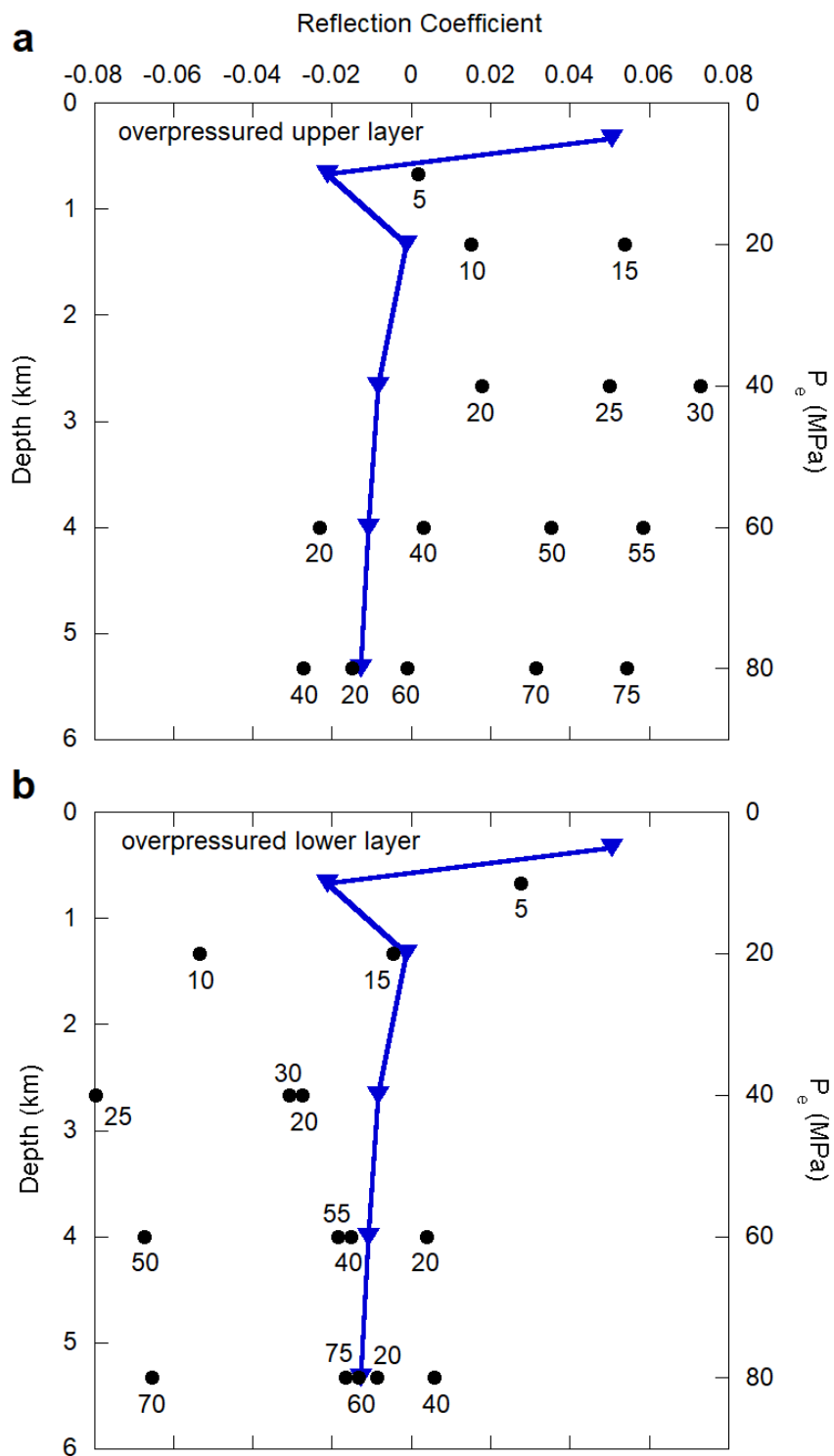
Fig. 30. Mélange over basalt model for (a) overpressured upper layer case and (b) overpressured lower layer case. Vertical axis of effective pressure (Pe) represents the effective pressures of the non-overpressured layer.

Fig. 31. Nobeoka hanging wall phyllite over footwall mélange model for (a) overpressured upper layer case and (b) overpressured lower layer case. Vertical axis of effective pressure (Pe) represents the effective pressures of the non-overpressured layer.
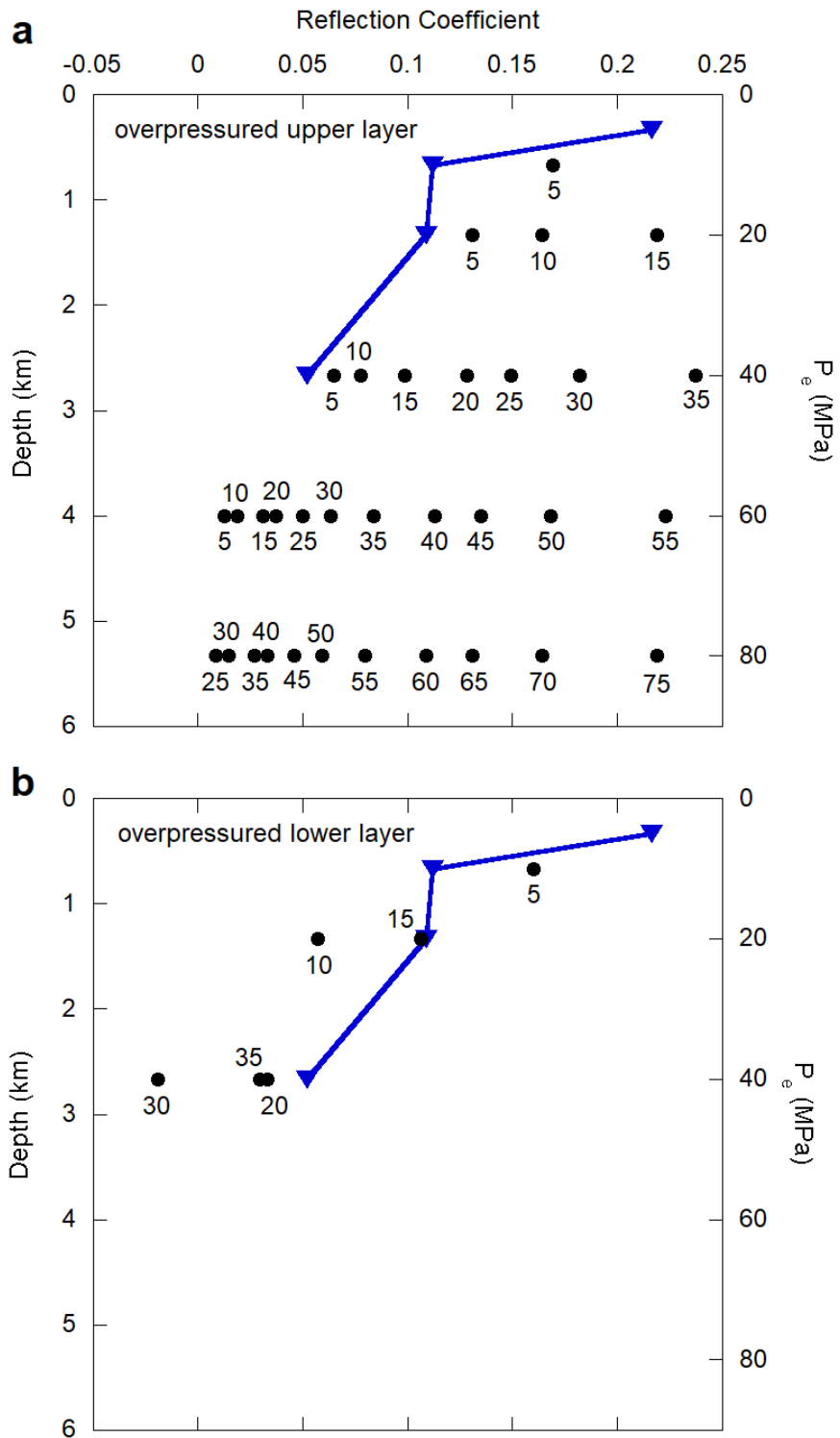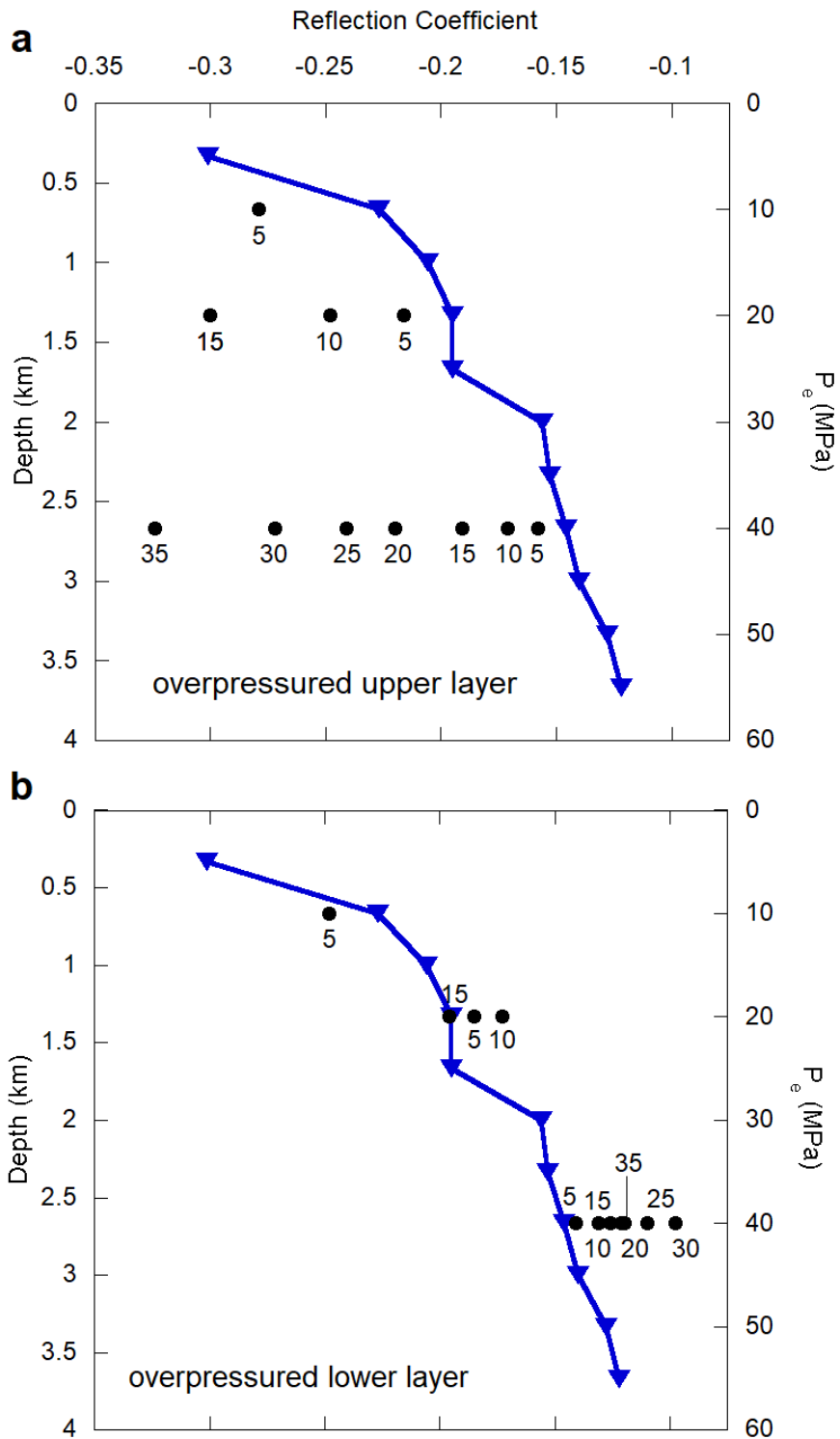
In the case of hydrostatic pore pressure in both upper and lower layers, two models of mélange over basalt and mélange over white sandstone demonstrate positive reflection coefficients at all depths and a decrease in reflection coefficient with increasing effective pressure (depth) (Fig. 26). The mélange over white sandstone has the greatest positive reflection coefficient because the acoustic impedance of the white sandstone is much greater than that of the mélange. The other two models of white sandstone over mélange and Nobeoka thrust models show negative reflection coefficients at all depths and an increase in reflection coefficient with effective pressure. The Nobeoka thrust model demonstrates the greatest negative reflection coefficient due to the acoustic impedance of the phyllite being much greater than the acoustic impedance of the mélange. The white sandstone over basalt shows little dependence of reflection coefficient with increasing effective pressure or depth, due to the minimal difference in acoustic impedance values between the white sandstone and basalt. Overall, all models approach a reflection coefficient toward 0 with increasing effective pressure.

In general, an overpressure in either the upper or lower layer leads to an increase or a decrease in reflection coefficients relative to the hydrostatic case, respectively. An exception is the Nobeoka Thrust model, where the opposite is true. In the white sandstone over basalt model at depths of 4 and 5.3 km (corresponding to effective pressure with hydrostatic pore pressure, $P_{e\_hydro} = P_c - P_{p\_hydro} = 60$ and 80 MPa, respectively), reflection coefficients of a few cases of overpressured upper layer are less than hydrostatic case ($\Delta Pp = 20$ MPa and $\Delta Pp = 20$ and 40 MPa, respectively). Additionally, several cases of the overpressured lower layer reflection coefficients at the same depth are greater than the hydrostatic case ($\Delta Pp = 20$ MPa and $\Delta Pp = 20$, 40, and 60 MPa, respectively) (Fig.

27). Furthermore, in the white sandstone over mélange, mélange over white sandstone, and Nobeoka thrust models, an increase in the excess pore pressure (ΔP_p) increases the difference between the overpressured case and the hydrostatic case (Figs. 28, 29, and 31). The same is true for the overpressured upper layer case for the mélange over basalt (Fig. 31a). In the white sandstone over basalt model (Fig. 27) and the overpressured footwall case of the mélange over basalt model (Fig. 30b), there is no correlation between excess pore pressure (ΔP_p) and difference from the hydrostatic case.

At the Nankai Trough, both normal and reverse polarity was observed along strike of the décollement near the deformation front at a depth of approximately 0.4-1 km (P_{e_hydro} = 5-15 MPa) (Fig. 32; Park et al. 2014). Reflection coefficient is reported as -0.036, 0.030, -0.064, and 0.095 at different locations. Among the model results for ~0.7 km (P_{e_hydro} = 10 MPa), the white sandstone over basalt model with hydrostatic pore pressure generates reflection coefficient values of ~-0.036; the white sandstone over basalt model with ΔP_p = 5 MPa in the lower layer yields reflection coefficient values of ~0.030; the mélange over basalt and mélange over white sandstone models with hydrostatic pore pressure, as well as the mélange over white sandstone model with ΔP_p = 5 MPa in the lower layer generate reflection coefficient values of ~0.095. At ~1 km depth (P_{e_hydro} = 15 MPa), the white sandstone over mélange case with ΔP_p = 10 MPa in the upper layer generates reflection coefficient values of ~-0.064; the mélange over white sandstone model with ΔP_p = 5 and 10 MPa in the lower layer yields reflection coefficient values of ~0.095. Although similar reflection coefficient values can be generated by the models of white sandstone over basalt, white sandstone over mélange, and mélange over white sandstone, they may not represent the real formation because at such shallow

73
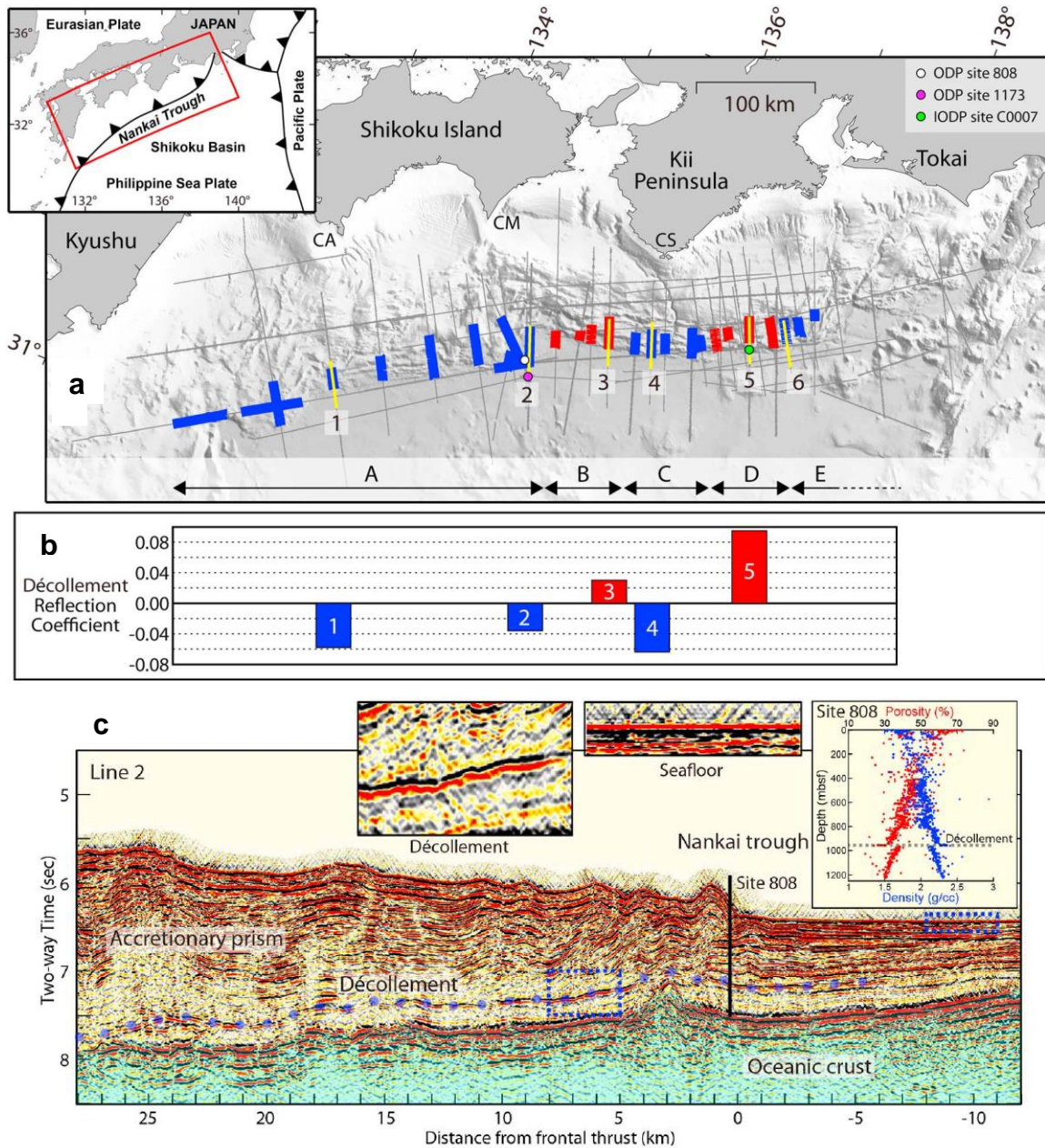
Fig. 32. (a) Bathymetry map of the Nankai Trough. Blue and red lines coordinate with (b) and show reverse and normal polarity reflections, respectively, of the décollement. (b) Mean décollement reflection coefficients for lines 1 through 5 on (a). (c) Time-migrated seismic profile of the Nankai Trough (modified from Park et al., 2014). Décollement is the blue dashed line. On the inlet figures, porosity and density profiles at Site 808 are shown.

depth, porosity ranging from 30-70% (Fig. 32) is much higher than that of lithologies

considered in the models (1.50-11.0%).

At deeper depth (6-10 km), reflection coefficients for a splay fault are reported as 0.026, -0.050, 0.046, and -0.047, for zones A, B, C, and D, respectively (Tsuru et al., 2005; Fig. 33). Based on the model results for ~5 km (P_{e_hydro} = 80 MPa), 4 scenarios yield a reflection coefficient of 0.026; 1 scenarios yields -0.050; 6 scenarios yield 0.046; and 1 scenarios yield -0.047 (Figs. 27-31). The 4 scenarios for the reflection coefficient of 0.026 include one scenario on the mélange over white sandstone model with ΔP_p = 30 MPa in the upper layer and three models of the mélange over basalt model with different overpressures (ΔP_p = 30, 35, and 40 MPa) in the upper layer. The white sandstone over basalt model with ΔP_p = 70 MPa in the lower layer generates reflection coefficient values of ~-0.050. The models that yield reflection coefficients of ~0.046 include 1 white sandstone over basalt model with ΔP_p = 75 MPa in the upper layer; 1 mélange over white sandstone model with ΔP_p = 40 MPa in the upper layer, and 4 mélange over basalt models with ΔP_p = 35, 40, 45, and 50 MPa in the upper layer. The white sandstone over mélange model with ΔP_p = 40 MPa in the footwall yields reflection coefficient values of
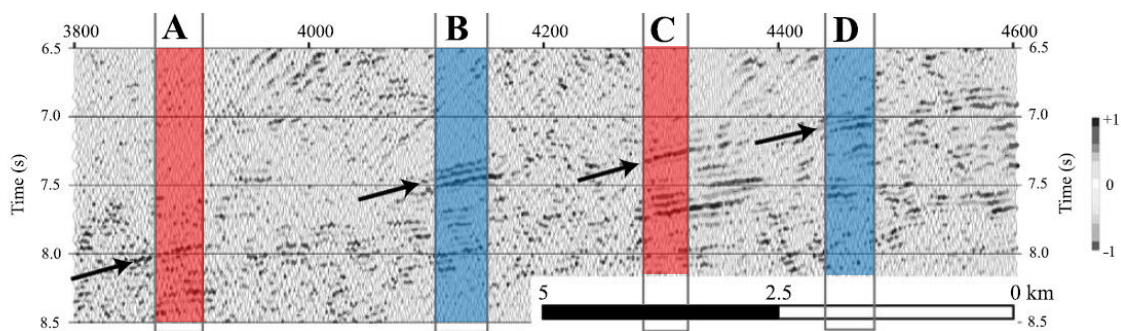
Fig. 33. Cross correlation between seafloor reflectors and near-trace records offshore of the Kii Peninsula (modified from Tsuru et al., 2005). Arrows identify target reflections from the splay fault. Depth decreases from zone A to zone D. Polarity is positive in zones A and C (red) and negative in zones B and D (blue).

~-0.047. The Nobeoka thrust model does not generate reflection coefficients similar to the splay fault.

Identifying a specific scenario for one reflection coefficient is difficult assuming models with different lithologies over a range of effective pressures (depths) from the simple models which assume simple two layers and calculate the reflection coefficients the angle of incidence of 0°. For example, 6 scenarios at deeper depth with different lithology and pressure combinations can generate the reflection coefficient of 0.046. However, this study was able to constrain the 44 total scenarios at ~5 km depth (P_{e_hydro} = 80 MPa) to 12 scenarios. Careful determination of physical properties on possible lithologies at appropriate conditions can provide realistic rock properties. These physical properties can aid to create synthetic seismograph with complicated structure (e.g., multiple layers, fault zones thickness) in the future work.

6. CONCLUSIONS

A suite of laboratory experiments reveals that the mechanical and physical properties vary with lithology. All the tested samples including basalt (porosity of 11.0%), Nobeoka mélange (1.5%), Shimanto mélange (5.5%), Shimanto white sandstone (2.6%), Shimanto gray sandstone (2.3%), and Shimanto red shale (3.2%) exhibit an increase in Young's modulus and Poisson's ratio with increasing pressure ranging from 4.73-27.6 GPa and 0.008-0.136, respectively, at confining pressure between 0 and 80 MPa. Young's modulus increases with Poisson's ratio, and lithologies with higher Poisson's ratio values have lower Young's modulus values. At higher pressures, Young's modulus has a greater rate of increase than Poisson's ratio. The triaxial deformation experiments exhibit that the white sandstone deforms brittle at effective pressure of 5-80 MPa, whereas the basalt deforms brittle at 5 and 10 MPa and ductile at 20 MPa. The fracture strength of the white sandstone is approximately three times greater than that of basalt. Although P-wave velocity was not successfully measured but computed from S-wave velocity and Poisson's ratio, the P-wave and S- wave velocities for the white sandstone and basalt range from 3.70-5.41 and 2.43-3.33 km/s. From the P-wave velocities, the acoustic impedance for the white sandstone and basalt range from 9.85-14.2 $\times 10^6$ Pa·s/m.

Using the experimental data, the forward models with different lithology at different stress conditions were created to estimate reflection coefficient on the plate fault boundary. In the hydrostatic pore pressure cases, whether the model generated positive or negative reflection coefficient values, the absolute magnitude of all models decreased with increasing effective pressure (depth). In general, the reflection coefficients generated

in overpressured upper layer scenarios are greater than the hydrostatic pore pressure scenario, whereas in scenarios with an overpressured lower layer, generated reflection coefficients are less than the hydrostatic pore pressure scenario. 18 scenarios out of 64 scenarios considered can explain the reflection coefficient observed along the plate boundary fault at shallower depth near the deformation front (-0.064-0.036) and deeper depth (-0.050-0.046) in the Nankai Trough. There is no noticeable trend in the shallower depth, but at deeper depth, 40, 70, and 75 MPa excess pore pressure in the hanging wall and 30-50 MPa excess pore pressure in the footwall are required for the negative and positive observed reflection coefficients, respectively.

This study presents the effects of lithology on physical properties of rocks. The physical properties determined in this study can be used to create more realistic synthetic seismographs for the subduction zones by taking into account fault structures in the future study.

REFERENCES

Ameen, M. S., Smart, B. G., Somerville, J. M., Hammilton, S., Naji, N. A., 2009.

Predicting rock mechanical properties of carbonates from wireline logs (A case

study: Arab-D reservoir, Ghawar field, Saudi Arabia). Marine and Petroleum

Geology 26, 430-444.

Ando, M., 1975. Source mechanisms and tectonic significance of historical earthquakes

along the Nankai Trough, Japan. Tectonophysics 27, 119-140.

Ballance, P., Scholl, D., Vallier, T., Stevenson, A., Ryan, H., Herzer, R., 1989.

Subduction of a Late Cretaceous seamount of the Louisville Ridge at the Tonga

Trench: A model of normal and accelerated tectonic erosion. Tectonics 8, 953-

962.

Bangs, N.L.B., Moore, G.F., Gulick, S.P.S., Pangborn, E.M., Tobin, H.J., Kuramoto, S.,

Taira, A., 2009. Broad, weak regions of the Nankai Megathrust and implications

for shallow coseismic slip. Earth and Planetary Science Letters, 284, 44-49.

Bauer, K., Schulze, A., Ryberg, T., Sobolev, S.V., Weber, M.H., 2003. Classification of

lithology from seismic tomography: a case study from the Messum igneous

complex, Namibia. Journal of Geophysical Research: Solid Earth 108, B3.

Brace, W.F., Martin III, R.J., 1968. A test of the law of effective stress for crystalline

rocks of low porosity. International Journal of Rock Mechanics and Mining

Sciences 5, 415-426.

Christensen, N.I., Hyndman, R.D., Hull, J.M., Salisbury, M.H., 1978. Seismic velocities, electrical resistivities, densities, and porosities of basalts from DSDP Leg 46. Initial Reports of the Deep Sea Drilling Project 46, 383-388.

Cloos, M.,1992. Thrust-type subduction-zone earthquakes and seamount asperities: A physical model for seismic rupture. Geology 20, 601-604.

Close, F., McCavitt, R.D., Smith, B., 2008. Deepwater Gulf of Mexico development challenges overview. In: SPE North Africa Technical Conference & Exhibition.

Collot, J.Y., Fisher, M., 1989. Formation of forearc basins by collision between seamounts and accretionary wedges: an example from the New Hebrides subduction zone. Geology 17, 930-933.

DeMets, C., Gordon, R.G., Argus, D.F., 2010. Geologically current plate motions. Geophysical Journal International 181, 1-80.

Dominguez, S., Lallemand, S., Malavieille, J., Von Huene, R., 1998. Upper plate deformation associated with seamount subduction. Tectonophysics 293, 207-224.

Dominguez, S., Malavieille, J., Lallemand, S., 2000. Deformation of accretionary wedges in response to seamount subduction: Insights from sandbox experiments. Tectonics 19, 182-196, doi:10.1029/1999TC900055.

Dumitru, T.A., Wakabayashi, J., Wright, J.E., Wooden, J.L., 2010. Early Cretaceous transition from nonaccretionary behavior to strongly accretionary behavior within the Franciscan subduction complex. Tectonics 29, TC5001.

Fisher, D., Byrne, T., 1987. Structural evolution of underthrusted sediments, Kodiak Islands, Alaska. Tectonics 6, 775-793.

Fjær, E., 2009. Static and dynamic moduli of a weak sandstone. Geophysics74, WA103-WA112.

Fukuchi, R., Fujimoto, K., Kameda, J., Hamahashi, M., Yamaguchi, A., Kimura, G., Hamada, Y., Hashimoto, Y., Kitamura, Y., Saito, S., 2014. Changes in illite crystallinity within an ancient tectonic boundary thrust caused by thermal, mechanical, and hydrothermal effects: an example from the Nobeoka Thrust, southwest Japan. Earth, Planets and Space 66, 116.

Hamahashi, M., Saito, S., Kimura, G., Yamaguchi, A., Fukuchi, R., Kameda, J., Hamada, Y., Kitamura, Y., Fujimoto, K., Hashimoto, Y., Hina, S., Eida, M., 2013. Contrasts in physical properties between the hanging wall and footwall of an exhumed seismogenic megasplay fault in a subduction zone—an example from the Nobeoka Thrust Drilling Project. Geochemistry, Geophysics, Geosystems 14, 5354-5370.

Hamahashi, M., Hamada, Y., Yamaguchi, A., Kimura, G., Fukuchi, R., Saito, S., Kameda, J., Kitamura, Y., Fujimoto, K., Hashimoto, Y., 2015. Multiple damage zone structure of an exhumed seismogenic megasplay fault in a subduction zone-a study from the Nobeoka Thrust Drilling Project. Earth, Planets and Space 67, 30.

Hashimoto, Y., Abe, S., Tano, H., Hamahashi, M., Saito, S., Kimura, G., Yamaguchi, A., Fukuchi, R., Kameda, J., Hamada, Y., Kitamura, Y., Fujimoto, K., Hina, S., Eida, M., 2017. Acoustic properties of deformed rocks in the Nobeoka thrust, in the Shimanto Belt, Kyushu, Southwest Japan. Island Arc 26, E12198.

Honda, R., Kono, Y., 2005. Buried large block revealed by gravity anomalies in the

    Tonakai and Nankai earthquakes regions, southwestern Japan. Earth, planets and

    space 57, 1–4.

Imai, I., 1971. Geologic structure and metamorphic zonation of the northeastern part of

    the Shimanto terrane in Kyushu, Japan. Journal of the Geological Society of Japan

    77, 207-220.

Isozaki, Y., Aoki, K., Nakama, T., Yanai, S., 2010. New insight into a subduction-related

    orogen: A reappraisal of the geotectonic framework and evolution of the Japanese

    Islands. Gondwana Research 18, 82-105.

Kameda, J., Raimbourg, H., Kogure, T., Kimura, G., 2011. Low-grade metamorphism

    around the down-dip limit of seismogenic subduction zones: Example from an

    ancient accretionary complex in the Shimanto Belt, Japan. Tectonophysics 502,

    383-392.

Karacan, C.Ö., 2009. Elastic and shear moduli of coal measure rocks derived from basic

    well logs using fractal statistics and radial basis functions. International Journal of

    Rock Mechanics and Mining Sciences 46, 1281-1295.

Kato, A., Sakaguchi, A., Yoshida, S., Yamaguchi, H., Kaneda, Y., 2004. Permeability

    structure around an ancient exhumed subduction-zone fault. Geophysical

    Research Letters 31, doi:10.1029/2003GL019183.

Kimura, G., Mukai, A., 1991. Underplated units in an accretionary complex: Melange of

    the Shimanto Belt of eastern Shikoku, southwest Japan. Tectonics 10, 31-50.

Kimura, G., Hamahashi, M., Okamoto, S., Yamaguchi, A., Kameda, J., Raimbourg, H.,

    Hamada, Y., Yamaguchi, H., Shibata, T., 2013. Hanging wall deformation of a

seismogenic megasplay fault in an accretionary prism: The Nobeoka Thrust in southwestern Japan. Journal of Structural Geology 52, 136-147.

Kimura, G., Hashimoto, Y., Kitamura, Y., Yamaguchi, A., Koge, H., 2014. Middle Miocene swift migration of the TTT triple junction and rapid crustal growth in southwest Japan: A review. Tectonics 33, 1219-1238.

Kitajima, H., Takahashi, M., Otsubo, M., Saffer, D., Kimura, G., 2017. Strength and deformation behavior of the Shimanto accretionary complex across the Nobeoka thrust. Island Arc 26, E12192.

Kodaira, S., Takahashi, N., Nakanishi, A., Miura, S., Kaneda, Y., 2000. Subducted seamount imaged in the rupture zone of the 1946 Nankaido earthquake. Science 289, 104-106.

Kodaira, S., Kurahismo, E., Park, J., Takahashi, N., Nakanishi, A., Miura, S., Iwasaki, T., Hirata, T., Kaneda, Y., 2002. Structural factors controlling the rupture process of a megathrust earthquake at the Nankai trough seismogenic zone. Geophysical Journal International 149, 815-835.

Kodaira, S., Nakanishi, A., Park, J., Ito, A., Tsuru, T., Kaneda, Y., 2003. Cyclic ridge subduction at an inter-plate locked zone off central Japan. Geophysical Research Letters 30, doi:10.1029/2002GL016595.

Kodaira, S., Iidaka, T., Kato, A., Park, J. O., Iwasaki, T., Kaneda, Y., 2004. High pore fluid pressure may cause silent slip in the Nankai Trough. Science 304, 1295-1298.

Kondo, H., Kimura, G., Masago, H., Ohmori-Ikehara, K., Kitamura, Y., Ikesawa, E., Sakaguchi, A., Yamaguchi, A., Okamoto, S., 2005. Deformation and fluid flow of

a major out-of-sequence thrust located at seismogenic depth in an accretionary

complex: Nobeoka Thrust in the Shimanto Belt, Kyushu, Japan. Tectonics 24,

TC6008, doi:10.1029/2004TC001655.

McCann, D.M., Entwisle, D.C., 1992. Determination of Young's modulus of the rock

mass from geophysical well logs. Geological Society, London, Special

Publications 65, 317-325.

Miyazaki, S., Heki, K., 2001. Crustal velocity field of southwest Japan: Subduction and

arc–arc collision. Journal of Geophysical Research 106, 4305–4326.

Moore, G.F., Shipley, T.H., Stoffa, P.L., Karig, D.E., Taira, A., Kuramoto, S.,

Tokuyama, H., Suyehiro, K., 1990. Structure of the Nankai Trough accretionary

zone from multichannel seismic reflection data. Journal of Geophysical Research:

Solid Earth 95, 8753-8765.

Moore, G.F., Bangs, N.L., Taira, A., Kuramoto, S., Pangborn, E., Tobin, H.J., 2007.

Three-dimensional splay fault geometry and implications for tsunami generation.

Science 318, 1128-1131.

Morgan, J., Bangs, N., 2017. Recognizing seamount-forearc collisions at accretionary

margins: Insights from discrete numerical simulations. Geology 45, 635-638.

Morley, C.K., 1988. Out-of-sequence thrusts. Tectonics 7, 539-561.

Nedimović, M.R., Hyndman, R.D., Ramachandran, K., Spence, G.D., 2003. Reflection

signature of seismic and aseismic slip on the northern Cascadia subduction

interface. Nature 424, 416-420.

Onishi, C.T., Kimura, G., Hashimoto, Y., Ikehara-Ohmori, K., Watanabe, T., 2001.

Deformation history of tectonic melange and its relationship to the underplating

process and relative plate motion: An example from the deeply buried Shimanto

Belt, SW Japan. Tectonics 20, 376-393, doi:10.1029/1999TC001154.

Park, J., Tsuru, T., Kaneda, Y., Kono, Y., Kodaira, S., Takahashi, N., Kinoshita, H.,

1999. A subducting seamount beneath the Nankai accretionary prism off Shikoku,

southwestern Japan. Geophysical Research Letters 26, 931-934.

Park, J.O., Tsuru, T., Kodaira, S., Cummins, P.R., Kaneda, Y., 2002. Splay fault

branching along the Nankai subduction zone. Science 297, 1157-1160.

Park, J.O., Naruse, H., Bangs, N.L., 2014. Along-strike variations in the Nankai shallow

décollement properties and their implications for tsunami earthquake generation.

Geophysical Research Letters, 41, 7057–7064.

Raimbourg, H., Augier, R., Famin, V., Gadenne, L., Palazzin, G., Yamaguchi, A.,

Kimura, G., 2014. Long-term evolution of an accretionary prism: The case study

of the Shimanto Belt, Kyushu, Japan. Tectonics 33, 936-959.

Ruff, L., Kanamori, H., 1983. Seismic coupling and uncoupling at subduction zones.

Tectonophysics 99, 99-117.

Sagiya, T., Thatcher, W., 1999. Coseismic slip resolution along a plate boundary

megathrust: The Nankai Trough, southwest Japan. Journal of Geophysical

Research: Solid Earth 104, 1111-1129.

Sakai, A., Kanmera, K., 1981. Stratigraphy of the Shimanto terrane and the tectono-

stratigraphic setting of the greenstones of the northern part of Miyazaki

prefecture, Kyushu. Sci. Rep. Dep. Geol. Kyushu Univ. 14, 31–48.

Sakai, T., 1984. Microfossil stratigraphy of the Paleogene system in Kyushu Shimanto

    Belt [in Japanese with English abstract]. In: Biostratigraphy and International

    Correlation of the Paleogene System in Japan, 95–112.

Sakai, T., 1985. Geology of the Nichinan Group and the process of production of the

    outermargin olisthostrome belt of the Shimanto terrane [in Japanese with English

    abstract]. In: Mem. Symp. on Formation of Slump Facies and their Relationship

    to Tectonics, some Problems on the Deformation of Unconsolidated Sediments,

    95–116.

Scholz, C., Small, C., 1997. The effect of seamount subduction on seismic coupling.

    Geology 25, 487-490.

Scholz, C., 1998. Earthquakes and friction laws. Nature 391, 37-42.

Seno, T., Stein, S., Gripp, A.E., 1993. A model for the motion of the Philippine Sea plate

    consistent with NUVEL-1 and geological data. Journal of Geophysical Research

    98, 941–948.

Smith, T.M., Sayers, C.M., Sondergeld, C.H., 2009. Rock properties in low-porosity/low-

    permeability sandstones. The Leading Edge 28, 48-59.

Strasser, M., Dugan, B., Kanagawa, K., Moore, G.F., Toczko, S., Maeda, L., Kido, Y.,

    Moe, K.T., Sanada, Y., Esteban, L., Fabbri, O., Geersen, J., Hammerschmidt, S.,

    Hayashi, H., Heirman, K., Hüpers, A., Jurado Rodriguez, M.J., Kameo, K.,

    Kanamatsu, T., Kitajima, H., Masuda, H., Milliken, K., Mishra, R., Motoyama, I.,

    Olcott, K., Oohashi, K., Pickering, K.T., Ramirez, S.G., Rashid, H., Sawyer, D.,

    Schleicher, A., Shan, Y., Sharbek, R., Song, I., Takeshita, T., Toki, T., Tudge, J.,

Webb, S., Wilson, D.J., Wu, H.-Y., Yamaguchi, A., 2014. Site C0012. Proc.
IODP 338, 1-26.

Taira, A., Okada, H., Whitaker, J.H., & Smith, A.J., 1982. The Shimanto Belt of Japan:
cretaceous-lower Miocene active-margin sedimentation. Geological Society,
London, Special Publications 10, 5-26.

Teraoka, Y., Okumura, K., 1992. Tectonic division and Cretaceous sandstone
compositions of the Northern Belt of the Shimanto Terrane, southwest Japan.
Mem. Geol. Soc. Jpn. 38, 261–270.

Tobin, H.J., Kinoshita, M., 2006. NanTroSEIZE: the IODP Nankai Trough seismogenic
zone experiment. Scientific Drilling, 2, 23-27.

Tsuji, T., Kimura, G., Okamoto, S., Kono, F., Mochinaga, H., Saeki, T., Tokuyama, H.,
2006. Modern and ancient seismogenic out-of-sequence thrusts in the Nankai
accretionary prism: Comparison of laboratory-derived physical properties and
seismic reflection data. Geophysical Research Letters 33, L18309.

Ueda, Y., 2005. Bouguer gravity anomalies (ver. 2004) of Japanese Island arcs and its
adjacent seas. Rep. Hydrogr. Oceanogr. Res 41, 1-26.

Wang, K., Bilek, S., 2011. Do subducting seamounts generate or stop large earthquakes?,
Geology 39, 819-822.

Yamazaki, T., Okamura, Y., 1989. Subducting seamounts and deformation of overriding
forearc wedges around Japan. Tectonophysics 160, 207-229.